This is to certify that the

dissertation entitled

The Disappearance of Fusion-fission and the Onset of Multifragmentation

presented by

Eugene Edward Gualtieri

has been accepted towards fulfillment of the requirements for

Ph.D. degree in Physics

Gary D. Westfall
Major professor

Date July 21, 1995

THE DISAPPEARANCE OF FUSION-FISSION AND THE ONSET OF MULTIFRAGMENTATION

by

EUGENE EDWARD GUALTIERI

A DISSERTATION

Submitted to
Michigan State University
in partial fulfillment of the requirements
for the Degree of

DOCTOR OF PHILOSOPHY

Department of Physics and Astronomy

1995

ABSTRACT

THE DISAPPEARANCE OF FUSION-FISSION AND THE ONSET OF MULTIFRAGMENTATION

By

Eugene Edward Gualtieri

Information about the evolution of momentum transfer and excitation energy in intermediate energy heavy ion collisions of a fissile target was extracted through an analysis of fission fragment folding angles and charged particle production as beam energy is increased. An exclusive measurement of central events is performed using the MSU 4π Array as an impact parameter filter. For central collisions, a saturation is found in linear momentum transfer but evidence is presented that excitation energy increases steadily with beam energy. The implications of these measurements are discussed.

The space time aspects of the collisions are probed using an analysis which is sensitive to the shape of the ellipsoidal flow envelope of the reaction products in momentum space. This event shape analysis is used to determine whether the dominant reaction mechanism is of a sequential-binary or simultaneous nature and was performed in order to determine at what energy the multifragmentation channel becomes the dominant mode of decay. Such a transition is expected to occur when the excitation energy of the system approaches that of the total binding energy of the system. We deduce that 55 AMeV is the lower limit of the bombarding energy at which multifragmentation becomes dominant in this system.

For Mary

ACKNOWLEDGEMENTS

Here I sit, actually writing the acknowledgements page of my dissertation. I have been dreaming about this for five years. Of course, in order to actually reach this point, I needed the help of several people and I would like to thank them here.

First I must thank my parents, Edward and Lola Gualtieri, who taught me the basic values that helped me to persevere and finish this program. They experienced the ups and downs of a graduate student's life right along with me.

My deepest thanks go to my advisor, Gary Westfall. How he put up with such a paranoid graduate student I will never know. His confidence in me filled in when my own self-confidence waned, and kept me on track toward my degree. Gary's enthusiasm for his work and for the accomplishments of his colleagues is a great source of inspiration and something I admire greatly. I will consider myself a success if I can give to just one person what Gary has given me.

Working with Skip Vander Molen has been both a pleasure and a privilege. He is incredibly dedicated to his work, and more than willing to go above and beyond the call of duty in order to ensure the success of an experiment. I owe a great deal of what I know about nuclear electronics to time spent in the vault with Skip and an oscilloscope.

The post-docs that have come and gone during my time with the 4π group – Roy Lacey, Sherry Yennello, and Bill Llope – have all provided invaluable guidance and advice. Though their styles and personalities differed, they all shared a real devotion to their work and were all willing to take the time to help me and other graduate students. From their examples, I learned what qualities are necessary in order to succeed.

A huge "thank you" goes to my fellow graduate students in the 4π group: Stefan Hannuschke, Robert Pak, Nathan Stone, and Jaeyong Yee. One of the greatest joys in my graduate career has been working in collaboration with them on physics experiments. When it came time to run my thesis experiment it was reassuring to know that they were there to back me up at 3:00 in the morning.

Special thanks go to Salvatore Fahey, my friend and partner during the first two years of classes and the candidacy exam. The memory of the expression on Sal's face as we opened the results of that exam is indelibly etched in my mind, and kept me going whenever I was frustrated or depressed.

Finally, I must thank my wife, Mary McManus. I could not have made it through this program without her unconditional support and tireless faith in me. Although she was struggling along the same path as me, in pursuit of her own degree, she was absolutely selfless in her support of me, and was always there whenever I needed her to listen.

C

LIS

LIS

Contents

5

A

LI

List of Tables

L

List of Figures

Chapter 1

Introduction

The study of nuclear fission as a means to probe the nature of nuclear reactions began in the 1950s. The determination of the linear momentum transfer in nuclear collisions from the angular correlation between fission fragments was used as a tool to study the mechanisms governing the reactions between two nuclei [Nich 59, Sikk 62]. Bombarding energies available at this time were very close to the Coulomb barrier for systems of light projectiles ($A \leq 20$) and heavy targets ($A \geq 100$), and much work was done studying collisions of this type.

Heavy ion reactions at the Coulomb barrier can be categorized into two groups based on impact parameter. Very peripheral collisions result in direct reactions involving the transfer of a few nucleons and very little linear momentum. In central collisions, complete fusion of the target and projectile occurs, and a compound nucleus is formed which then either decays by fission or evaporation, depending on the system mass. At bombarding energies 1-4 MeV above the Coulomb barrier, a third type of reaction mechanism, "deep-inelastic processes", develops at intermediate impact parameters. This process involves a large amount of mass and energy transfer between the projectile and target, but because of high angular momentum barriers does not result in the formation of a true compound system. Rather, the dinuclear character remains while many of the degrees of freedom are relaxed [Plas 78, Zoln 78, Ngo 86, Viol 89].

As beam energies are increased to ~10 - 15 AMeV, the probability for complete fusion to occur begins to decrease dramatically. In its place occurs an incomplete fusion, or "massive transfer" process, in which some portion of the projectile mass fuses with the target, and the remaining mass is lost in a forward-peaked spray of particles which is emitted before equilibration can occur. Momentum transferred to the fused system is less than in the case of complete fusion, and this is apparent in the angular correlations of the fission fragments [Zoln 78, Back 80, Viol 82, Sain 84, Lera 84]. For highly fissile targets, very peripheral collisions in this beam energy range can also lead to fission, but the reaction dynamics in this case are very different. Since there is little linear momentum transferred to the fissioning system, the correlation angle, or folding angle, between the fission fragments is much closer to 180^{o} in the lab frame.

Figure 1.1 shows a typical fission fragment folding angle distribution with contributions from complete fusion, incomplete fusion, and target fission. The complete fusion component (σ_{CF}) is peaked at an angle corresponding to complete momentum transfer, whereas the inclusive component for central collisions (σ_F), containing incomplete and complete fusion, peaks at a slightly larger angle corresponding to incomplete momentum transfer ($p_{||}^{mp}$). The low momentum transfer component is also visible near 180^{o} .

As beam energy is further increased from 10 AMeV up to ~ 50 AMeV, complete fusion continues to become less probable, and more of the fusion-like cross section is dominated by massive transfer processes. In the $^{14}N + ^{238}U$ system, for example, the maximum estimated cross section for complete fusion has been measured to decrease from 56% to 21% of the total fission cross section as beam energy increases from 15 to 30 AMeV [Tsan 84]. Correspondingly, the most probable momentum transfer, *as a fraction of beam momentum* for fusion-like events decreases, indicating that preequi-

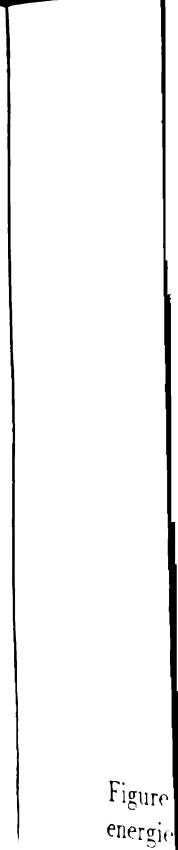

Figure
energie
comple
momen

librium

[Back s

shown t

indicati

their st

Figure

As b

for heav

This is

ing angl

[Conj &

shown i

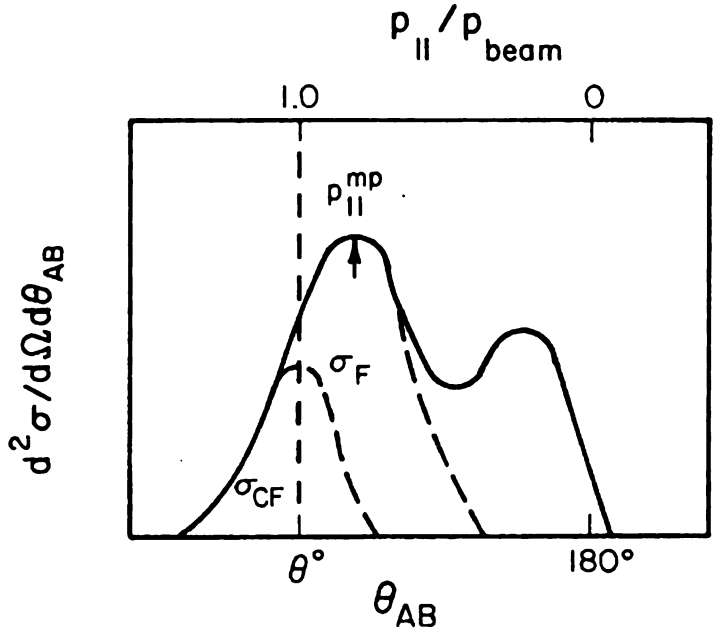

Figure 1.1: Representative distribution of the fission fragment folding angle θ_{AB} at energies well above the Coulomb barrier. Angle θ° represents the expected angle for complete fusion followed by symmetric fission. θ_{AB} is translated into longitudinal momentum transfer, $p_{||}/p_{beam}$, on the above scale. [Viol 89]

librium emission of particles becomes more important as bombarding energy increases [Back 80, Awes 81, Tsan 84]. This decrease in fractional momentum transfer has been shown to follow the same systematic function of beam velocity for a variety of systems, indicating that it is primarily the relative velocity of the colliding nuclei, rather than their structure, that determines the momentum transfer [Viol 82, Tsan 84, Nife 85]. Figure 1.2 illustrates this linear decrease.

As beam momentum increases far beyond the Fermi momentum (~250 AMeV/c for heavy nuclei), the cross section for incomplete fusion has been reported to decline. This is most dramatically displayed by the disappearance of the peak in the folding angle distributions corresponding to these high linear momentum transfer events [Conj 85, Faty 85, Jacq 85, Bege 92, Schw 94]. An example of this phenomenon is shown in Figure 1.3.

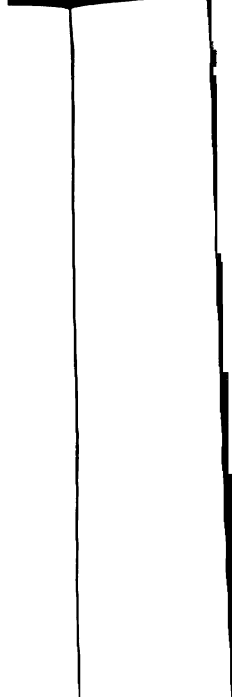

Figure
mentu
target
ordina

Th

nant re

AMeV

stated

fect of

of eacl

collisic

to the

is show

plotted

fer per

shown.

Nat

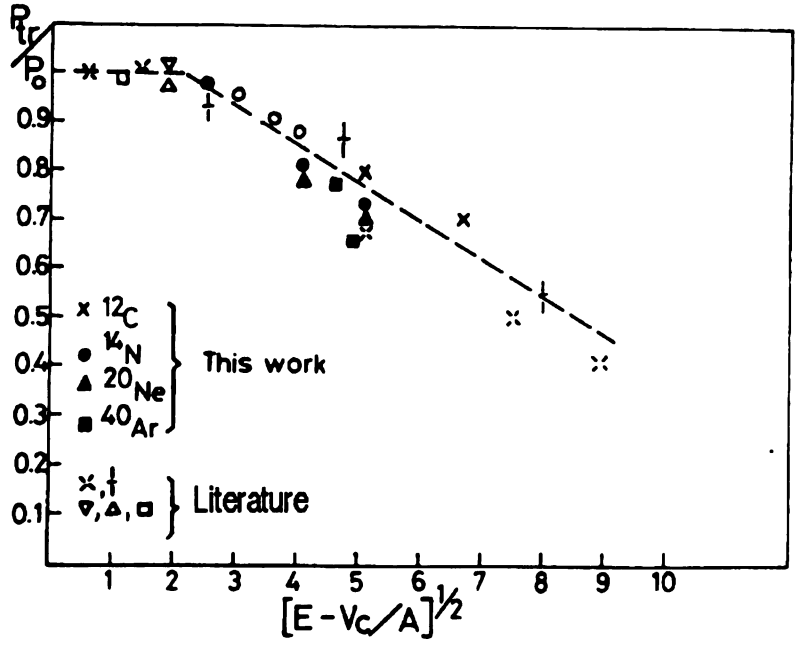

Figure 1.2: Systematics of the energy dependence of the most probable linear momentum transfer in measured in central collisions of various projectiles on actinide target nuclei [Nife 85]. The abscissa is proportional to the beam velocity, and the ordinate is the momentum transfer as a fraction of the beam momentum.

The disappearance of this peak has led to much speculation regarding the dominant reaction mechanism in systems such as $^{40}Ar + ^{232}Th$ at beam energies above ~40 AMeV, and was one of the prime motivations for the present study. It is generally stated that, at these energies, nucleon-nucleon interactions begin to dominate the effect of the mean field [Viol 82, Woo 83, Sain 84, Conj 85]. That is, as the momentum of each nucleon in the projectile begins to approach the Fermi momentum, individual collisions between projectile nucleons and target nucleons impart enough momentum to the latter to allow them to escape the mean field of the nucleus. Evidence of this is shown in Figure 1.4 where the mean momentum transfer *per projectile nucleon* is plotted versus beam energy for a variety of systems. The maximum momentum transfer per nucleon saturates at or below the Fermi momentum for all of the projectiles shown.

Naturally intertwined with the discussion of linear momentum transfer is the topic

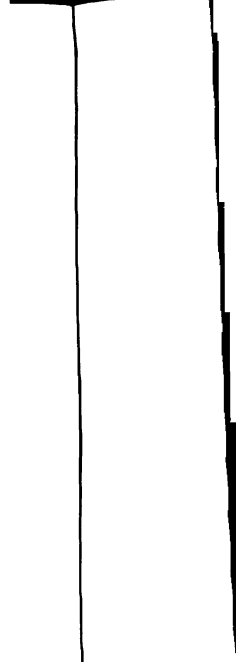

Figure
and 4
θ_{ff} =
locati

of ene
kineti
citatio
requir
ing th
to est
well a
disagr
systen
Poll 9
to the
increa
no lon
one ex

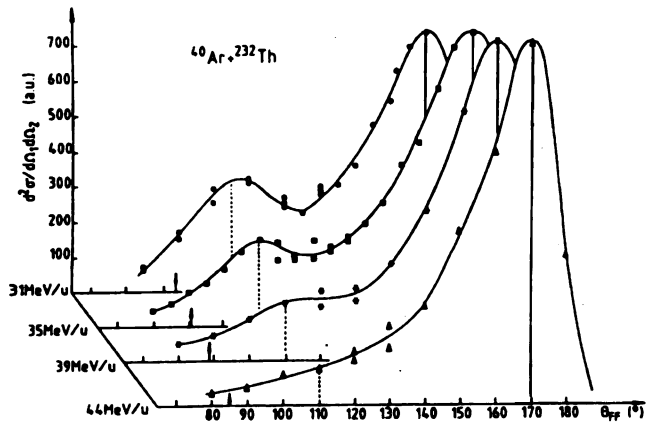

Figure 1.3: Fission fragment folding angles for the system ^{40}Ar + ^{232}Th at 31, 35, 39, and 44 AMeV. Curves are drawn to guide the eye. The vertical lines correspond to $\theta_{ff} = 170^{\circ}$ and 110° (about 0.8 and 7 GeV/c respectively); the arrows indicate the locations of the folding angles corresponding to full momentum transfer. [Conj 85]

of energy deposition. In the massive transfer picture, it is assumed that all of the kinetic energy of the captured mass is converted into thermal excitation energy. Excitation energy is often calculated by assuming that a given amount of energy is required on the average to evaporate a nucleon (~15 MeV), and then either measuring the mass of the evaporation residue or the total number of evaporated particles to estimate the excitation energy. Measurements using this and other methods, as well as microscopic calculations of intranuclear particle-particle collisions have led to disagreement over the existence of a saturation in the deposited energy in asymmetric systems such as ^{40}Ar + ^{232}Th [Jacq 84, Jacq 85, Conj 85, Bhat 89, Jian 89, Troc 89, Poll 93, Schw 94, Utle 94]. Also unclear, is whether the demise of fusion-fission is due to the onset of a new exit channel, such as simultaneous multifragmentation, or if the increase in preequilibrium and statistical emission simply leaves a residue which is no longer highly fissile [Gros 86, Schw 94, Poll 93, Jacq 85, Conj 85]. An example of one experimental result which measured a saturation in energy deposition is shown

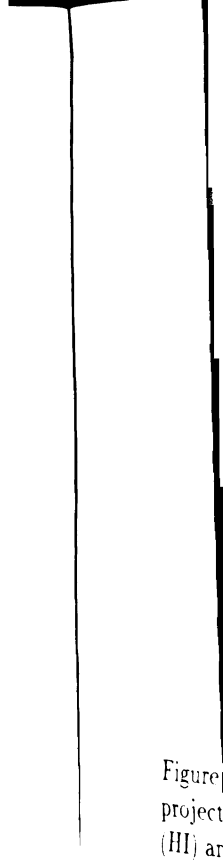

Figure
project
(HI) ar
(circle
Upper
maxim
of proj
respect
the lar

in Figu

Att

as fusic

tal obs

emissio

elongat

sequent

thus, th

betwee

space, v

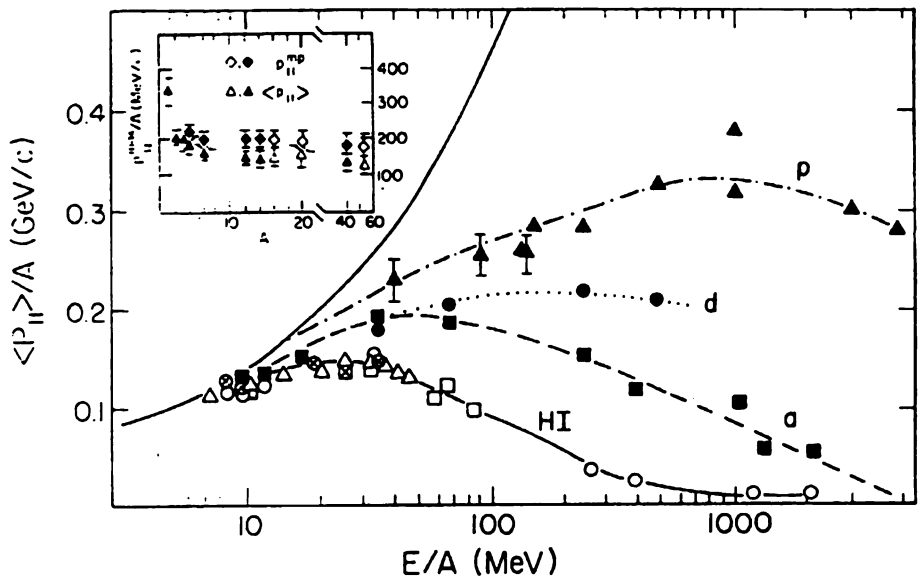

Figure 1.4: Average linear momentum transfer per nucleon, $\langle p_{||} \rangle / A$, as a function of projectile E/A from reactions with Th and U targets. Symbols from the heavy ions (HI) are as follows: ^{6}Li–(solid square), ^{12}C–(open square), ^{14}N–(open triangle), ^{16}O–(circle w/ X), ^{20}Ne–(open circle). Lines drawn through points are to guide the eye. Upper solid line indicates the beam momentum per projectile nucleon. Insert gives maximum value of the linear momentum transfer per projectile nucleon as a function of projectile mass; diamonds and triangles represent most probable and average value, respectively. Solid points indicate established upper bounds; open points represent the largest values observed over a more restricted range of energies. [Viol 89]

in Figure 1.5.

Attempts have been made to differentiate between sequential binary decays, such as fusion-fission, and simultaneous multifragmentation through the use of experimental observables which are sensitive to the timescale of the reaction mechanism or the emission pattern of the particles. Sequential binary decays are expected to be more elongated in momentum space than simultaneous processes [Cebr 90, Lope 89]. In a sequential breakup, the earliest decays occur when the system is maximally heated; thus, these decays carry off the most energy and there is a large relative momentum between the two daughters. This initial decay defines a primary axis in momentum space, whereas later decays occur after the system has cooled and are less likely to

Figure
cles) a
scale)
excita

define

is the

sociat

Use o

multa

Cebr

It

sions

of the

differe

evapor

of ^{40}A

well in

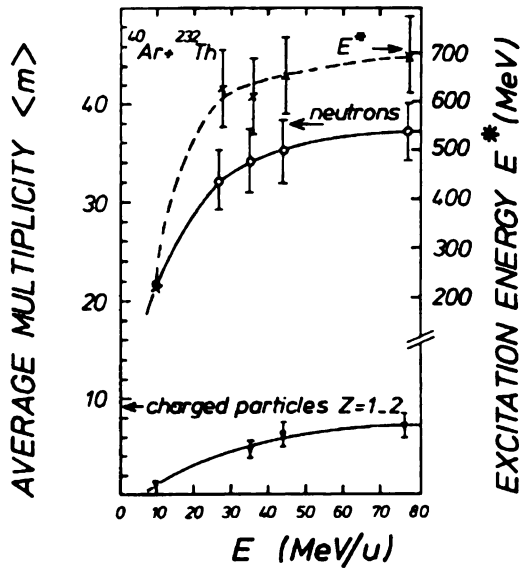

Figure 1.5: Evolution with bombarding energy of the total number of neutrons (circles) and evaporated charged particles (triangles) summed over Z=1,2 (left-hand scale) released from the most dissipative collisions. From these multiplicities the excitation energies (crosses) have been estimated (right-hand scale). [Jian 89]

define the event shape [Cebr 90]. One technique that gives access to the event shape is the kinetic flow tensor [Cugn 82, Gyul 82, Cugn 83, Gust 84, Lope 89], and the associated variables, sphericity and coplanarity [Gyul 82, Lope 89, Cebr 90, Cebr 90a]. Use of this technique has provided evidence of a transition from sequential to simultaneous mechanisms in systems such as ^{40}Ar + ^{51}V (See Figure 1.6.) [Cebr 90, Cebr 90a, Barz 91].

It was our intent to determine the dominant reaction mechanism in central collisions of ^{40}Ar + ^{232}Th at beam energies above $\sim$ 40 AMeV. Does the disappearance of the high-momentum-transfer peak in Figure 1.3 signify the onset of a radically different reaction mechanism, or simply the disappearance of fission in favor of an evaporative process? In a effort to shed light on this topic, we studied collisions of ^{40}Ar + ^{232}Th from the beam energy range where incomplete fusion is important well into the range where nucleon-nucleon effects are expected to dominate the mean

Figure
beam e
represe
The un

field.

mentur

observa

The

in this

technic

subeler

are inc

Cha

tion en

of light

Cha

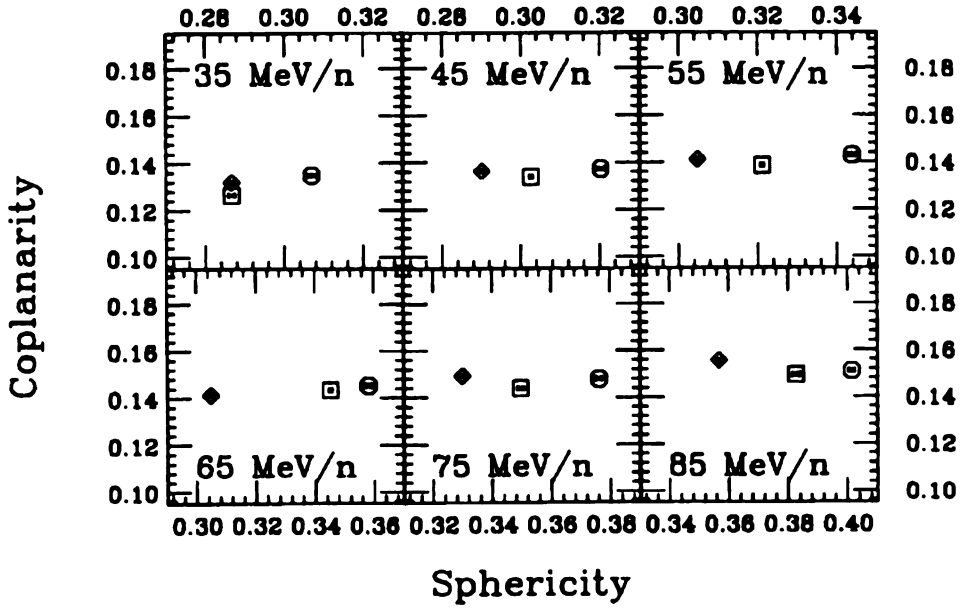

Figure 1.6: A study of the average sphericity and coplanarity values as a function of beam energy for the system ^{40}Ar + ^{51}V. The centroids of a sequential simulation are represented by diamonds, those of the experimental data are represented by circles. The uncertainties displayed are statistical errors of the mean.

field. We have made use of both the conventional observables used to study momentum transfer, such as fission fragment folding angles, as well as newer "global observables", such as sphericity, to determine the event shape.

The results of the study of the ^{40}Ar + ^{232}Th from 15 - 115 AMeV are presented in this work which is organized as follows. Chapter 2 contains a description of the technical details of the experiment, including a description of the 4π Array and its subelements, and the electronics used. Details of the data reduction and calibration are included also.

Chapter 3 discusses experimental results regarding momentum transfer and excitation energy as determined through fission fragment folding angles and the production of light charged particles and intermediate mass fragments.

Chapter 4 concerns results of the event shape analysis. A description of the

method for determining the event shape is presented, along with details regarding various effects which must be considered in the analysis.

Chapter 5 contains a summary and brief conclusions. Appendix A discusses the experimental determination of the centrality of an event, and the technique of impact parameter selection based on global observables is explained. Also discussed are the concept of autocorrelations and the reasoning behind the choices of the global observables used.

Chapter 2

Experimental Details

2.1 Introduction

The experiment was performed at the National Superconducting Cyclotron Laboratory (NSCL) at Michigan State University (MSU) where ^{40}Ar beams of E = 15 to 115 AMeV accelerated by the K1200 cyclotron bombarded a 1 mg/cm^2 ^{232}Th target. Reaction products of nuclear collisions were detected with the MSU 4π Array [West 85]. Event information from each collision was digitized on an event-by-event basis, written to magnetic tape, and analyzed off-line.

The 4π Array, as outfitted for this experiment, provided nearly 4π detection of light charged particles, intermediate mass fragments, and fission fragments. Most previous experiments studying this system did not have coverage as comprehensive as that provided by the Array, either in geometric acceptance or range of particle types identified. It was our hope that with the extensive coverage of this system over such a wide range of beam energies we could determine the evolution of the reaction mechanism in central collisions. The following sections in this chapter describe in detail the 4π Array, its various components and their acceptance, and the methods used to calibrate them.

2.2

Figu
consi
icosa
12 pe
as ba
faces

Fi
onal(p
Moun
detect
standa
are sul
multi-w
In total
tors. 55
162° .
forward
cover ap
array is

2.2.1

The 170
fast plas
Bicron B

2.2 Michigan State University 4π Array

Figure 2.1 depicts the underlying geometry of the MSU 4π Array. The 4π Array consists of 30 separate sub-modules enclosed within a 32-faced, aluminum, truncated icosahedron. Externally, it resembles a soccer ball, having 20 hexagonal faces, and 12 pentagonal ones. All of the hexagonal faces, and 10 of the pentagonal ones serve as backplates upon which the 30 modules are mounted. The remaining pentagonal faces serve as an entrance and exit for the incident beam.

Figure 2.2 shows a diagram of a hexagonal module of the 4π Array. Each hexagonal(pentagonal) module consists of 6(5) close packed plastic phoswich detectors. Mounted in front of each phoswich is a gas chamber which can be used as a ΔE detector for particles stopping in the thin layer of the phoswich detector, and as a standalone Bragg Curve counter (BCC). The BCCs in the 5 most forward modules are subdivided into 6 separate detectors. In front of each BCC is a low pressure multi-wire proportional counter (MWPC) for the detection of slow, heavy fragments. In total, these sub-modules making up the main ball consist of 170 phoswich detectors, 55 BCCs, and 30 MWPCs, and cover lab polar angles from approximately 18° to 162° . In addition to the detectors in the main ball, the 4π Array also contains a forward array consisting of 45 plastic phoswiches. These are not close packed, and cover approximately 54% of the solid angle from 7° to 18° . The layout of the forward array is shown in Figure 2.3.

2.2.1 Plastic Phoswich Counters

The 170 ball plastic phoswiches are composed of 3 mm thick sheet of Bicron BC-412 fast plastic scintillator (ΔE component) optically coupled to 25 cm thick block of Bicron BC-444 slow plastic scintillator (E component). The terms "fast" and "slow"

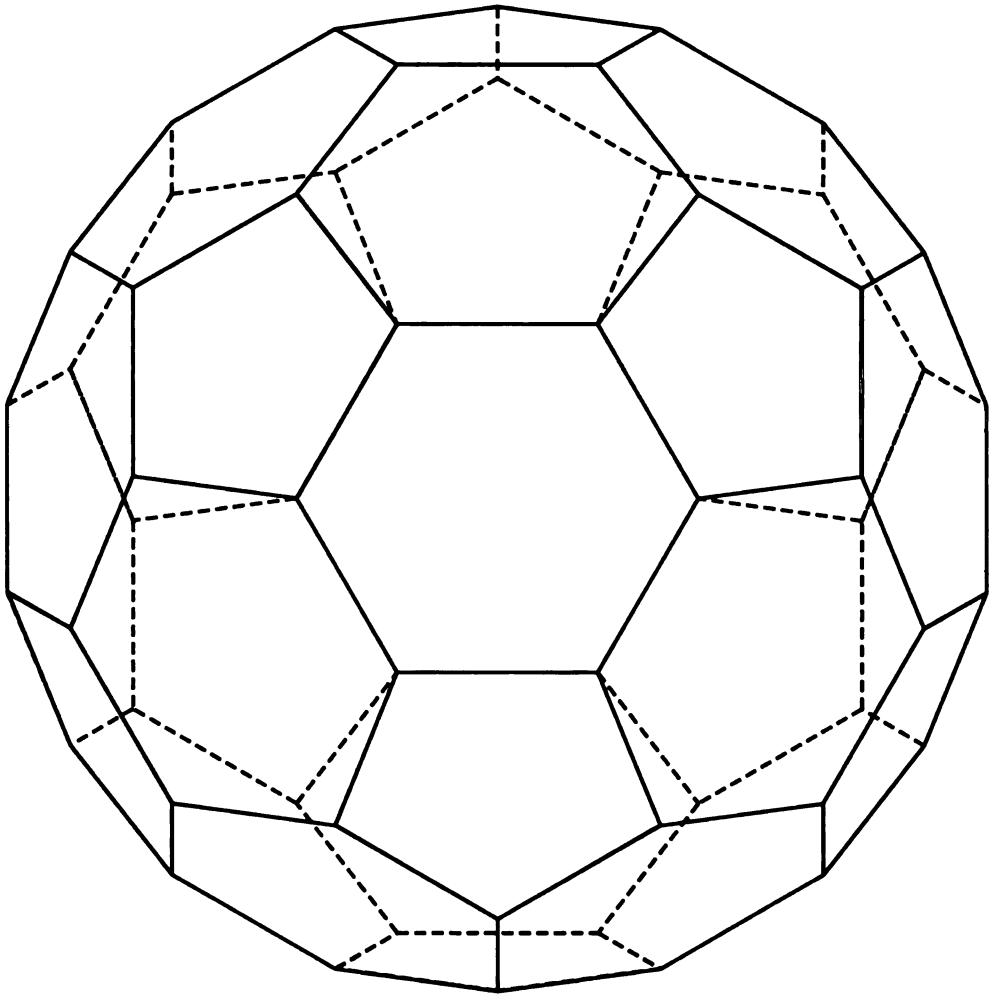

Figure 2.1: Schematic diagram showing the underlying geometry of the 4π Array.

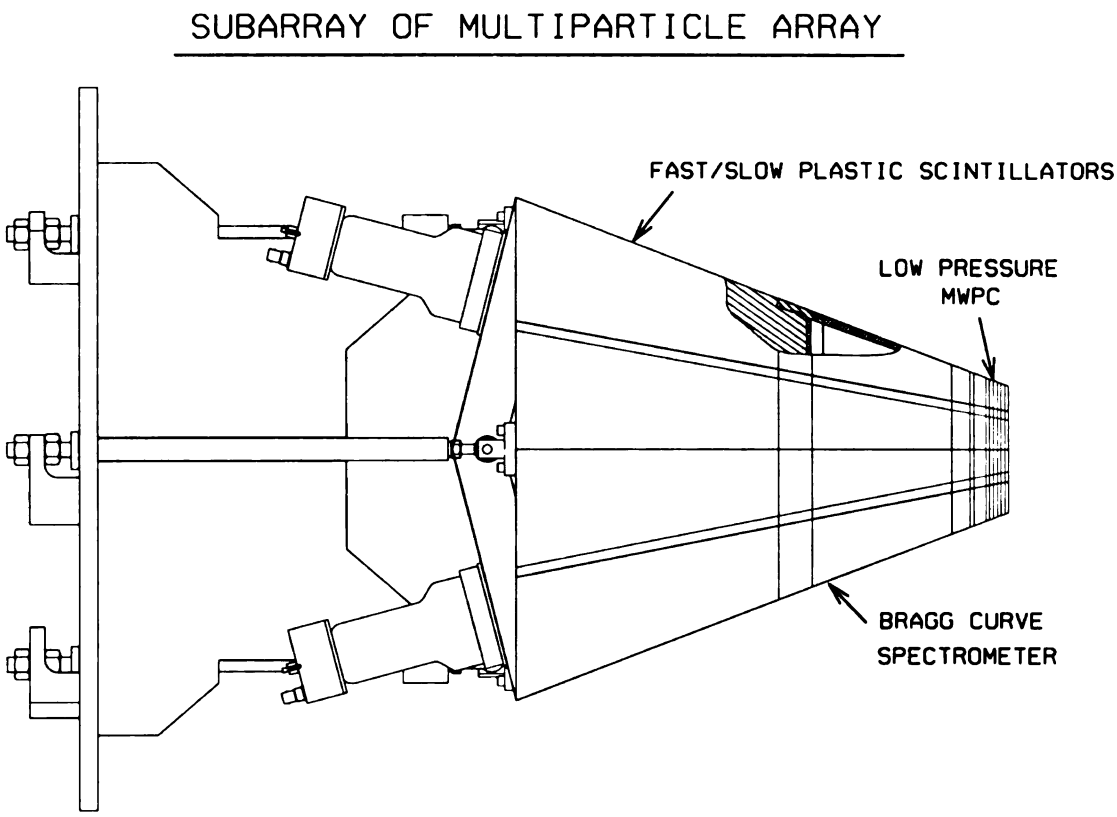

Figure 2.2: Schematic diagram showing the components of a 4π module.

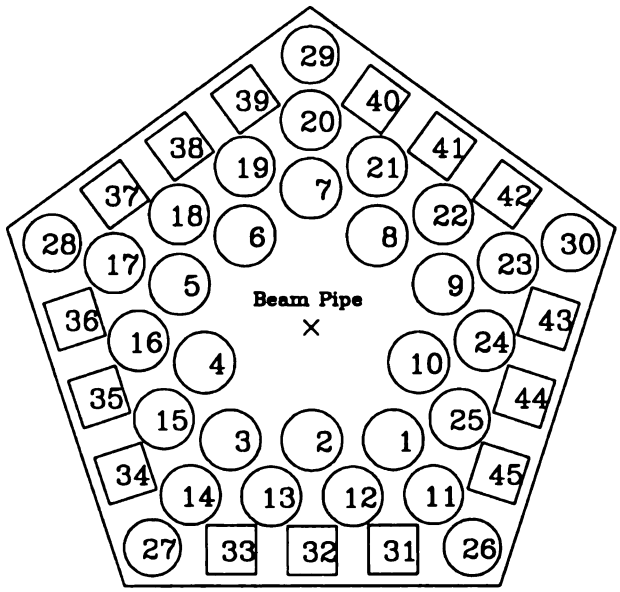

Figure 2.3: The layout of the 45 forward array detectors.

refer

parti

scinti

fast p

thresh

Th

pentag

differen

msr. an

olds. an

summa

A p

produc

through

medium

and is

This is

is ampl

tube. T

two diff

This pr

A ty

shown i

Figure 2

which st

on the y

refer to the response time of the plastic when penetrated by an energetic charged particle. The characteristics of the scintillators are summarized in Table 2.1. The scintillator in the forward array telescopes is identical to that of the ball, however the fast plastic layer in the forward array is only 1.6 mm thick. This lowers the energy threshold of the telescopes, and allows for better detection of heavy particles.

The ball hexagonal modules each cover a solid angle of 6 $\times$ 66 msr, and the pentagonal modules cover 5 $\times$ 50 msr. The forward array telescopes also have two different geometries. There are 30 cylindrically shaped detectors each covering 3.02 msr, and 15 with a truncated pyramidal shape covering 2.75 msr. The energy thresholds, angular coverage, and Z identification capabilities of the phoswich detectors are summarized in Table 2.2.

A particle impinging on a phoswich detector, and stopping in the second layer, produces two flashes of light. The first is a fast signal produced as the particle passes through the fast plastic, and is proportional to the rate of energy loss (ΔE) in the medium. The second is a slow signal produced as the particle stops in the slow plastic, and is proportional to the total energy loss (E) of the particle in the slow plastic. This is very close to the total energy of the particle. The combined light produced is amplified and transformed to an electronic signal by an 8-stage photo-multiplier tube. This signal is approximately separated into its fast and slow components using two different gates which trigger charge to digital converters (Lecroy FERA 4301b). This process is illustrated graphically in Figure 2.4.

A typical example of a raw spectrum produced by a ball phoswich detector is shown in Figure 2.5. A similar spectrum is shown for a forward array phoswich in Figure 2.6. The strong band close to the y-axis in these spectra is caused by particles which stop in the ΔE layer and create no E signal. These points do not lie exactly on the y-axis because some of the fast signal leaks into the slow gate. This band is

Table 2.1: Characteristics of the two types of scintillator used in the phoswich detectors.

BICRON Plastic	Rise time (ns)	Fall time (ns)
BC-412 (fast)	1.0	3.3
BC-444 (slow)	19.5	179.7

Table 2.2: Specification of the ball and forward array phoswich detectors.

Characteristic	Ball Phoswich	FA Phoswich
Polar Angle region (^{o})	18 - 162	7 - 18
Solid Angle coverage (%)	84	54
Z identification	1 - 8	1-10
Energy Threshold (AMeV)		
Proton	12	7
Helium	17	12
Carbon	32	22

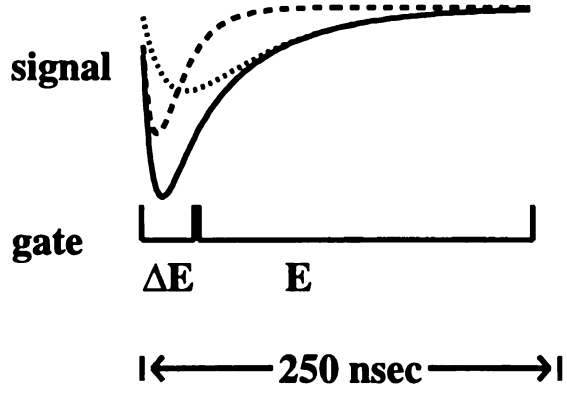

Figure 2.4: Diagram of the phoswich signal and gates.

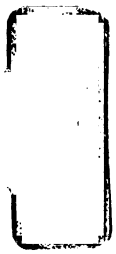

known as the punch-in line. Similarly, the band near the x-axis is caused by particles such as neutrons or gamma rays, which leave little or no signal in the ΔE layer but leave a large signal in the E layer. This band is called the neutral line. Both of these spectra are displayed in 512 channel resolution, but the data are recorded in 2048 channel resolution.

Phoswich Calibration

Because of the large number of detectors in the 4π Array, a system has been devised to minimize the amount of time required to calibrate each detector. This process involves creating a two-dimensional calibrated template to which all of the phoswich spectra are then matched. There are two components to this template: the gate lines and the response function.

The gate lines are created by drawing them directly onto a typical spectrum using a mouse driven graphics program. Before this is done, the spectrum is transformed such that the punch-in line and neutral line lie exactly on the x and y axes. This is done using the following transformations [Cebr 90]:

$$\begin{aligned} CH_f &= (\Delta E_{channel} - Y_0) - (E_{channel} - X_0)M_n \\ CH_s &= (E_{channel} - X_0) - (\Delta E_{channel} - Y_0)/M_p, \end{aligned} \tag{2.1}$$

where $\Delta E_{channel}$ and $E_{channel}$ are the fast and slow channel numbers recorded during the experiment, M_n and M_p are the slopes of the neutral and punch-in lines, and X_0 and Y_0 are the coordinates of the crossing point of the neutral and punch-in lines, representing the offset of the ADCs. The quantities CH_f and CH_s are the transformed channel numbers. The gatelines are used to produce a map file which converts the transformed channel numbers into the correct atomic number for each particle. As isotopic resolution is possible only for Z=1, all other elements are assigned a mass

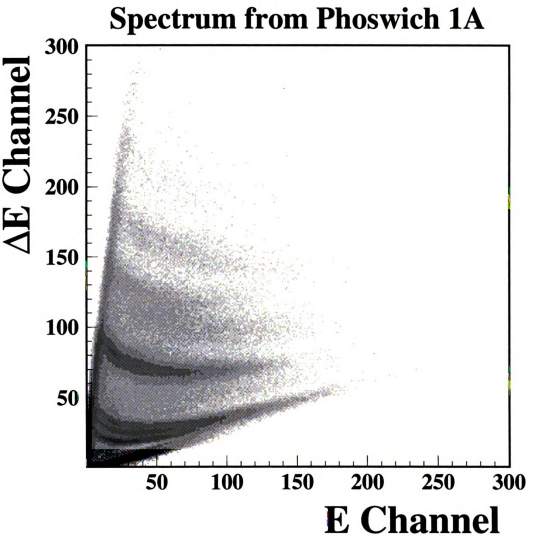

Figure 2.5: Typical raw spectrum from a ball phoswich for Ar + Th at 45 AMeV. Signals from particles with Z = 1 - 5 are visible with isotopic resolution for Z=1.

Figure 2.6
AMeV. Si
Z=1.

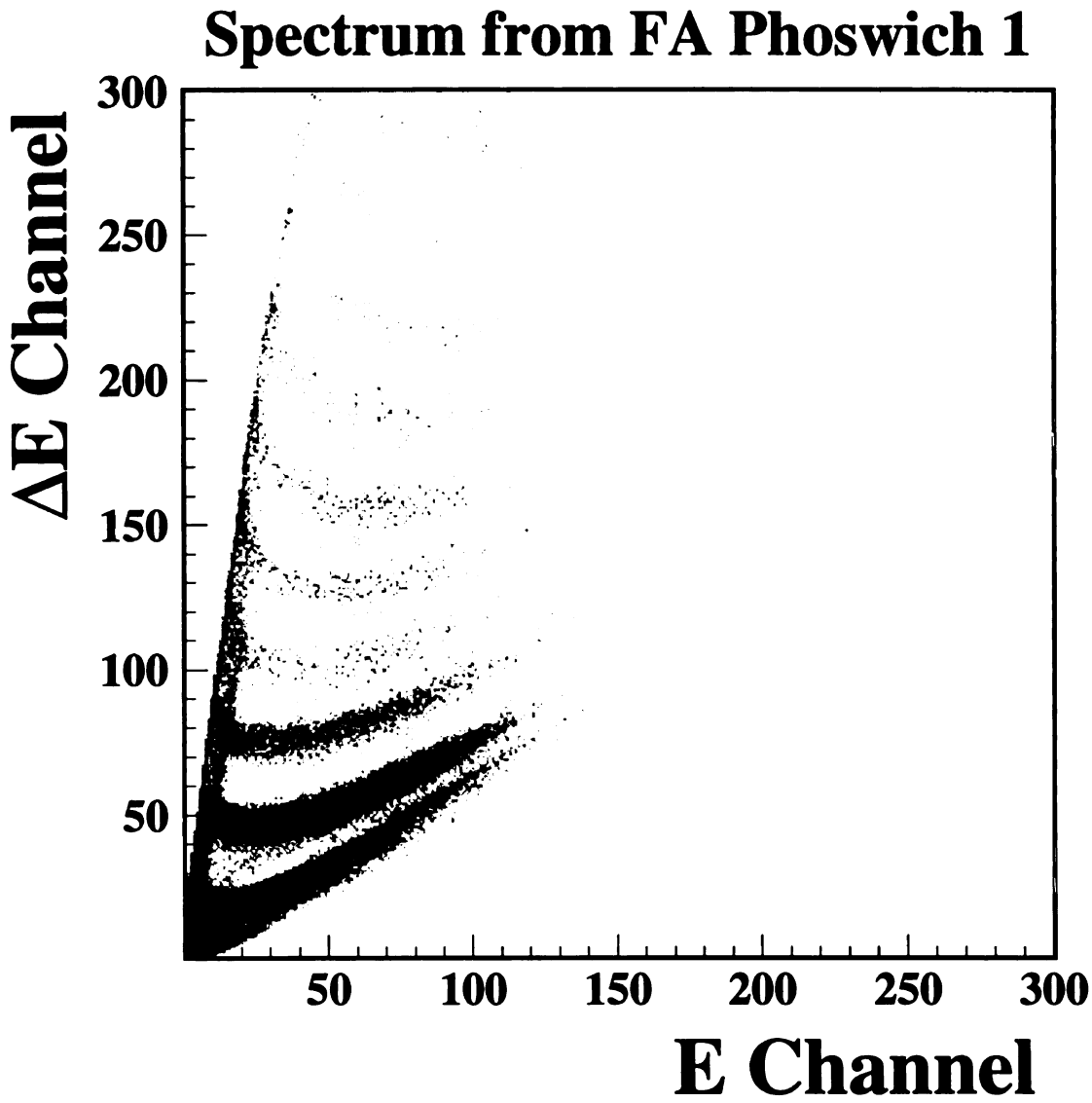

Figure 2.6: Typical raw spectrum from a forward array phoswich for Ar + Th at 45 AMeV. Signals from particles with Z = 1 - 9 are visible with isotopic resolution for Z=1.

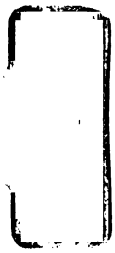

numb
detec
progr
a har
array
Th
ment

These
energy
termin
spectru
templa
number
used fo

Thu
ated wi
in the fa
particle
By provi
tained th
convert t

To su
phoswich

number corresponding to the most common isotope. Phoswich spectra from each detector are then transformed and gain matched to fit these gate lines using another program with a graphical interface, and the gain parameters are stored in a file on a hard disk. Figure 2.7 and Figure 2.8 show the gate lines for the ball and forward array phoswiches used for these data.

The response functions used are determined from a previous calibration experiment [Cebr 90], and have the form:

$$\begin{aligned} CH_s &= aE_s^{1.4}/A^{0.4}Z^{0.8} \\ CH_f &= bE_f^{0.5} - c. \end{aligned} \tag{2.2}$$

These equations convert the transformed fast and slow channel numbers into the energy lost in the corresponding plastic. The arbitrary constants a,b, and c are determined by fitting the lines following this functional form to the same representative spectrum used to create the gate lines. Thus, when the spectra are fit to the gate line template for particle identification, a map is also obtained between the raw channel number and the energy lost in the slow and fast plastic. The final response functions used for the ball are shown in Figure 2.9.

Thus far, we have described a process to convert the raw channel number associated with a detected particle into the correct atomic number and kinetic energy lost in the fast and slow plastic. The final step is to determine an incident energy for the particle based on its energy loss. This is done using the energy loss program DONNA. By providing DONNA with the densities and thickness of the detector media we obtained the final link which, in combination with the response functions, allowed us to convert the raw channel number directly into incident kinetic energy.

To summarize, a template is produced for the ball and forward array which all phoswich spectra are matched to. From this template look-up tables are made which

DE Channel //

5

40

30

200

100

0

0

Figure

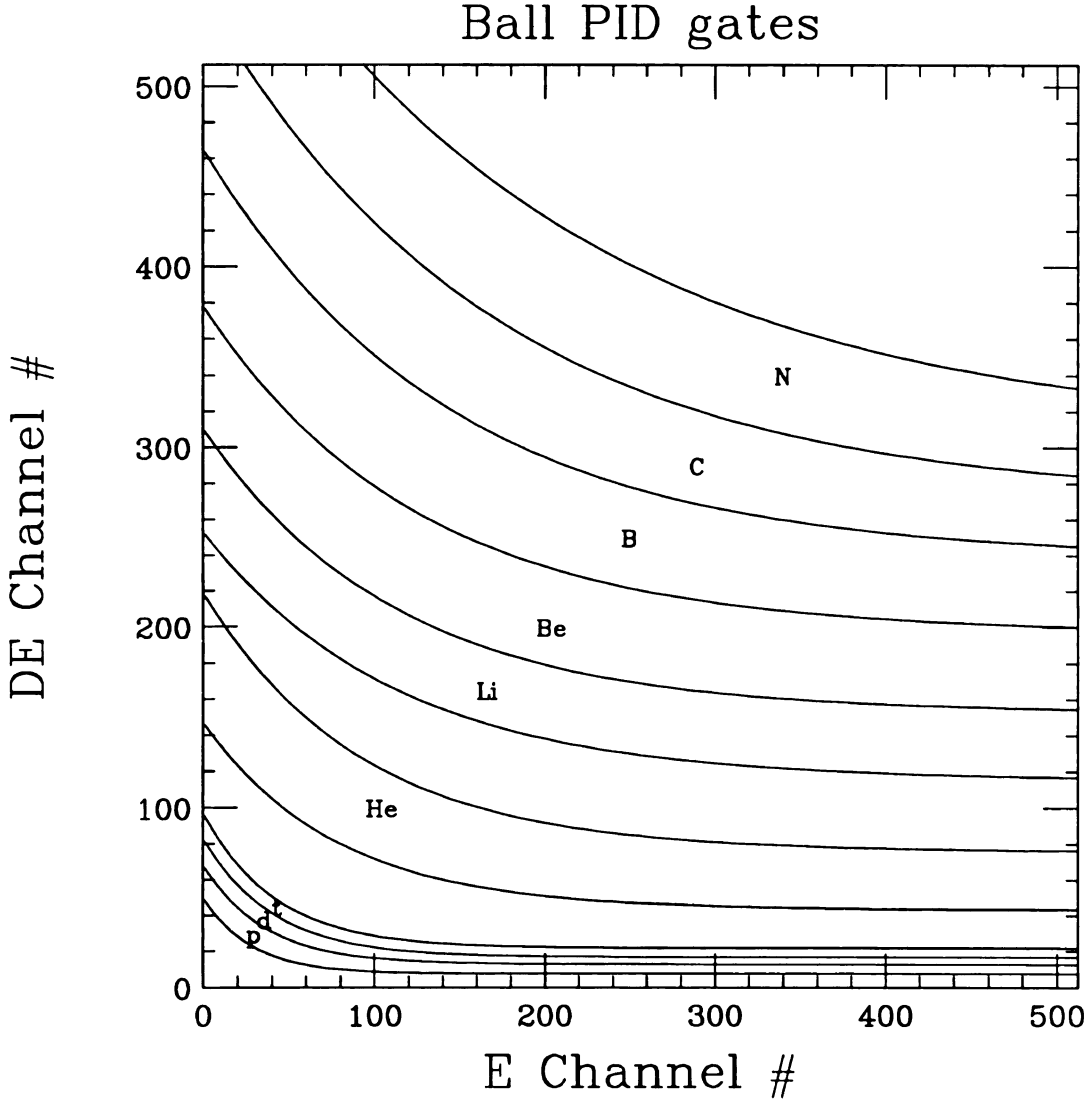

Figure 2.7: The particle gate lines for p,d,t and Z = 2 - 7 for a ball phoswich.

Figure
phoswi

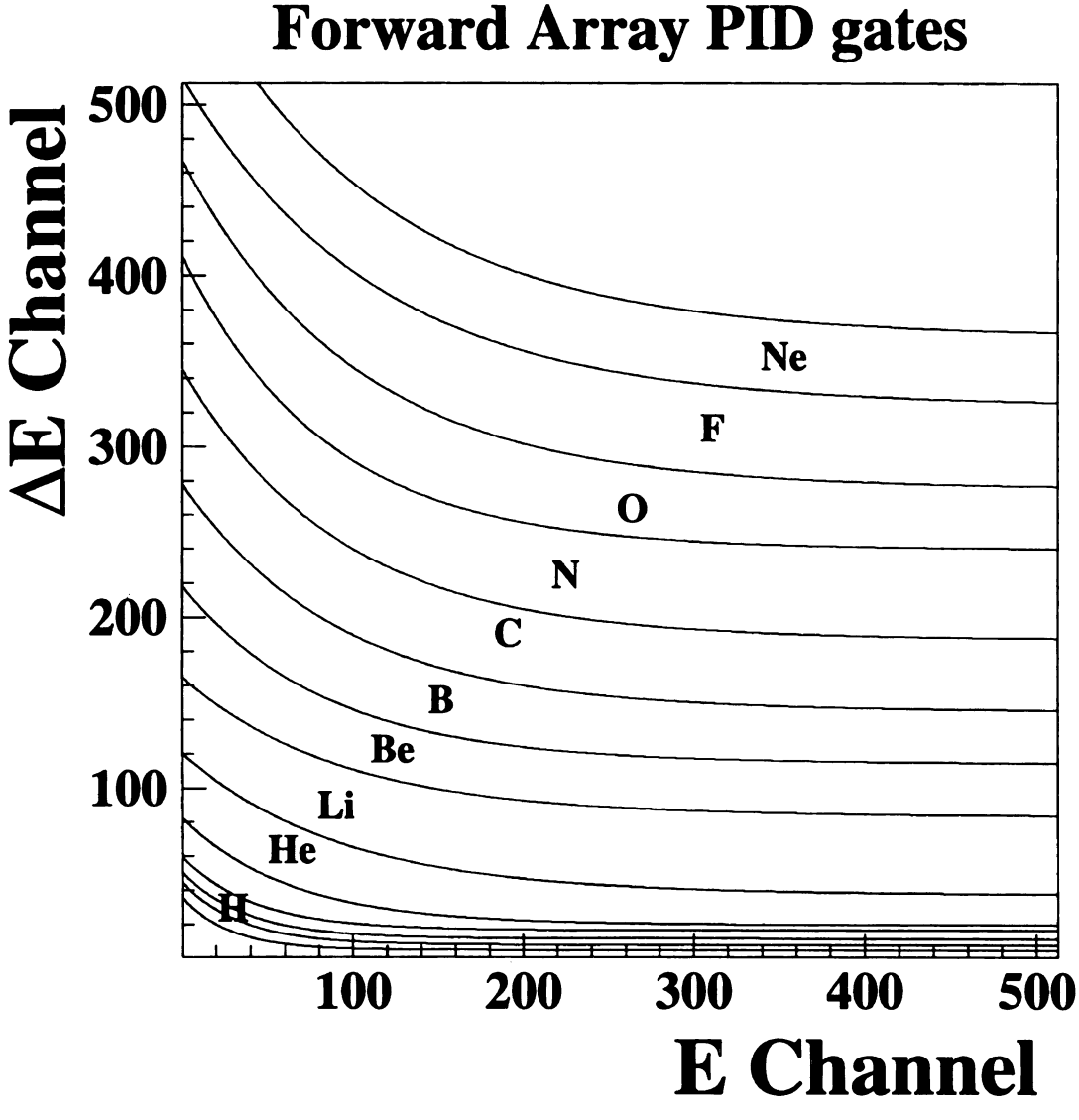

Figure 2.8: The particle gate lines for p,d,t and Z = 2 - 10 for a forward array phoswich.

DE channel #

Figure 2.

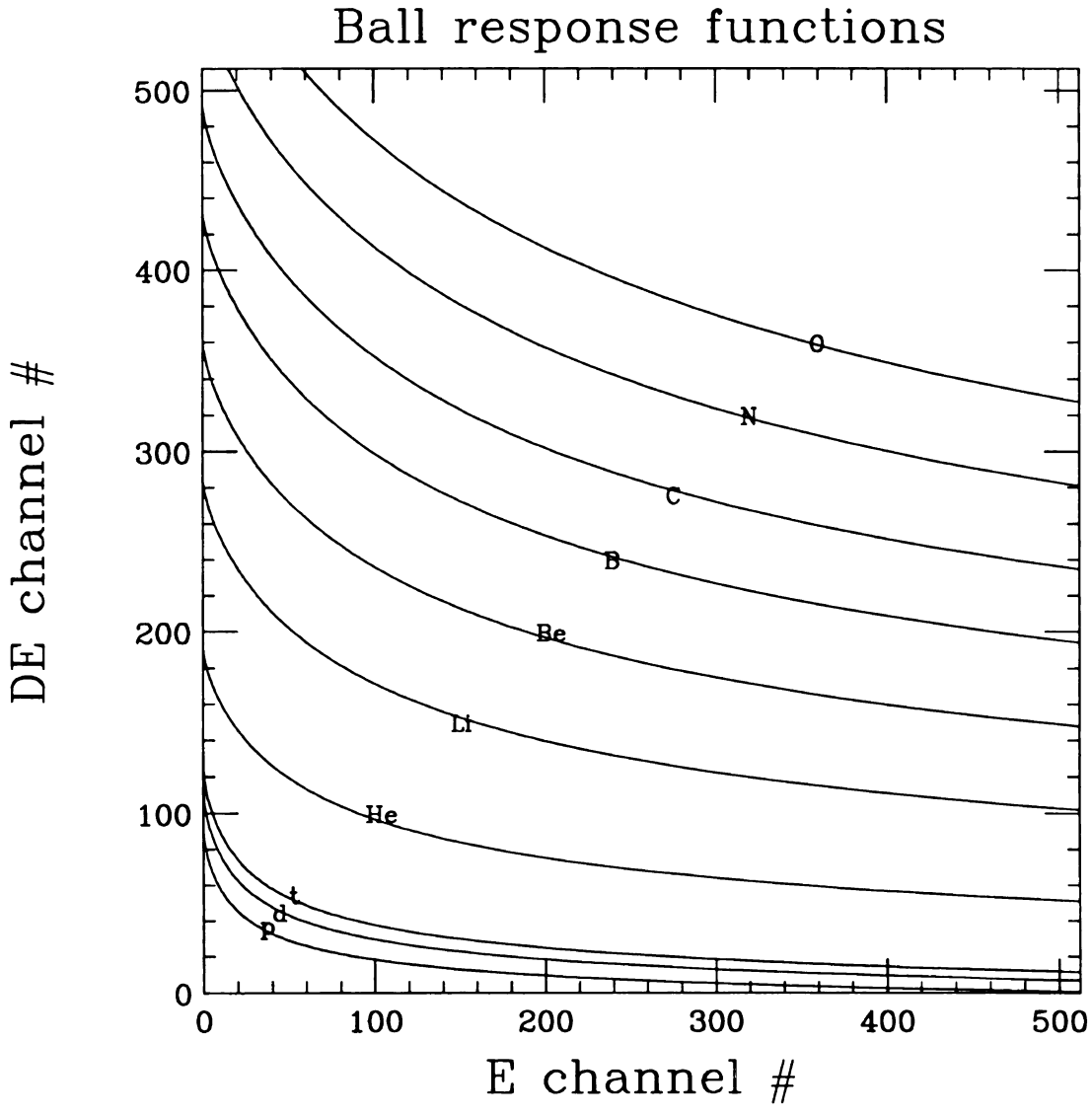

Figure 2.9: The response functions for p,d,t and Z = 2 - 11 for a ball phoswich.

map

tecte

tor. I

conta

tected

2.2.2

The 4-

ization

housing

ule. (S.

of the

ring (cl

6 electr

there ar

gas volu

aluminiz

the cath

cm.

A Fri

Frisch gr

epoxied w

at ground

caused by

is produc

grid consi

map raw channel number into particle type and incident energy. Angles of the detected particles are assigned as the geometric mean angle of the corresponding detector. Using these tables, the raw data tapes are filtered onto "physics" tapes which contain information regarding the Z,A,θ,ϕ, and kinetic energy of each particle detected.

2.2.2 Bragg Curve Counters

The 4π Array contains 55 Bragg Curve spectrometers (BCC) which are gas-filled ionization chambers. The chambers each consist of a hexagonal or pentagonal pyramidal housing of G10 fiberglass which is mounted directly on the face of the phoswich module. (See Figure 2.10.) A 2.5 μm thick aluminum coating is evaporated on the face of the phoswich fast plastic, and this serves as the anode for the BCC. In the first ring (closest to the beam axis) of five hexagonal modules, the anode is separated into 6 electrically isolated segments corresponding to the 6 fast plastic segments. Thus there are effectively 55 BCCs in the 4π Array, even though there are only 30 separate gas volumes. The front pressure windows of the BCCs are made of 900 $\mu g/cm^2$ thick, aluminized kapton. The windows are epoxied to a stainless steel frame and serve as the cathodes for the BCCs. The distance between the cathode and the anode is 13.36 cm.

A Frisch grid is installed in the BCCs parallel to and 1 cm above the anode. The Frisch grid is made of 12.5μm gold plated tungsten wires spaced .5 mm apart, and epoxied with conductive epoxy to a copper strip on the BCC frame. The grid is held at ground potential and serves to shield the anode from the induced image charge caused by the drifting electrons. An approximately radial field within the chamber is produced by using a field shaping grid which lines the inside of the housing. The grid consists of 21 copper strips, each encircling the the volume of the chamber and

spaced between the Frisch grid and the cathode. The strips are linked by 21 1.55 MΩ resistors creating a 21 stage voltage drop between the negative cathode potential and ground.

Charged particles (positive ions) entering the chamber ionize the gas within, and lose energy as they travel. If one plots the rate of this energy loss against the distance of penetration, the functional form is called a Bragg curve. The Bragg curve typically peaks close to the end of the flight path of the particle since the rate of energy loss is greatest when the particle is moving very slowly and spending more time in the field of each particle it encounters. At the very end of flight path, the charge of the ion is reduced due to electron pickup and the energy loss curve decreases quickly. The energy loss falls to zero when the ion becomes a neutral atom.

The electron-ion pairs created by the impinging particle drift along the radial field lines to the cathode and anode. The negative signal produced on the anode is fed into a charge-sensitive preamplifier and integrated. This signal is in turn fed into a shaping amplifier with both a fast and slow time constant. The fast channel differentiates the input signal to obtain the shape of the original signal before integration. A small amount of integration is used to suppress noise. This results in a Bragg curve signal with peak height proportional to the charge of the particle which created it. The slow channel shapes the integrated signal with two stages of differentiation and integration producing a signal whose peak is proportional to the energy of the incident particle. Each of these signals is fed into a separate peak sensing ADC (Silena 4418/v), digitized and written to magnetic tape.

This method of identification will not work if the particle does not stop in the gas volume because the peak of the Bragg curve will not occur in the detector. In that case, the particles that punch through and stop in the fast plastic behind the BCC are identified by the ΔE signal left in the BCC and the E signal left in the

fast plastic. As there are 170 phoswiches, there are effectively 170 BCC/fast plastic telescopes as well. Examples of spectra obtained using both of these methods are shown in Figure 2.11 and Figure 2.12. The BCC vs. fast plastic spectrum shows bands from particles having Z = 2 through 11. Particles just punching into the fast plastic are found along the y-axis. The E vs. Z spectrum shows particles with Z = 3 through 13. Particles punching through the gas volume (and ending up either in the BCC vs. fast plastic or phoswich spectra) are found in the strong line near the y-axis. Particles just punching into the BCC are found in the band near the x-axis. The slope of the Z lines and the hazy area near the punch-in band are due to the choice of gas used in taking the present data.

The BCCs were originally intended to be used with 500 Torr of P5 (95% argon, 5% methane) gas, and operated with -1200 V on the cathode and +500 V on the anode. For the present experiment however, the BCCs are operated at 125 Torr of C_2F_6 with a cathode voltage of -500 V and an anode voltage of +150 V. Running with the heavier gas at a lower pressure put less strain on the pressure windows without a loss in stopping power. However, whereas the drift velocity of the ions in P5 is independent of the field strength, the same is not true of C_2F_6. This caused the the distribution of the ion trail to become somewhat distorted and created a dependence of the peak signal height on the penetration distance. Particles stopping closer to the cathode had larger Z signals than the same species particles stopping later. This effect also caused the loss of resolution for particles stopping very close to the cathode, and resulted in a higher effective threshold for the BCCs. A summary of the characteristics of the BCCs can be found in Table 2.3.

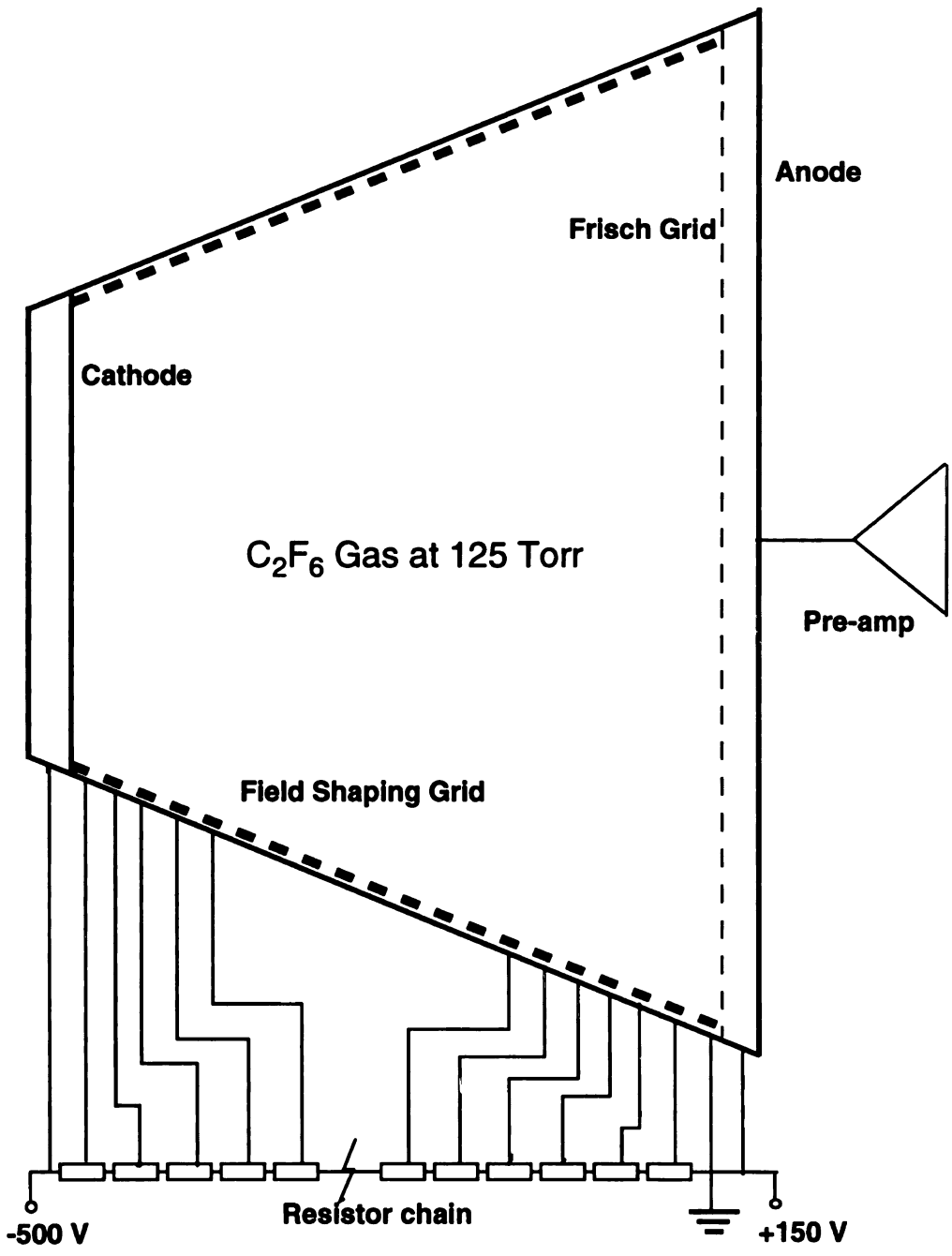

Figure 2.10: Schematic of the MSU 4π Array Bragg curve counter.

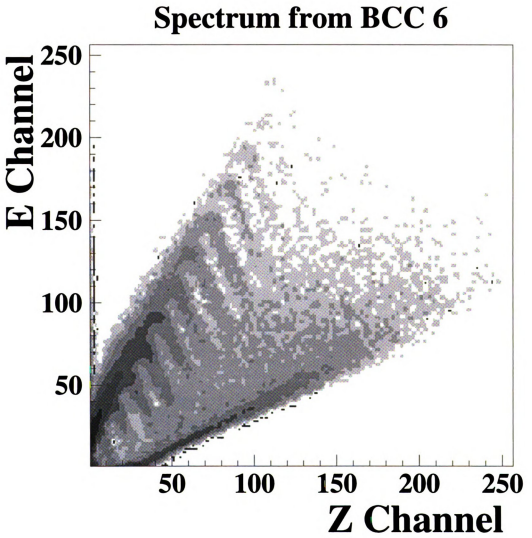

Figure 2.11: Bragg curve spectrum for Ar + Th at 55 AMeV. The signal proportional to the particle energy is plotted on the ordinate, and the signal proportional to the atomic number (Z) of the particle is plotted on the abscissa.

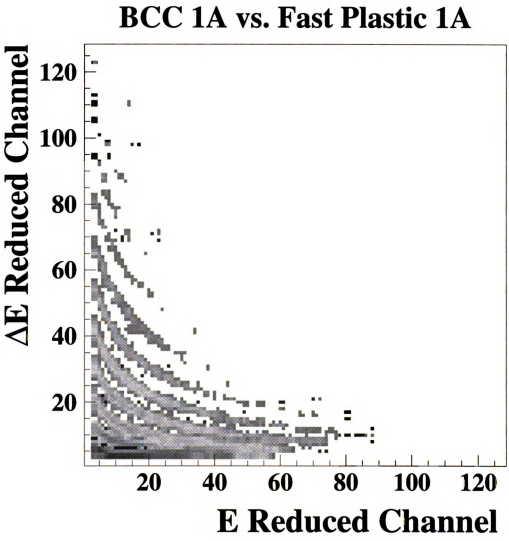

Figure 2.12: BCC vs. fast plastic spectrum for Ar +Th at 55 AMeV.

Table 2.3: Specifications of the Bragg curve counters.

Characteristic	BCC vs. FP	BCC E vs. Z
Polar Angle region (^{o})	18 - 162	18 -162
Solid Angle coverage (%)	84	84
Z identification	2 - 18	3 - 18
Energy Threshold (AMeV)		
Lithium	4.0	2.0
Boron	5.0	3.0
Carbon	5.5	4.0

BCC Calibration

The calibration of the Bragg curve vs. fast plastic (ΔE/E) spectra is accomplished in a fashion similar to the phoswich calibration. The difference lies in that the gate lines as well as the response functions are generated from a known functional form, whereas with the phoswiches the gate lines are drawn in by hand. The response function for the fast plastic has the same form as that used for the slow plastic in the phoswich calibration, since in this case the fast plastic is the stopping detector. The form is

$$CH_f = \alpha E_f^{1.4}/(A^{0.4}Z^{0.8}). \tag{2.3}$$

A response curve for the BCC was originally determined to be linear:

$$CH_{BCC} = \beta E_{BCC} \tag{2.4}$$

during a field test using a BCC with P5 gas and corresponding specifications listed above [Cebr 91] (See Figure 2.13). In that test run, it was determined that the BCC energy response was independent of particle type. However, in the present experiment, it is necessary to introduce a charge dependence into the energy calibration as an exponent in the energy term.

$$CH_{BCC} = \beta E_{BCC}^{C(Z)} \tag{2.5}$$

Using the response functions, a template is made to which all BCC vs. fast plastic spectra are gain matched. This time using the energy loss program ELOSS, look-up tables are made from the template which map each point in the two-dimensional spectra to the corresponding energy, Z, and A. The tables are used to filter the raw data to tape. The template used for the present experiment is shown in Figure 2.14.

The calibration for the data obtained for particles stopping in the Bragg curve is done in a slightly different fashion. For each of the 55 detectors, customized gate lines are drawn for each Z as shown in Figure 2.15, resulting in 55 individual templates. The response curves are created by selecting the point in the spectra representing the energy where each particle type punched out of the gas volume. This is found by looking for the point where the Z line bends over and blends with the punch-out line, and is marked in Figure 2.15 by the stars. The y-channel number corresponding to this point is then matched with the calculated punch-out energy (using the energy loss code ELOSS) for each Z. Doing this for several particle types produces a curve such as the one shown in Figure 2.16. This curve is then fit with a polynomial using a least squares routine. The resulting function is used to create a table mapping channel number to energy. The response is not quite linear as found in the test run. A quadratic term on the order of 10^{-3} was needed obtain an accurate fit.

This method has the disadvantage that a separate template must be made for each detector. However, because of the relatively small number of detectors (55), the relative ease of producing the templates, and the fact that the gains were not changed during the experiment this disadvantage proved to be small.

2.2.3 Multi-Wire Proportional Counters

Mounted in front of each of the Bragg curve counters in the 4π Array are 30 low pressure multi-wire proportional counters (MWPCs). The frame of each MWPC is

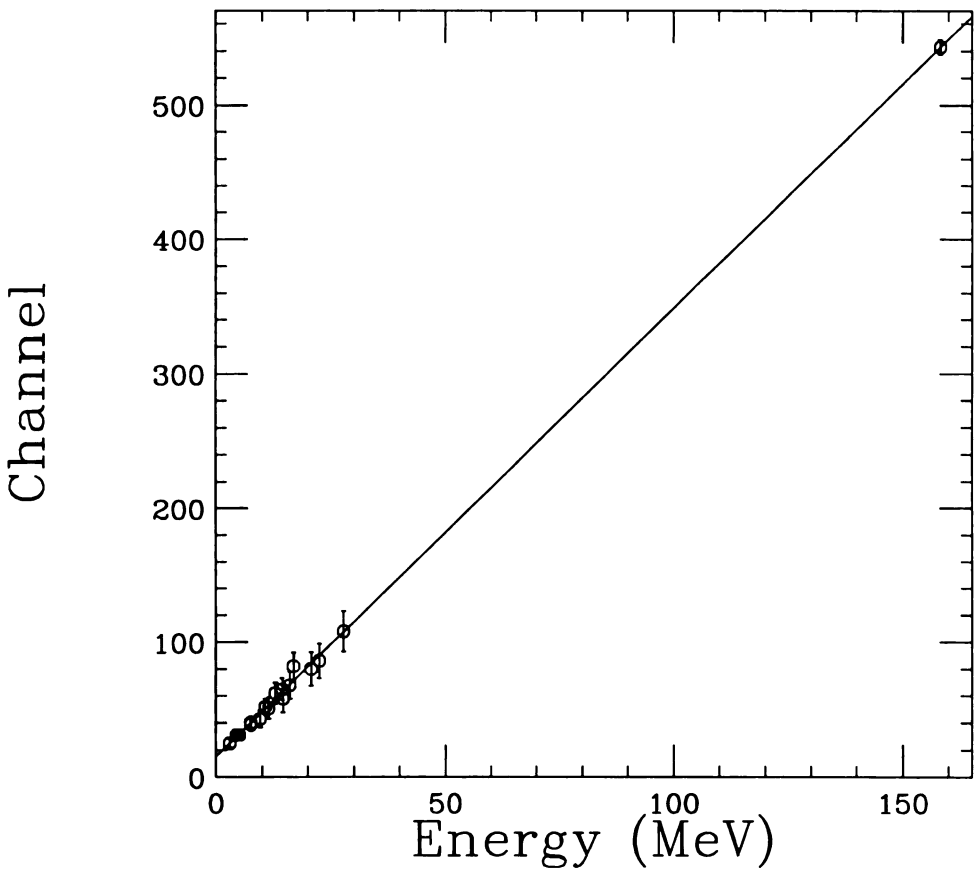

Figure 2.13: Bragg curve response function from test run.

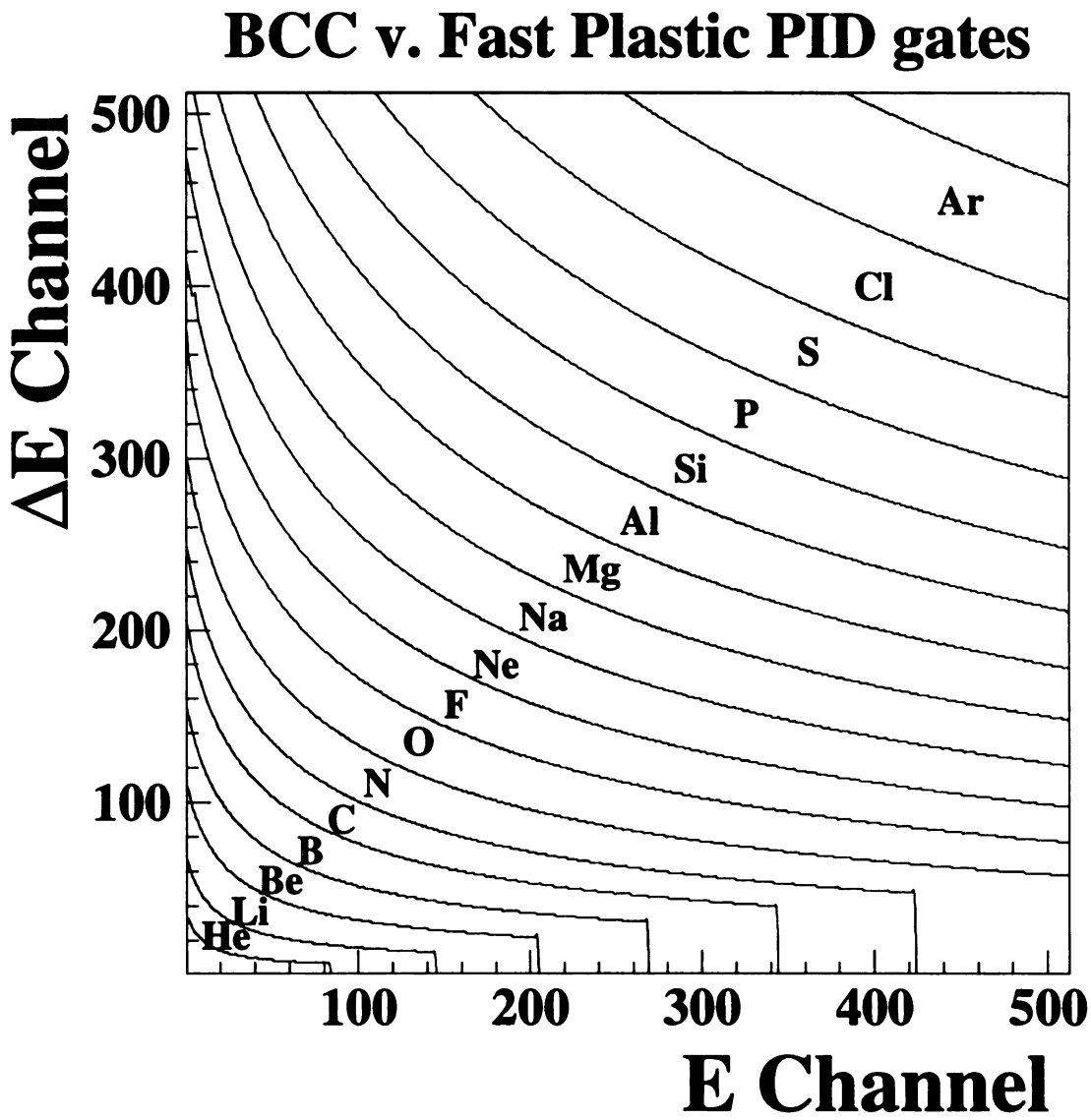

Figure 2.14: Template for a BCC vs. Fast Plastic spectrum.

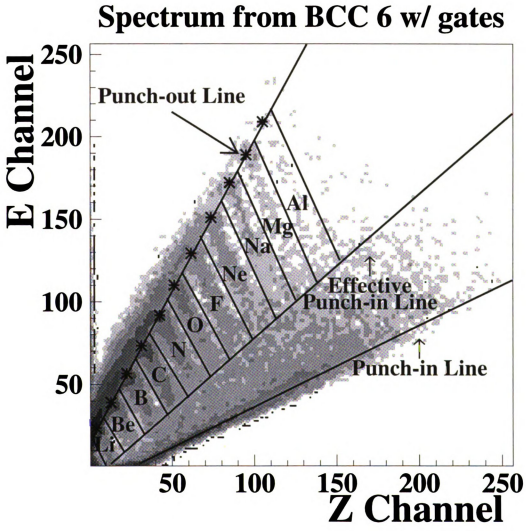

Figure 2.15: Same spectrum as 2.11 with gates and calibration points superimposed.

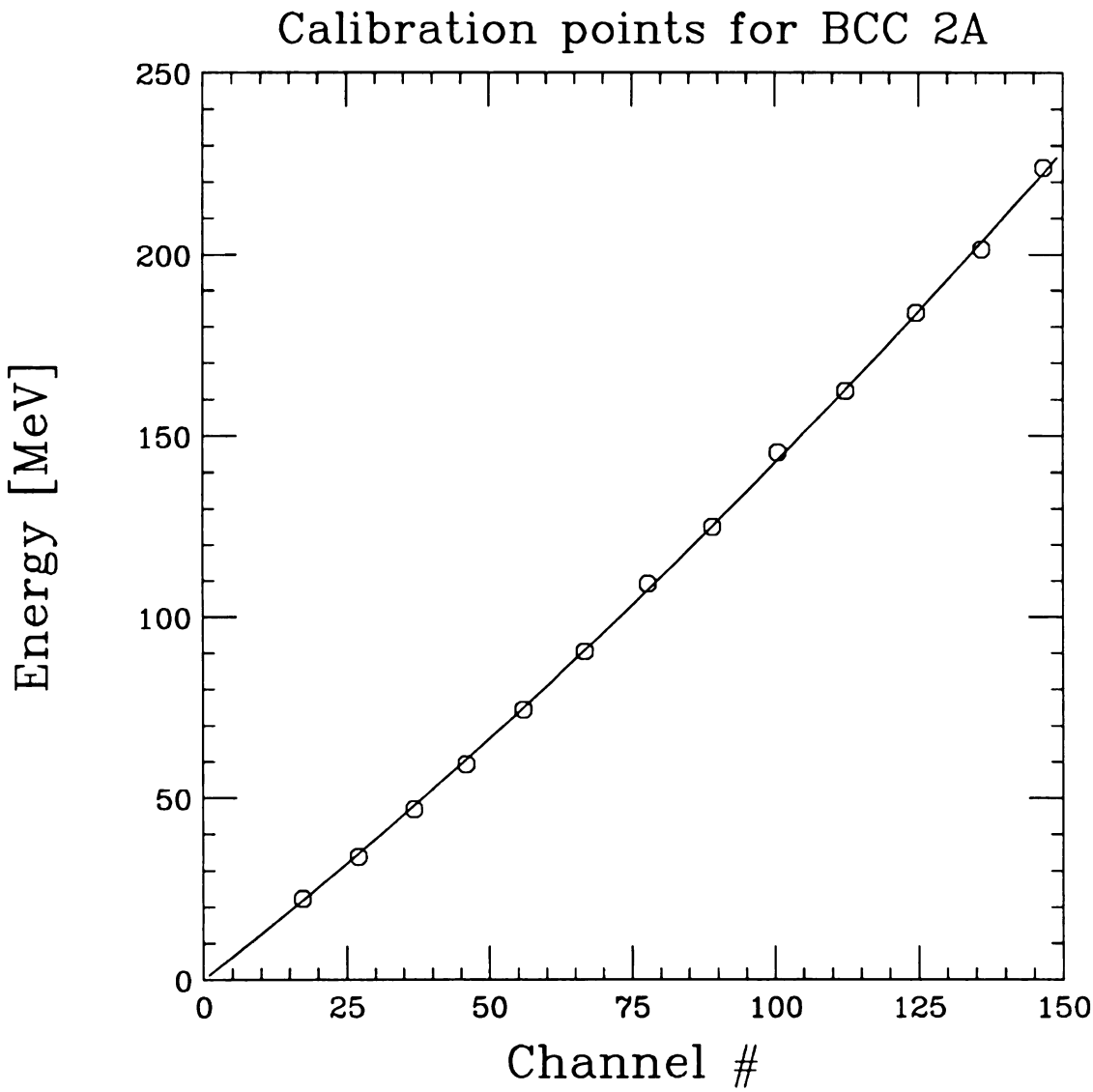

Figure 2.16: Calibration curve for a BCC.

constructed of 6 layers of G10 fiberglass with stretched kapton foils (0.3 mil) forming the front and rear pressure windows. The anode is mounted in the center layer and consists of a plane of 12 μm-thick goldplated tungsten wires spaced 1 mm apart. This layer is in between two cathode planes made of stretched polypropylene foil. A layer of aluminum is evaporated on the surface of the foil and is divided into 5 mm wide strips connected by a 1 mm wide strip of resistive (5 kΩ) nichrome. Figure 2.17 shows an internal view of the MWPC layers. The cathode planes are separated by approximately 1 cm, and the entire gas volume between the pressure windows is approximately 3 cm thick.

For the present experiment the MWPC was pressurized with 5 Torr of isobutane gas and +500 V was applied to the anode. The cathodes are held at ground potential. Particles impinging on the detector create electron-ion pairs which drift toward the cathode and anode creating more ionized pairs along the way. This is known as an avalanche effect and results from the combination of gas, pressure, and voltage used in the detector.

The positive charges are collected from both ends of the cathodes' nichrome strips. Using the principle of charge division, the position of the incident particle along the strip is extracted. In this process, the difference in the two charges collected at each end of the MWPC is divided by the sum of the two charges. This gives a fraction corresponding to the distance of the impinging particle from one end of the detector. For example, if the fraction is 0.25, the particle was one quarter of the way from one end of the strip. As there are two cathodes oriented with their nichrome strips crossing at a fixed angle (See Figure 2.17), the X-Y position of the particle's punch-in point on the face of the detector can be determined.

In a test run, an MWPC was covered with a mask that had slits of known width sliced in it. By irradiating the face of the MWPC with fission fragments and mea-

suring the resulting position spectrum, we were able to determine that the MWPCs have an angular resolution of 1° .

A position spectrum of particles produced in 15 AMeV Ar + Th collisions and measured in the MWPCs is shown in Figure 2.18. In the figure, the polar and azimuthal angular positions of the detected particles are unfolded and displayed. Most of the MWPCs were working when this spectrum was recorded; dead detectors are identifiable as white regions. Shadowing due to the target frame can be seen in the region near 90° (lab).

The MWPCs were designed to detect fission fragments. Due to the low pressure and small volume of gas used, they are not as efficient for very light, fast particles. However, IMFs can leave significant signals in the MWPCs and must be separated from the fission fragments. This is done by using the BCC behind the MWPC as a veto detector. Particles leaving a signal in the MWPC and punching into the BCC are designated as not being fission fragments.

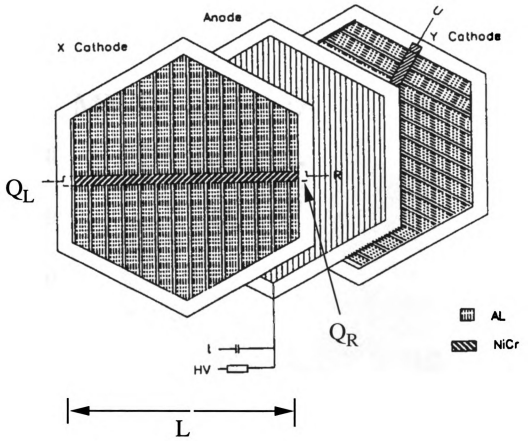

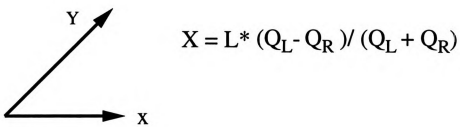

Figure 2.17: Exploded view of the MWPC. The X in the equation is the position of the particle along the x-axis. Q_L and Q_R are the charge collected on the left and right ends of the cathode, respectively.

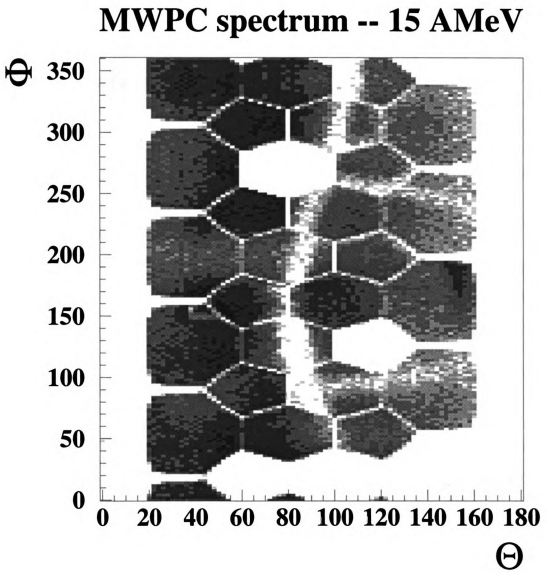

Figure 2.18: MWPC spectrum from 15 AMeV Ar + Th collisions

Ch

Mc
De

3.1

In this c
tion in
will stud
folding a

3.2

In investig
the fission
between th
frame. In t
180° apart a
boosted into
to the veloc
graphically i

Chapter 3

Momentum Transfer and Deposited Energy

3.1 Introduction

In this chapter we discuss the evolution of the momentum transfer and energy deposition in $^{40}Ar + ^{232}Th$ collisions as beam energy is increased from 15 to 115 AMeV. We will study these topics via inclusive and exclusive measurements of fission fragment folding angles, fission fragment azimuthal angles, and charged particle production.

3.2 Folding Angle Distributions

In investigating heavy fissionable systems, a great deal can be learned from studying the fission fragment folding angle distributions. The folding angle is simply the angle between the two vectors defining the trajectory of each fission fragment in the lab frame. In the frame of the fissioning nucleus, these vectors would be approximately 180° apart as required by momentum conservation. However, when the fragments are boosted into the lab frame, the folding angle is reduced by an amount directly related to the velocity of the moving source [Back 80, Viol 82, Viol 89]. This is illustrated graphically in Figure 3.1.

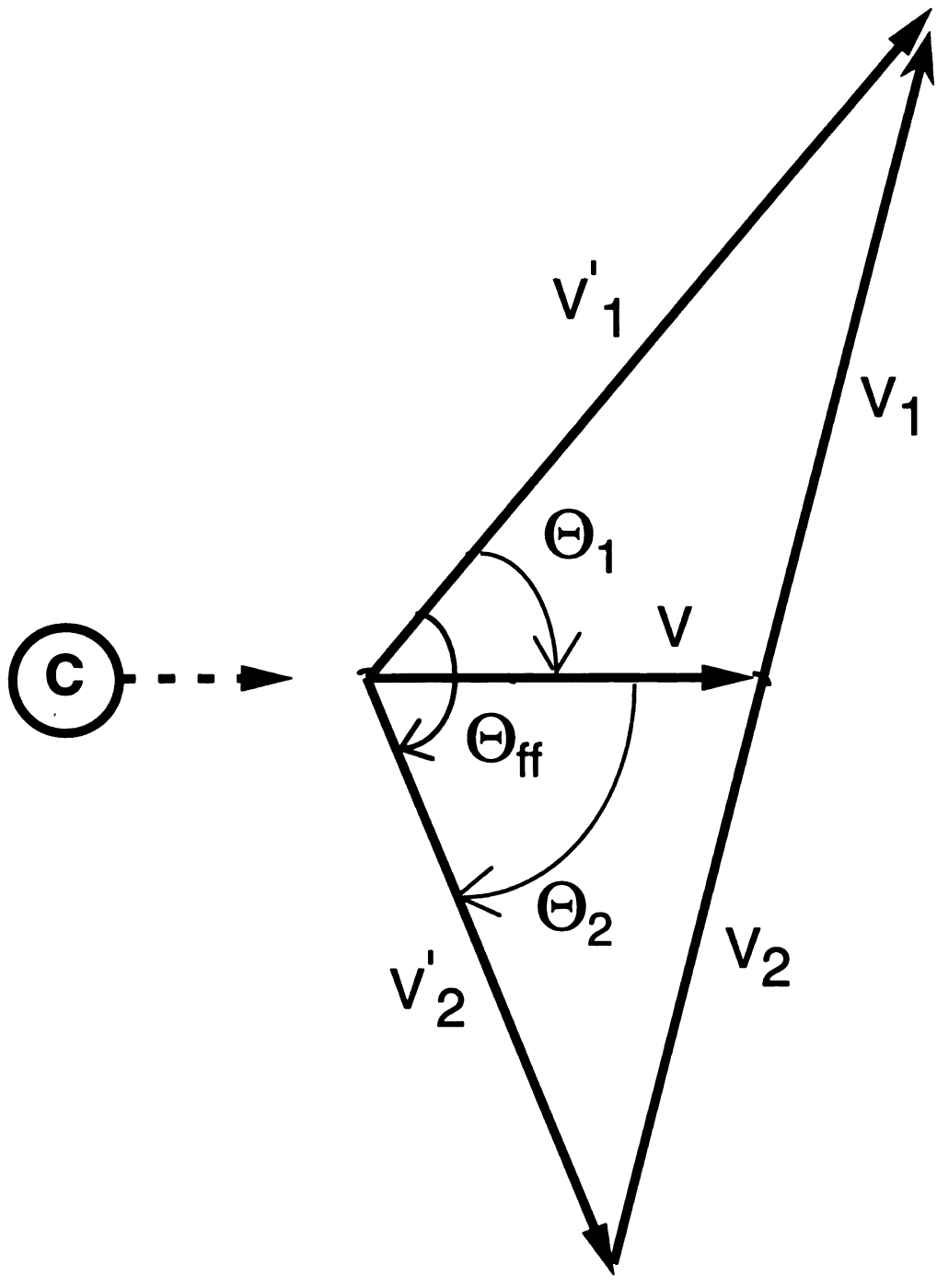

Figure 3.1: Cartoon illustrating the transformation of a fission event into the lab frame. The compound nucleus "C", traveling at speed V undergoes pure binary fission. The fragment velocities are collinear in the moving frame (unprimed), but in the lab frame (primed), the angle between them is reduced to Θ_{ff}.

Th

fissio

where

adequa

axis. H

energie

all poss

we use

where f_i

assumin

Figu

the ^{40}Ar

trigger (

teristics

be loosel

at a foldi

tile graze

momentu

sion. The

been show

increases

present da

The folding angle is usually defined as the sum of the polar angles of the two fission fragments in the lab frame [Viol 82, Tsan 84, Viol 89]. That is

$$\Theta_{ff} = \Theta_1 + \Theta_2, \tag{3.1}$$

where Θ_1 and Θ_2 are measured with respect to the beam axis. This definition is adequate if the fission fragments are emitted close to a common plane with the beam axis. However, as will be shown below, this is often not the case at high bombarding energies. Because of the ability of the 4π Array to detect fission fragments in almost all possible planes, we need a more general definition of opening angle. For this reason we use

$$\Theta_{ff} = \cos^{-1}(\mathbf{f_1}\cdot\mathbf{f_2}), \tag{3.2}$$

where $\mathbf{f_1}$ and $\mathbf{f_2}$ are the unit vectors of the lab trajectories of the fission fragments, assuming an emission from the center of the lab coordinate system.

Figure 3.2 shows the inclusive distributions of fission fragment folding angles for the ^{40}Ar + ^{232}Th system at all nine energies studied. These data were taken with a trigger (called MWPC 1) requiring one MWPC to fire. There are two main characteristics in each of these distributions resulting from different interactions that can be loosely classified into two groups. The peak that appears in all the distributions at a folding angle of $\sim 165^\circ$ is produced by peripheral collisions in which the projectile grazes the target [Viol 82, Poll 84, Conj 85, Viol 89, Leeg 92]. Very little linear momentum transfer (LMT) occurs, but the ^{232}Th target is excited sufficiently to fission. The resulting fragments are emitted almost colinearly in the lab frame. It has been shown in a previous experiment [Conj 85] that the cross section for this reaction increases only slightly in the 25 - 45 AMeV energy range, and other work with the present data [Yee 95, Yee 95b] extends this conclusion up to 115 AMeV.

Figure 3.2:
collected wi
select fissio

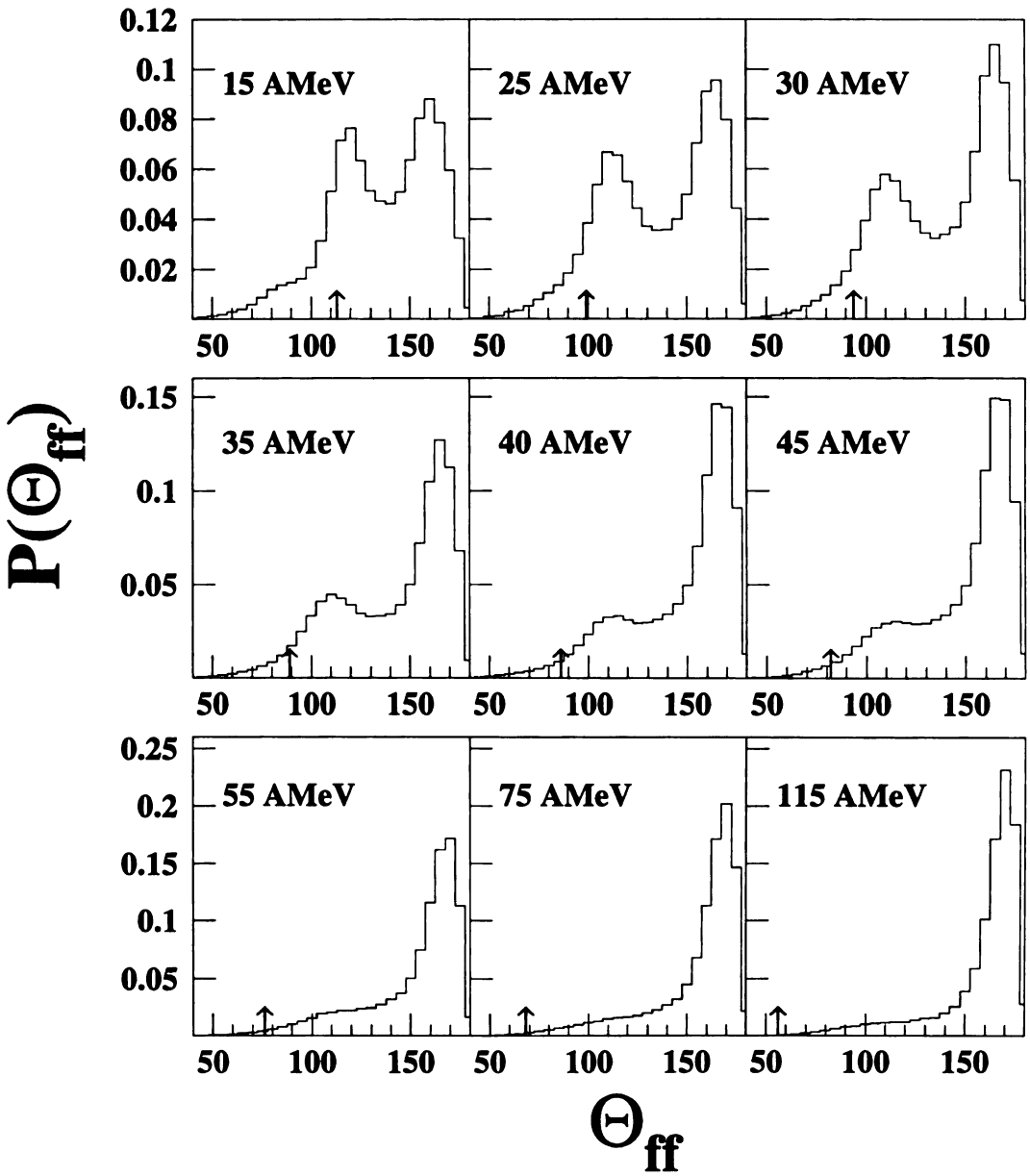

Figure 3.2: Impact parameter inclusive folding angle distributions. These data were collected with a trigger requiring at least one MWPC to fire. Additional criteria to select fission events were applied off-line.

Th

with b

the en

This p

[Back

collisio

If this

[Viol 8

velocity

Zoln 78

importa

AMeV t

to the g

[Viol 89,

particles

At highe

$(A \geq 7)$ i

heavier fr

pure bina

quantitat

Even

more pred

fusion-fissi

be at the

this peak g

result has

The other obvious characteristic of these folding angle distributions does change with beam energy, and it is this phenomenon that motivated the present study. At the energies between 15 and 35 AMeV, a sharp peak appears between 110° and 120° . This peak results from central, high LMT collisions that have been studied extensively [Back 80, Awes 81, Viol 82, Poll 84, Tsan 84, Conj 85, Viol 89, Leeg 92]. In these collisions, the projectile and target form a fused system that subsequently fissions. If this fusion is complete, this system moves with the velocity of the center of mass [Viol 82]. At higher energies, the mass transfer is not complete; both the size and velocity of the system formed are smaller than in the complete fusion case [Viol 82, Zoln 78]. This effect has been explained as being due to two distinct processes, each important in a particular energy range. At energies between ~10 AMeV and ~40 AMeV the decrease in the momentum transfer in central collisions has been attributed to the growing importance of preequilibrium emission of nucleons and light particles [Viol 89, Awes 81, Troc 89]. This process carries away momentum in a spray of particles and reduces the momentum available to accelerate the compound system. At higher energies, the probability of the statistical emission of heavier fragments ($A \geq 7$) in coincidence with the fission fragments increases [Poll 93, Schw 94]. These heavier fragments are capable of carrying off large amounts of momentum and the pure binary nature of fission is lost. Momentum transfer in this system will be treated quantitatively later in the chapter.

Even at the lowest energy studied here, incomplete fusion is already occurring more predominately than complete fusion, and this is reflected in the location of the fusion-fission peak. Were complete fusion occurring predominately, the peak would be at the location indicated in each frame by the arrow. As beam energy increases, this peak gradually diminishes until, at 115 AMeV, it has apparently vanished. This result has been seen before, and has been interpreted as signifying the disappearance

of the

[Conj

focus o

In

the da

2) req

the eve

periphe

The eff

almost

the low

remaind

that a fi

further e

Figur

using tra

is explain

approxim

At all ene

like events

which a hi

is in the sa

distributio

out, the pe

component

continuity w

of the process of fusion-fission and perhaps the onset of a new decay mechanism [Conj 85]. Whether or not either of these scenarios is actually occurring will be the focus of the better part of this thesis.

In Figure 3.3, the folding angle distributions are again displayed, but in this case the data were taken with a different hardware trigger. This trigger (called BALL-2) required two particles to be detected in the main ball phoswiches in order for the event to be recorded. This trigger has the effect of reducing the contribution of peripheral collisions, which is helpful as we are interested in isolating central events. The effect of the trigger is obvious in the 15 AMeV case where the low LMT peak is almost completely absent and the dominant feature is the fusion-fission peak. With the low LMT component suppressed, a shoulder in the distribution that could be the remainder of a high LMT component is visible even at 115 AMeV, perhaps signifying that a fission-like process is still occurring at this energy. However, we will need to further exclude the peripheral collisions in order to make this determination.

Figure 3.4 displays the folding angle distributions for central collisions as defined using transverse kinetic energy (E_T). (This method of selecting central collisions is explained in detail in Appendix A.) The number of events in this distribution is approximately 10% of the number in the inclusive distribution shown in Figure 3.3. At all energies, there is a single peak which can be associated with high LMT, fission-like events. If one compares the distributions in Figure 3.4 to those in Figure 3.3 in which a high LMT component is visible, it is apparent that the peak selected with E_T is in the same place ($\sim 110^\circ$) as the high LMT peak in the impact parameter inclusive distribution. However, as the high LMT peak in Figure 3.3 becomes difficult to make out, the peak in Figure 3.4 remains easily distinguishable. Although, this high LMT component is diminished in absolute size as beam energy increases [Yee 95], this continuity with the lower energies is strong evidence that a fission-like process is still

$P(\Theta_{ff})$

Figure 3.3
collected
phoswiche

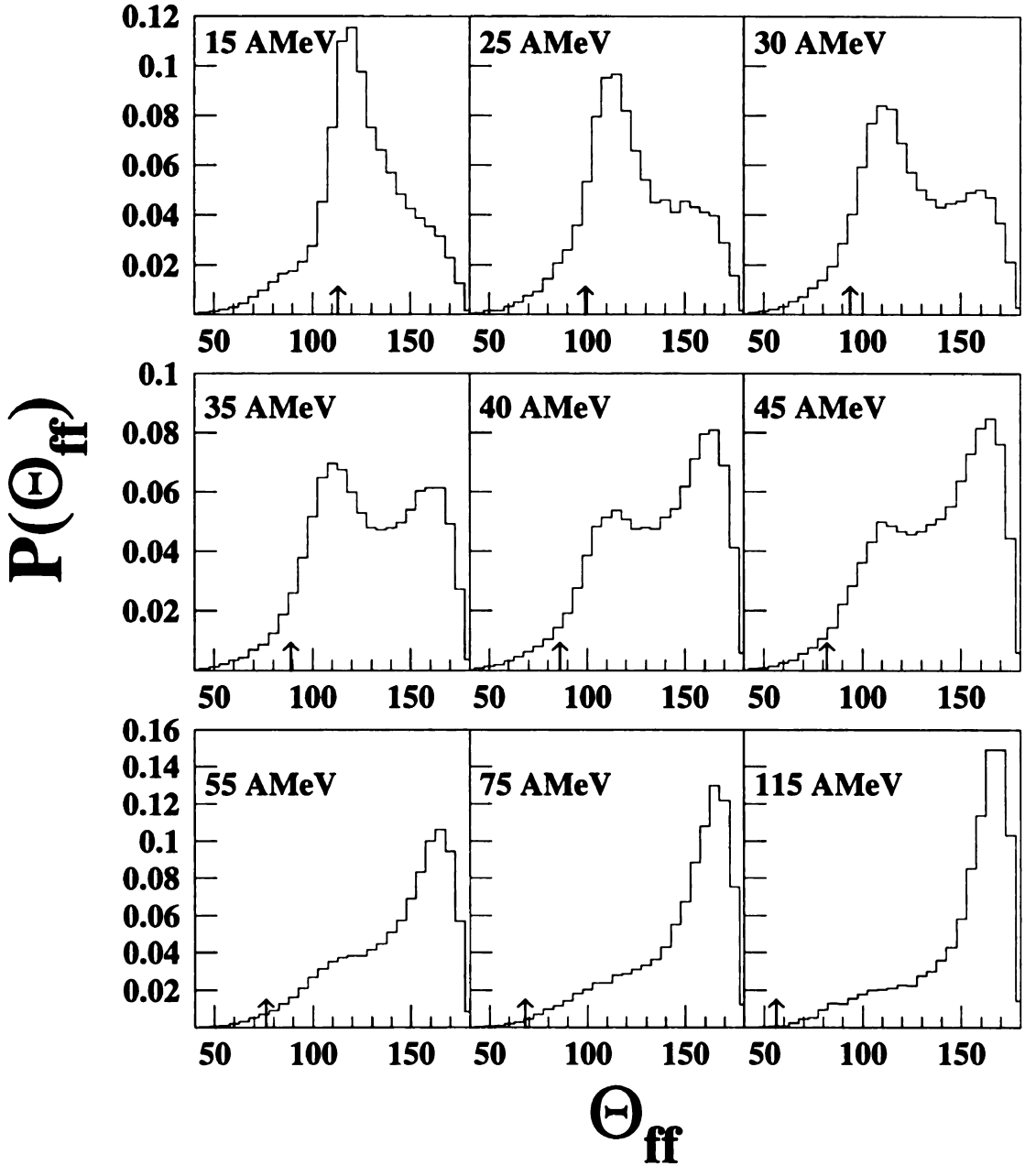

Figure 3.3: Impact parameter inclusive folding angle distributions. These data were collected with a trigger requiring at least two particles to trigger the main ball phoswiches. Additional criteria to select fission events were applied off-line.

occurr

Th

the hig

crease

made s

shoulde

particle

At ener

[Viol 89

[Schw 9

between

extendin

cesses ha

in the fo

3.3 A

Another c

mechanis

fragments.

the planes

perfectly c

another, Φ

Figure 3

and high L

from events

occurring in central events even at 115 AMeV.

There is also some evidence in Figure 3.4 that there is a change in the character of the high LMT fission-like events as beam energy increases. There is a noticeable increase in the width of the distributions with beam energy, although this observation is made slightly difficult by the contamination of some target fission events on the right shoulder of the peak. Kinematical broadening can be caused by the emission of other particles from the nucleus during fission or from the daughter fragments after fission. At energies near the Coulomb barrier it is attributed primarily to neutron emission [Viol 89]. At higher energies, the increased probability of complex fragment emission [Schw 94, Viol 89] makes this picture more complicated. Asymmetric mass division between the fission fragments can also lead to a tail in the folding angle distribution extending toward smaller angles [Tsan 83]. Possible changes in the fission-like processes having to do with the coincident emission of lighter particles will be discussed in the following sections.

3.3 Azimuthal Distributions

Another characteristic of fission that can tell us about the evolution of the reaction mechanism with beam energy is the relative azimuthal angle between the fission fragments. This angle is depicted in Figure 3.5, and is defined to be the angle between the planes containing each fission fragment and the beam axis (Φ_{ff}). That is, for perfectly coplanar fragments, Φ_{ff} is zero, and for fragments perpendicular to one another, Φ_{ff} is 90° .

Figure 3.6 illustrates the evolution of Φ_{ff} with beam energy, for both low LMT and high LMT collisions, as determined by the folding angle. The dashed curves are from events containing fission fragments with a folding angle between 150° and 180° ,

$P(\Theta_{ff})$

0.
0.
0.
0.
0.
0.
0.0
0.0
0.0
0.0

Figure 3.4: I
verse kineti
data.

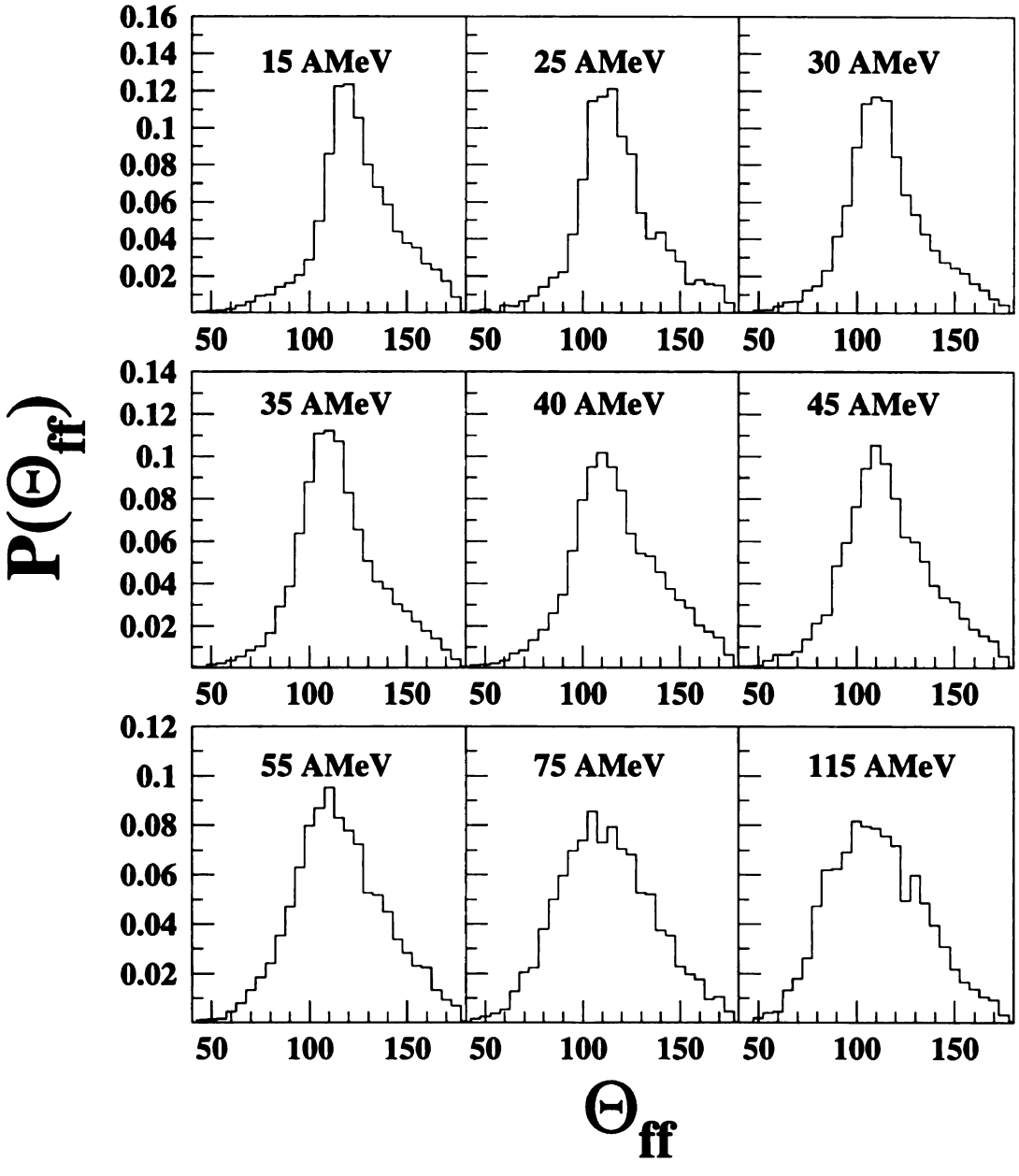

Figure 3.4: Folding angle distributions from central collisions as selected using transverse kinetic energy. Events represent the 10% most central from the BALL 2 trigger data.

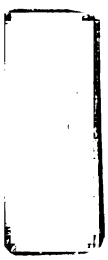

i.e. in the target fission peak. These distributions show no change in width as beam energy increases, giving an indication that there is little change in the character of these peripheral reactions as beam energy increases. The solid curves are selected from events in the high LMT peak, and these show significant widening as a function of beam energy to the point where the distribution is almost flat at 115 AMeV.

The widening of the the Φ_{ff} distributions for high LMT events indicates a change in the character of the reaction mechanism as beam energy increases much more dramatically than does the widening of the Θ_{ff} distributions. The Φ_{ff} distributions suggest that the fission process is not purely binary at the highest energies. It is well known that light charged particles emitted either from the nucleus during fission or from the daughter fragments after fission can deflect the trajectories of the fragments out of a common plane with the beam axis [Tsan 84, Viol 89]. However, the degree of non-coplanarity of the fragments in the highest energy systems studied suggest that there must be more massive fragments emitted most likely simultaneously with the fission fragments in order for the values Φ_{ff} to be so drastically altered from zero [Schw 94]. In the following section we will present evidence that supports this claim of massive fragment production in conjunction with the fission fragments.

3.4 IMF and LCP Production

One of the most fundamental observables one can examine when investigating nuclear reactions is the production of charged particles. Trends in the mean number of intermediate mass fragments and light charged particles can provide insights into the amount of energy that is being deposited into the composite system as beam energy increases. A large body of evidence links excitation energy deposited in the nucleus with the production of IMFs [Fiel 86, Troc 89, Pori 89, Ogil 91, deSo 91, Sang 92],

Figure 3.
fectly co

and show

importa

In Fig

event, ve

criteria a

data set.

well belo

certainly

Array as a

collisions.

each event

the solid c

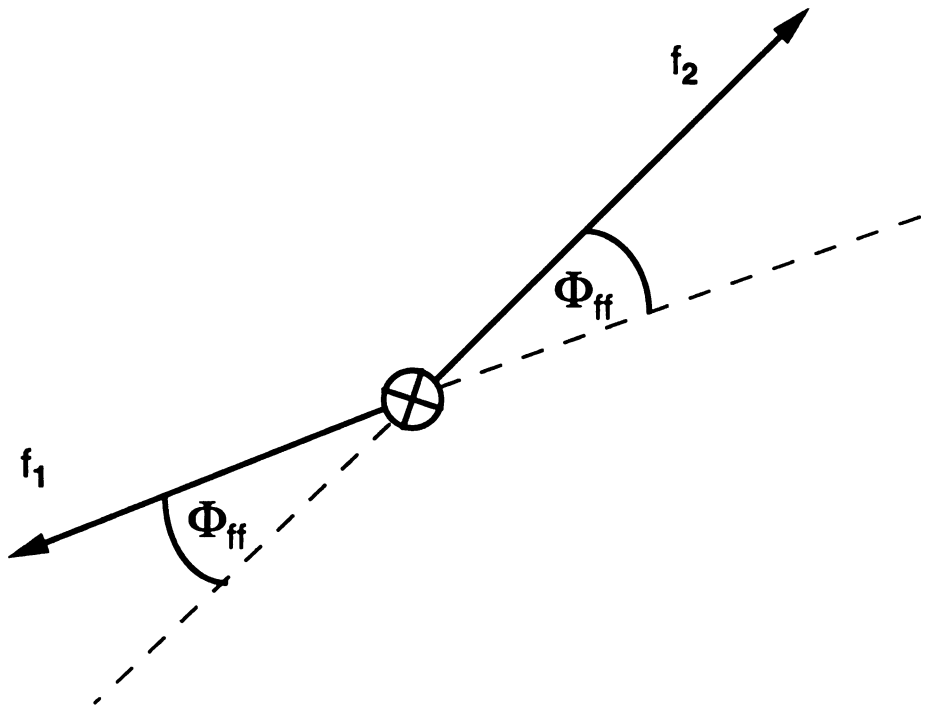

Figure 3.5: Cartoon illustrating the fission fragment azimuthal angle Φ_{ff}. For perfectly coplanar events, $\Phi_{ff} = 0$.

and shows that large multiplicities of IMFs are present if multifragmentation is an important decay process [Warw 83, Camp 84, Desb 87, Gelb 87, Bowm 91].

In Figure 3.7, we plot the mean IMF multiplicity, $\langle N_{IMF} \rangle$, determined event by event, versus the lab projectile energy E_{beam}. The various symbols represent selection criteria as shown in the inset. The open squares represent $\langle N_{IMF} \rangle$ for the inclusive data set. These data show that, above 35 AMeV, IMF production saturates at a value well below $\langle N_{IMF} \rangle = 1.0$. However, this impact parameter inclusive measurement certainly mixes together a variety of reaction mechanisms. By again using the 4π Array as an impact parameter filter, we can make an exclusive measurement of central collisions. Centrality was determined using the total transverse kinetic energy (E_T) of each event (See Appendix A). The $\langle N_{IMF} \rangle$ values for these central events, as shown by the solid circles, are well above the inclusive data at all energies shown. The excitation

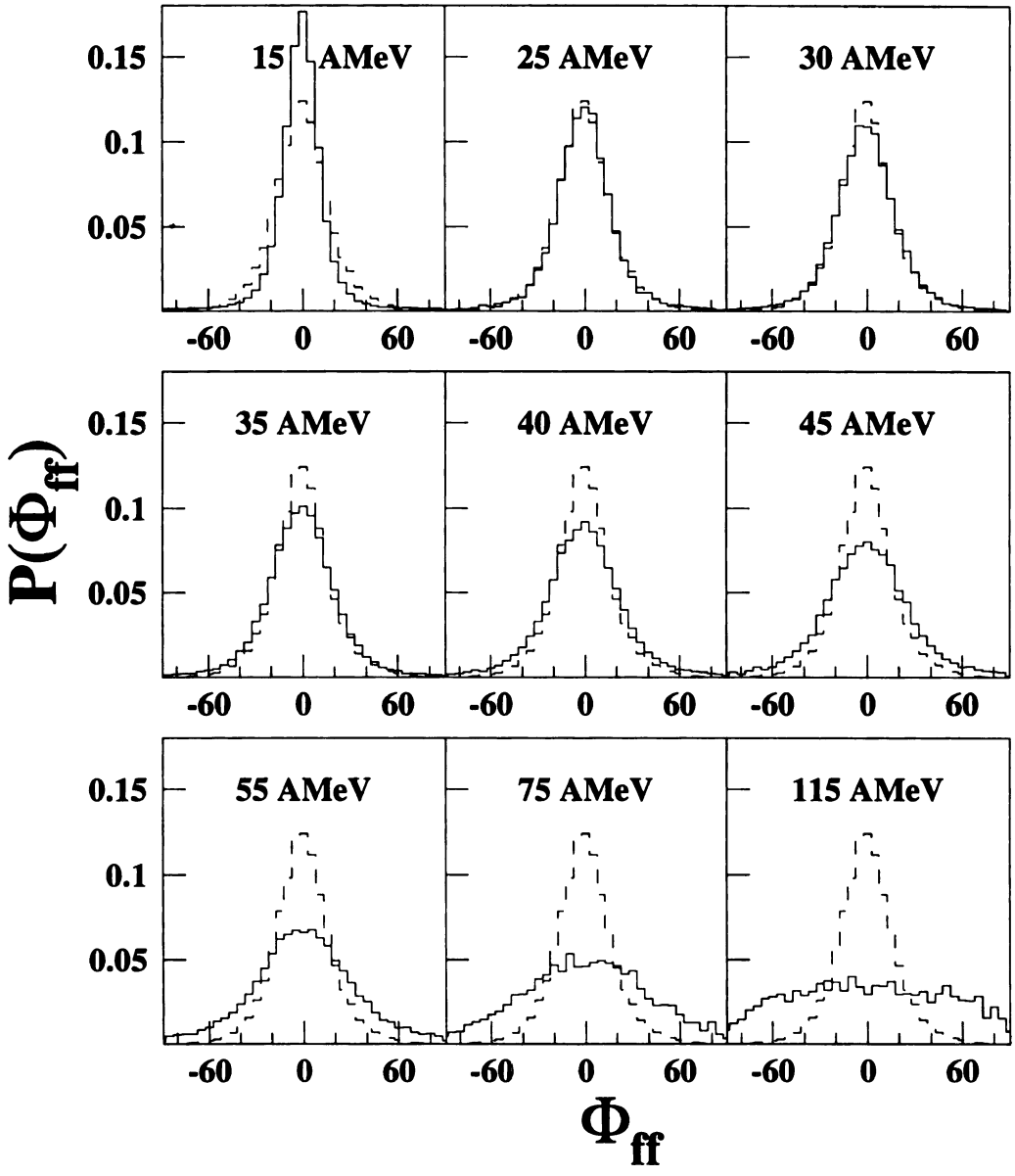

Figure 3.6: Fission fragment azimuthal angle Φ_{ff} distributions for low LMT events (dashed lines) and high LMT events (solid lines).

function increases steadily with beam energy and shows no sign of saturation.

The open triangles in Figure 2a show $\langle N_{IMF} \rangle$ when the same cut is made on central events with the further requirement that two fission fragments are detected in each event. Here, a subset of events is obtained having a relative size varying from ~5% (at 15 AMeV) to ~1% (at 115 AMeV) of the number of all central collisions. The excitation function for this subset then falls between the inclusive data and the data with only the E_T cut. The trend of these data is consistent with the previous statement (and previous observations [Schw 94, Yee 95, Yee 95b]) that the fission fragments are being emitted increasingly out-of-plane as beam energy increases. Further work by Yee et al. [Yee 95b], has provided evidence that these IMFs are not emitted primarily from the fission fragments at beam energies above $\sim 45 AMeV$, but are emitted at a time closer to scission. The shift of the excitation function to lower values of $\langle N_{IMF} \rangle$ than that of the data gated on only E_T occurs because we require a large fraction of the mass to be bound in two large fragments.

In the bottom frame of Figure 3.7, we plot the mean charge bound in light charged particles, $\langle Z_{LCP} \rangle$, versus beam energy, with the same gates as applied in Figure 2a. As in the above plot, the impact parameter inclusive curve saturates after ~30AMeV while the curve selected with only E_T increases steadily. For this system, Jiang et al. [Jian 89] measured a saturation in mean LCP production in central collisions – as defined by neutron multiplicities – at beam energies above 30 AMeV, and determine that the excitation energy is saturating also. Based on the comparison of the trends of our inclusive and central $\langle N_{IMF} \rangle$ curves, we suggest that this previous result was due to the less stringent exclusion of peripheral collisions in the events used to determine mean LCP multiplicity. Our conclusion is supported by Utley et al. [Utle 94], who measure a much higher excitation energy for the 40 AMeV ^{40}Ar + ^{232}Th system than do Jiang et al., although they both use a similar technique. The bottom frame of

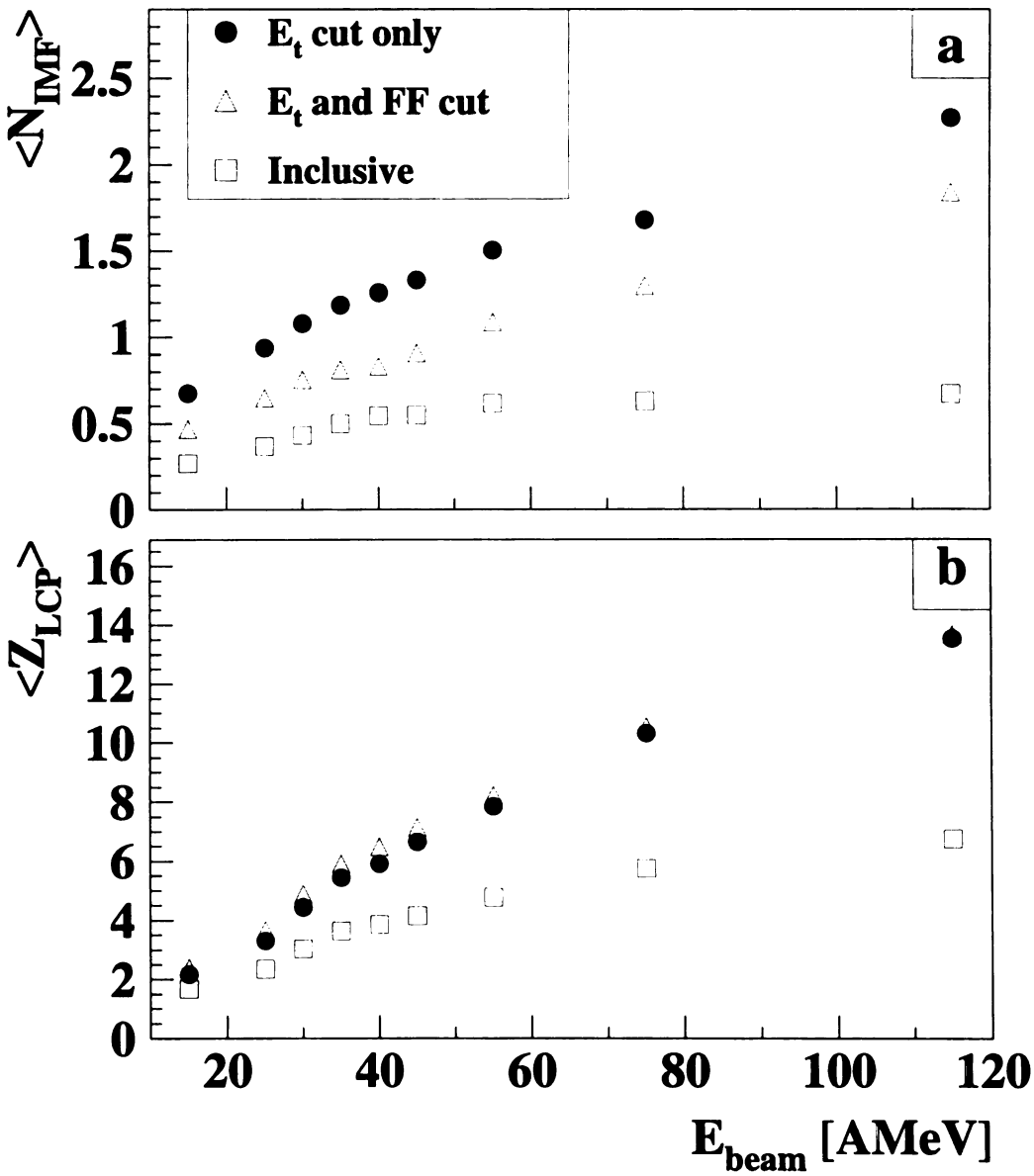

Figure 3.7: Top frame: Average IMF multiplicities plotted versus beam energy. The various symbols represent criteria used to select subsets of events, and are defined in the inset. Bottom frame: Average charge bound in light charged particles versus beam energy for the same selection criteria.

Figure 3.7 also shows that there is little difference between the curve gated on E_T and FFs and the curve gated on only E_T. This would seem to indicate an insensitivity of LCP production to the formation of fission fragments versus IMFs in these data.

The steady increase of the curves gated on E_T in Figure 3.7 suggests that increasing amounts of energy are being deposited in this system in central collisions. The evidence of this increase is contrary to the results of at least one previous experiment, [Jian 89] but in qualitative agreement with several others [Conj 85, Ethv 91, Utle 94]. This observation leaves open the possibility that a change in the dominant reaction mechanism to multifragmentation could be occurring as beam energy increases. However this determination is difficult to make based on IMF multiplicities alone. If a system of this size is multifragmenting one may expect to see more IMFs on average than the $\langle N_{IMF} \rangle$ reached at 115 AMeV, which is less than 2.5. Recent measurements of the ^{36}Ar + ^{197}Au system have found $\langle N_{IMF} \rangle = 4$ in central collisions [deSo 91]. However, at 115 AMeV, the standard deviation of the IMF probability distribution for central events is quite large ($\sigma_{IMF} = 1.3$), as can be seen in Figure 3.8. A significant fraction (~40%) of the central events contains three or more IMFs.

As mentioned in the previous section, there are multiple sources for IMF and LCP emission, including preequilibrium emission and statistical emission from an fusion-like source. Work by Fatyga et al. [Faty 87a, Faty 87b], has shown that particles from these sources can be separated through the selection of emission angle. Based fits to energy spectra, Fatyga states that IMFs emitted at backward angles seem to come from the fusion-like source, whereas particles emitted at more forward angles are most likely from preequilibrium processes. We have made no such distinction in the above results, and therefore claim only to be accessing overall deposition energy thus far, rather than thermal excitation energy.

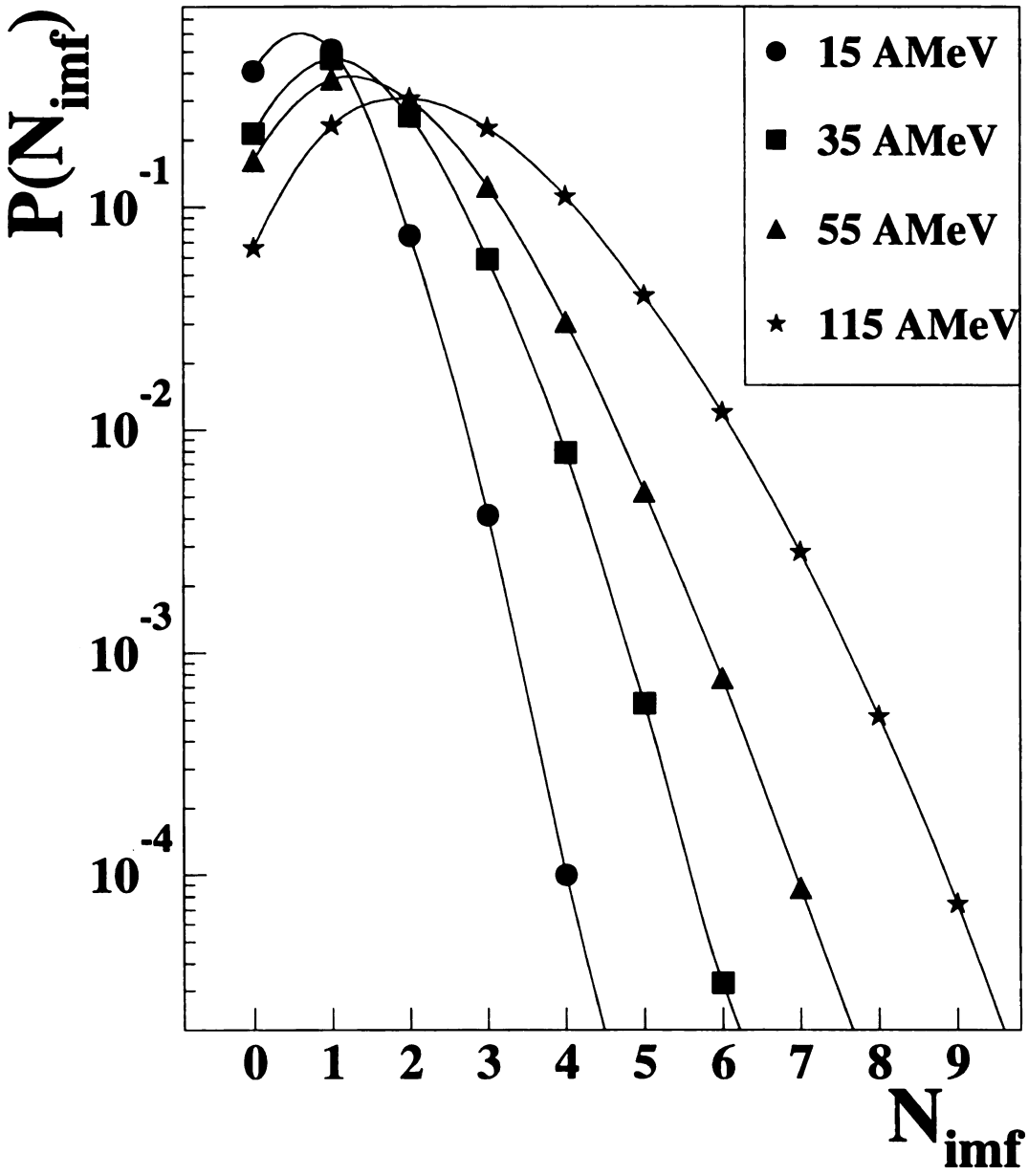

Figure 3.8: IMF probability distributions for central events (selected with E_T) from the BALL 2 trigger data. Data is presented for four beam energies as defined in the key. These values are not corrected for detector acceptance.

3.5 Calculations of Momentum Transfer and Excitation Energy

In the previous sections, we have presented measurements of observables which are related to the momentum transfer and energy deposition in the $^{40}Ar + ^{232}Th$ system. In the next sections, we will quantitatively determine these properties, and study their evolution with bombarding energy.

3.5.1 Linear Momentum Transfer

The momentum transferred to the fissioning nucleus can be calculated if one measures the mass and velocity of the fission fragments. While these observables were not directly available for the present analysis, a calculation of the average linear momentum transfer, relative to the beam momentum $\frac{\langle p \rangle}{p_{beam}}$ can still be performed as shown in Reference [Leeg 92],

$$\frac{\langle p \rangle}{p_{beam}} = \left(\frac{M \langle E_k \rangle}{M_p E_p} \right)^{1/2} \frac{sin\Theta_{ff}}{[2sin^2(\Theta_1) + 2sin^2(\Theta_2) - sin^2(\Theta_{ff})]^{1/2}}, \tag{3.3}$$

where M_p and E_p are the mass and kinetic energy of the projectile, and M is the mass of the the fissioning nucleus. For $\langle E_k \rangle$, the updated formula from Viola was used [Viol 85]:

$$\langle E_k \rangle = (.1189 \frac{Z^2}{A^{1/3}} + 7.3)\, MeV. \tag{3.4}$$

The angles Θ_1 and Θ_2 are the angles of the fission fragments with respect to the trajectory of the fissioning nucleus. It is assumed this trajectory is the same as the beam direction, so the lab angles of the fission fragments are used for Θ_1 and Θ_2. The mass M is extrapolated from values measured by Conjeaud et al. [Conj 85] at energies near the middle of the present range studied. Using equation 3.10, the linear momentum transfer is calculated event by event, and an average is found.

In Figure 3.9, the fractional linear momentum transfer $\frac{p_{||}}{p_{beam}}$ is plotted versus the velocity parameter $[(E_{beam} - E_c)/A]^{1/2}$. E_c is the Coulomb barrier which is ~200 MeV for this system. The solid line represents a systematic dependence of the momentum transfer on the beam momentum which has been determined empirically from data collected by several investigators [Viol 82]. The parameterization used here is from the work of Nifenecker et al. [Nife 85]. The solid circles represent the most probable linear momentum transfer, $p_{||}^{mp}$, determined by fitting a gaussian to the momentum transfer distribution from the high LMT events in the most central collisions, i.e., the events shown in Figure 3.4. In previous experiments with this system, this variable could not be extracted at energies above 40 AMeV, because the high LMT peak could not be resolved in the inclusive folding angle distribution [Schw 94]. The values we extract agree quite well with the systematic curve even at the highest beam energies where there had been no data previously for this system.

The open squares represent the mean linear momentum transfer, $\langle p_{||} \rangle$, from the impact parameter inclusive data in Figure 3.3. These values are always below the data from the central collisions because of the contribution to the fission cross section from peripheral collisions. The relative size of this contribution increases with beam energy, and so the discrepancy between the two data sets increases as well.

Figure 3.10 shows the evolution of the linear momentum transfer *per projectile nucleon* $\frac{p}{A_{beam}}$ as a function of the velocity parameter $[(E_{beam} - E_c)/A]^{1/2}$. The solid line indicates the beam momentum or full momentum transfer, and the symbol definitions are the same as in Figure 3.9. The momentum transfer per projectile nucleon is always less than full beam momentum in this energy range, even for the central collisions. This indicates, as stated in section 3.2, that primarily incomplete mass transfer is occurring. The impact parameter inclusive measurement of average momentum transfer is maximum at 25 AMeV, and then decreases with beam momentum.

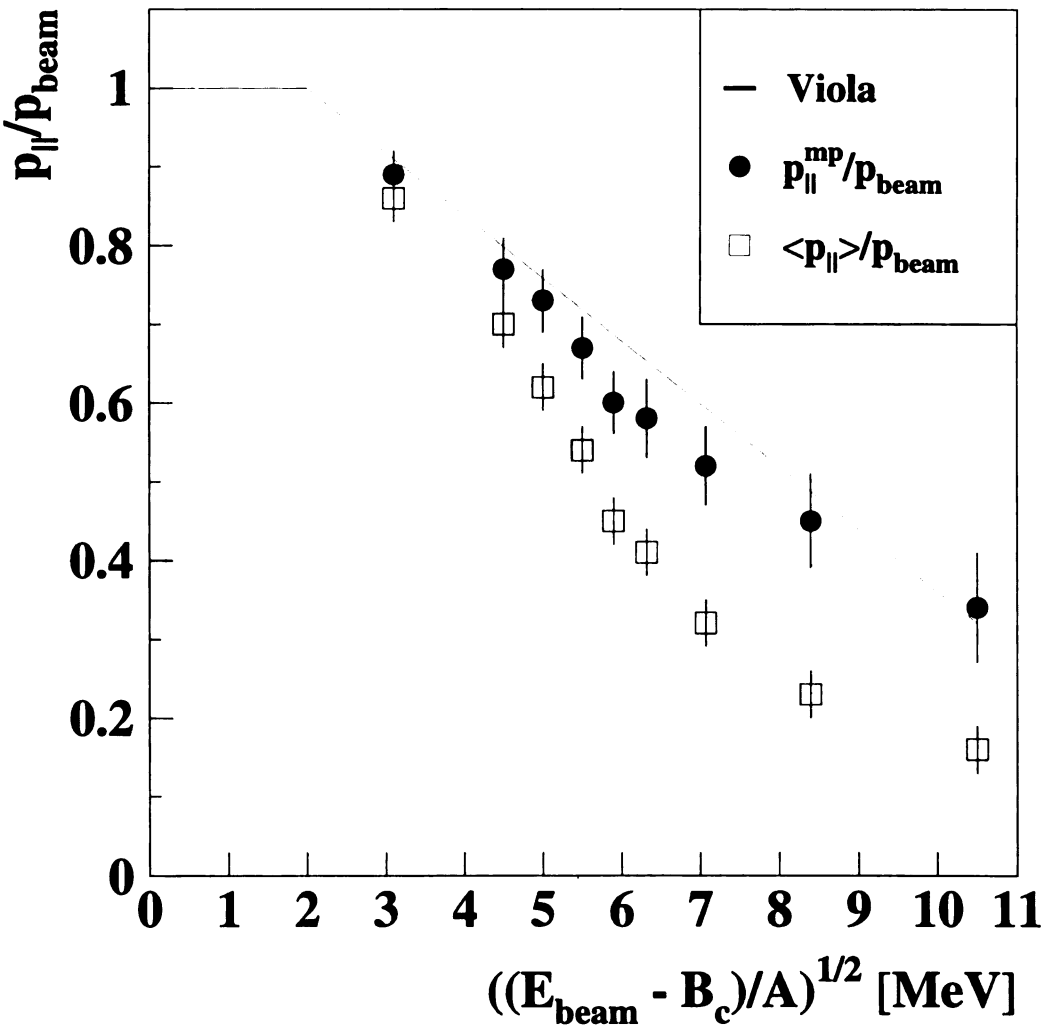

Figure 3.9: Fractional parallel linear momentum transfer plotted versus the velocity parameter, $((E_{beam} - E_c)/A)^{1/2}$ for the Ar +Th system. Symbols are defined in the inset.

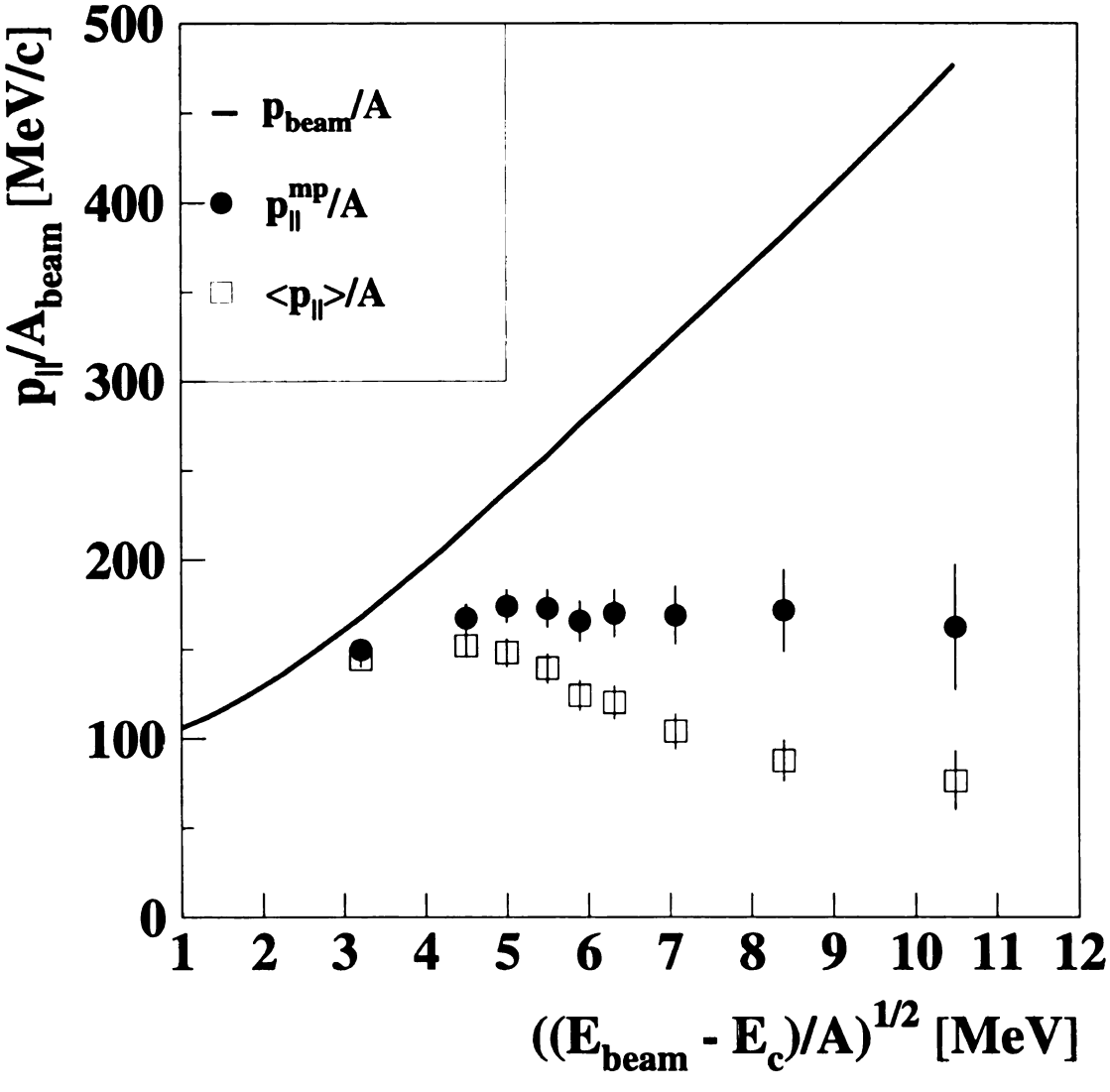

Figure 3.10: Parallel linear momentum transfer per projectile nucleon plotted versus the velocity parameter, $((E_{beam} - E_c)/A)^{1/2}$ for the Ar +Th system.

Both the location of this maximum and the rate of decline of $\frac{\langle p \rangle}{A_{beam}}$ beyond that point are in agreement with data from similar systems [Viol 89, Faty 85].

The momentum transfer for the isolated high LMT events does not decline with beam energy. The solid points show that it increases with beam energy from 15 AMeV to 25 AMeV and then saturates at approximately 170 MeV/c per projectile nucleon.

3.5.2 Excitation Energy

As one might expect, linear momentum transfer is closely linked to deposited excitation energy [Jacq 85, Bege 92, Blai 92]. Intranuclear cascade calculations from the 1960s provided an empirical relationship between these two quantities [Pori 60]. In order to quantitatively determine the energy deposited in the ^{40}Ar + ^{232}Th system we performed a calculation of the average total excitation energy, $\langle E^* \rangle$, using a method similar to that described in Reference [Bege 92], and based on new calculations presented in Reference [Blai 92]. In [Bege 92], excitation energy as calculated through

$$E^* = E^*_{CF} \frac{p_{||}}{p_{beam}} \frac{A_P + A_T}{A_{sys}} \tag{3.5}$$

was shown to reasonably describe the mass loss of the fissioning nucleus. E^*_{CF} represents the excitation energy for complete fusion, A_P and A_T are the atomic mass of the projectile and target, respectively, and A_{sys} is the atomic mass of the fissioning system. The quantity E^* is calculated from the most probable LMT measured in the most central fission-like reactions (the solid circles in Figure 3.9) using the method described in the previous section. The average excitation energies, $\langle E^* \rangle$, extracted in this way are summarized in Table 3.1. The values we obtained for the energies studied in Reference [Conj 85] agree well with the values cited in that work. Uncertainties were calculated from the width of the momentum transfer distributions coupled with

Table 3.1: Summary of momentum transfer and excitation energy for the Ar +Th system.

E_{beam} (AMeV)	$\langle p_{\|} \rangle / p_{beam}$ (%)	$p_{\|}^{mp} / p_{beam}$ (%)	$p_{\|}^{mp} / A_{beam}$ (MeV/c)	E^* (MeV)	ϵ^* (AMeV)	M_{res} (AMU)
15	86±3	89±3	150±5	474±4	1.78±0.03	266±6
25	70±3	77±4	167±8	710±9	2.70±0.06	263±9
30	62±3	73±4	174±9	788±11	3.02±0.08	261±10
35	54±3	67±4	173±11	860±13	3.32±0.10	259±12
40	45±3	60±4	166±12	884±15	3.44±0.12	257±13
45	41±3	58±5	170±13	998±20	3.90±0.15	256±15
55	32±3	52±5	169±16	1067±26	4.27±0.21	250±18
75	23±3	45±6	172±23	1300±44	5.42±0.37	240±24
115	16±3	34±7	162±35	1693±92	7.46±0.81	227±37

the experimental uncertainty in the mass of the fissioning system.

Figure 3.11 shows the calculated values of the average excitation energy *per nucleon*, $\langle \epsilon^* \rangle$, versus beam energy (solid circles). The value of $\langle \epsilon^* \rangle$ increases with beam energy up to ~7.5 AMeV, indicating, as did Figure 3.7, that there is no saturation in excitation energy in this system. We also extracted excitation energies from a two-stage model [Harp 71, Desb 87, Cerr 89] which was shown in [Yee 95b] to reasonably predict the decline of the fusion cross section in the present system. The first stage of this model is hydrodynamical in nature, and begins with the nucleons of the projectile trapped within the potential well of the target. This system then equilibrates through two-body collisions and the emission of light particles. At the end of this stage the excitation energy is extracted and used as input for the second stage. In that stage, the system expands isentropically and cools. It is then determined whether the system undergoes sequential binary decay or multifragmentation. This determination is based on fluctuations in the mean field as calculated through a percolation calculation. As shown in Figure 3.11, the values of $\langle \epsilon^* \rangle$ extracted from the first stage of the model agree quite well with the calculation based on momentum

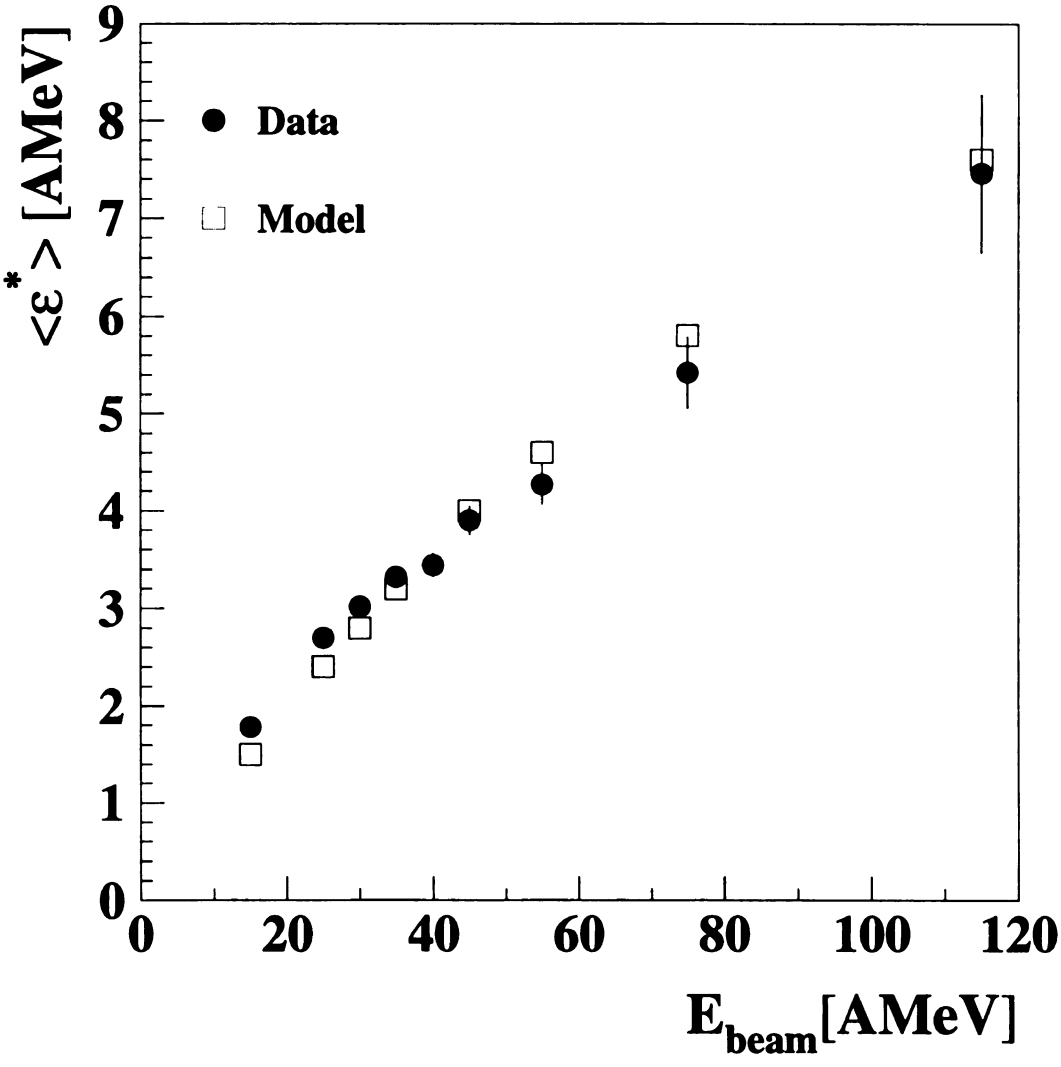

Figure 3.11: Average excitation energy per nucleon deposited in the the Ar + Th system plotted versus beam energy.

transfer.

3.6 Summary and Discussion

In this chapter we have studied the evolution of fission fragment angular distributions, momentum transfer and excitation energy in ^{40}Ar + ^{232}Th collisions, as bombarding energy is increased from 15 to 115 AMeV. Fission fragment folding angle distributions support previous measurements that indicate the process of fusion-fission declines with bombarding energy. However, through the use of impact parameter filters, we have determined that a high LMT, fission-like process still occurs even at 115 AMeV. Fission fragment azimuthal distributions indicate that the nature of the fission at these energies has changed from an essentially binary to a many-fragment process.

Momentum transfer per projectile nucleon in high LMT, fission-like events has been found to saturate at 170 MeV/c for beam energies above 30 AMeV. Fractional momentum transfer for these events has been found to agree quite well with an empirically determined functional form for all beam energies studied, including the highest energies for which this variable has not been measured before in this system. The saturation of momentum transfer as it approaches the value of the Fermi momentum (~250 MeV/c [Moni 71]) has been interpreted as indicating the increased effect of nucleon-nucleon interactions over the influence of the dinuclear mean-field [Jacq 84, Faty 85, Viol 89].

Energy deposited in this system in central collisions has been shown to increase steadily with beam energy through the measurement of IMF and LCP multiplicities as well as through a calculation involving the measured momentum transfer. These observations about momentum transfer and deposited energy lead one to ask if the dominant reaction mechanism is changing as beam energy increases. In the Ar +

Au system, for example, evidence has been presented there is a possible transition to multifragmentation at excitation energies of 5 AMeV, a value we reach in this system at bombarding energies near 55 - 75 AMeV [Biza 93]. In the next chapter we present evidence for a similar transition in this system.

Chapter 4

Event Shape Analysis

4.1 Introduction

This chapter will discuss changes in the reaction mechanism in $^{40}Ar + ^{232}Th$ collisions as function of beam energy, as viewed through the technique of event shape analysis [Cugn 82, Gyul 82, Cebr 90a, Cebr 91]. Topics that will be dealt with include multiplicity distortions inherent in this method, the effects of detector acceptance, and the separation of projectile-like sources from center-of-mass sources.

4.2 The Flow Tensor

The event shape analysis begins with the event by event construction of the flow tensor [Cugn 82, Gyul 82]. Each event is transformed into the center-of-mass reference frame, and the flow tensor is then constructed by summing over the momentum components of each fragment in the event as follows:

$$\mathbf{F} = \sum_{i,j} F_{ij} \tag{4.1}$$

where

$$F_{ij} = \sum_{n=1}^{N_c} \omega_n p_n^i p_n^j. \tag{4.2}$$

The sum runs over the total event multiplicity N_c, and the variables i and j represent the cartesian coordinates x, y, and z. Thus, the quantity p_n^i is the i*th* momentum component of the n*th* particle in the event. The quantity ω_n is the weighting factor for each particle and is needed to make the tensor coalescence invariant. That is, since the sum runs over particles of various masses, a factor must be included to ensure that heavy fragments do not dominate the flow tensor. This factor is often chosen to be $\frac{1}{2m_n}$, making $\mathbf{F}$ the kinetic energy tensor, however $\frac{1}{p_n^2}$ is also a valid choice. The end result is an ellipsoid that describes either the energy or particle flow of the event.

Once the tensor is constructed, an orthogonal similarity transformation is performed to reduce it to diagonal form. This corresponds to rotating the coordinate axes so that they coincide with the principal axes of the three-dimensional momentum spheroid. The ellipsoid can be completely described by three eigenvalues (f_i) and three eigenvectors ($\mathbf{e}_i$):

$$\mathbf{F} = f_1\mathbf{e_1}\mathbf{e_1}^\dagger + f_2\mathbf{e_2}\mathbf{e_2}^\dagger + f_3\mathbf{e_3}\mathbf{e_3}^\dagger, \tag{4.3}$$

where the eigenvectors give the direction of the principal axes, and the square root of the eigenvalues ($\sqrt{f_i}$) give the length of those axes. Figure 4.1 depicts such an ellipsoid. It is extremely important that the tensor be constructed in the frame of the emitting source. If the frame of calculation moves quickly with respect to the emitting frame, all of the momentum vectors will appear elongated due to the relative motion of the source and the ellipsoid will thus be artificially elongated as well.

The eigenvalues of the tensor satisfy the cubic equation

$$f_i^3 + a_2 f_i^2 + a_1 f_i + a_0 = 0, \tag{4.4}$$

with

$$a_2 = -(F_{11} + F_{22} + F_{33}), \tag{4.5}$$

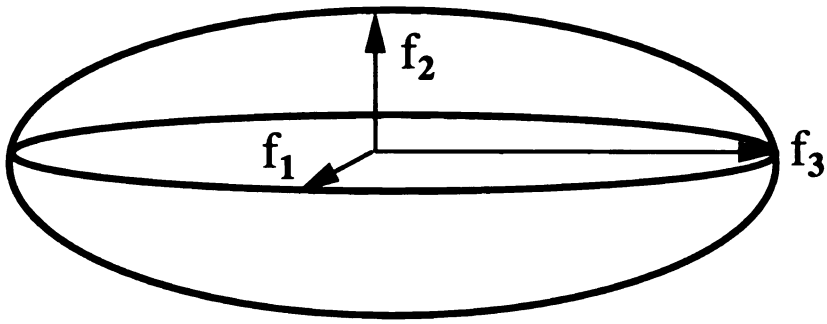

Figure 4.1: Schematic depiction of the flow ellipsoid. The principal axes are denoted as f_1,f_2, and f_3

$$a_1 = F_{11}F_{22} + F_{11}F_{33} + F_{22}F_{33} - F_{12}^2 - F_{13}^2 - F_{23}^2, \tag{4.6}$$

and

$$a_0 = F_{11}F_{23}^2 + F_{22}F_{13}^2 + F_{33}F_{12}^2 - F_{11}F_{22}F_{33} - 2F_{12}F_{13}F_{23}. \tag{4.7}$$

The three solutions to this equation can be written as follows (for i=1,2,3):

$$f_i = -\frac{1}{3}a_2 + 2p\,cos[\frac{1}{3}cos^{-1}(r/p^3) + (n-1)\frac{2}{3}\pi], \tag{4.8}$$

where

$$p = \frac{1}{3}(a_2^2 - 3a_1)^{\frac{1}{2}} \tag{4.9}$$

and

$$r = \frac{1}{6}(a_1a_2 - 3a_0) - \frac{1}{27}a_2^3. \tag{4.10}$$

The orientation of the eigenvectors can be determined in spherical coordinates with **the** following equations (for i=1,2,3):

$$\theta_i = cos^{-1}[1/\sqrt{1 + c_i^2 + (f_i - F_{33} - F_{23}c_i)^2/F_{13}^2}], \tag{4.11}$$

$$\phi_i = tan^{-1}[c_iF_{13}/(f_i - F_{33} - F_{23}c_i)], \tag{4.12}$$

where

$$c_i = \frac{(F_{11} - f_i)(F_{33} - f_i) - F_{13}^2}{F_{12}F_{13} - F_{23}(F_{11} - f_i)}. \tag{4.13}$$

The quantities θ_i and ϕ_i are the polar and azimuthal angles of the corresponding **eigen**vectors $\mathbf{e_i}$.

4.2.1 Sphericity and Coplanarity

We now have the means to describe the shape of the ellipsoid in terms of its eigenvalues and eigenvectors. An ellipsoid having $f_1 > f_2 = f_3$ is elongated on one axis, and has a rod-like shape, whereas an ellipsoid with $f_1 < f_2 = f_3$ is shortened on one axis and would appear flattened. A perfectly spherical event shape would have $f_1 = f_2 = f_3$. It is useful to further reduce the quantities describing the ellipsoid in order to more succinctly describe the event shape. We first order the eigenvalues by magnitude, defining $f_3 > f_2 > f_1$. The eigenvalues are then squared and normalized in the convention used by Fai and Randrup [Fai 83]:

$$q_i = \frac{f_i^2}{\sum_{j=1}^{3} f_j^2}. \tag{4.14}$$

Now, the ellipsoid axes, q_i, are normalized such that $q_1 + q_2 + q_3 = 1$. This is desirable since, in determining the event shape, we are interested in the relative sizes of the axes and not the overall volume of the ellipsoid. We can now use these reduced quantities to define the two parameters: sphericity, $S = \frac{3}{2}(1 - q_3)$, and coplanarity, $C = \frac{\sqrt{3}}{2}(q_2 - q_1)$ [Fai 83]. Alternate definitions of S and C also exist in which the eigenvalues are not squared [Cugn 83]. With the present definitions, S can take on any value between 0 and 1, while C ranges from 0 to $\sqrt{3}/4$. Figure 4.2 shows the triangular region which contains the allowed values in the S-C plane, and connects the possible shapes of the ellipsoid with their corresponding area in that plane. As can be seen in Figure 4.2, a perfectly spherical distribution would have S=1 and C=0, a disc-like distribution would have a large value of C and a reduced value of S from the spherical case, and a rod-like distribution would have small values of both variables.

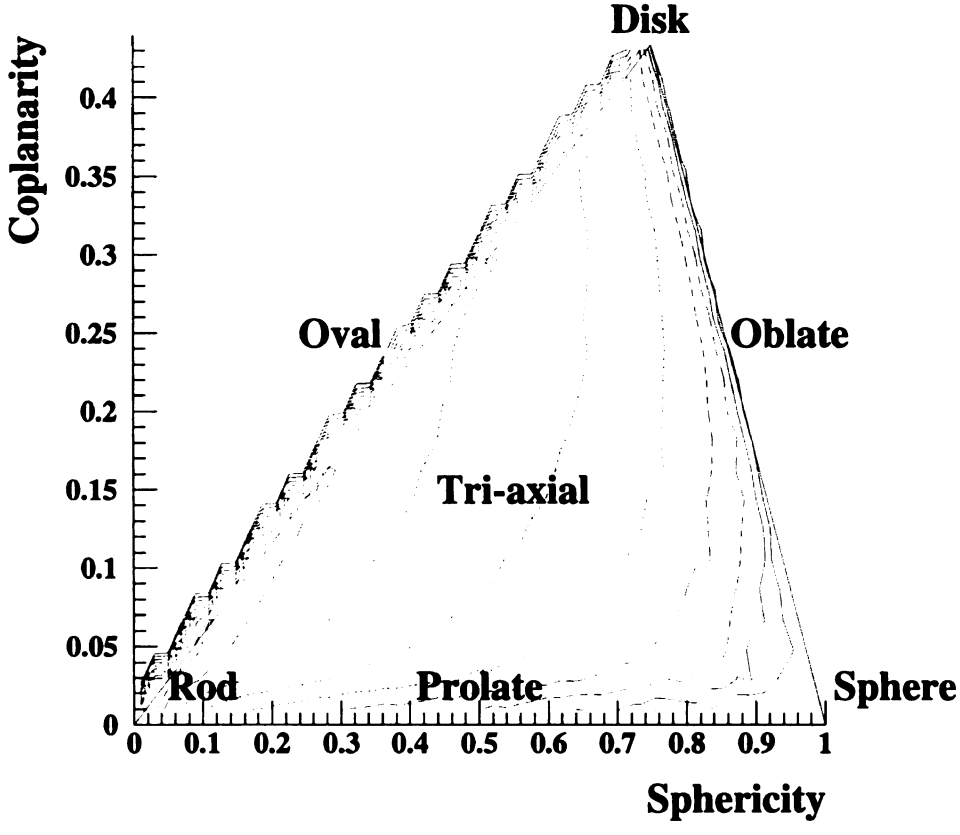

Figure 4.2: Diagram defining the allowed region of S-C space. Shapes along the **line** connecting (0,0) and (0.75,0.43) are 2-dimensional and range from a perfect rod ($f_2 = f_3 = 0$) to a perfect circle ($f_3 = f_2 = \frac{1}{2}, f_1 = 0$). Shapes along the bottom axis **range** from a perfect rod to a sphere ($f_1 = f_2 = f_3 = \frac{1}{3}$) with f_2 and f_3 increasing **with** sphericity. Shapes on the line from (0.75,0.43) to (0,1) range from a perfect **circle** to a sphere, with f_1 increasing as coplanarity decreases.

4.3 Relationship of the Event Shape to the Reaction Mechanism

In section 4.2 the basis of the technique of event shape analysis was described. In this section, we will relate the usefulness of this technique to the study of the evolution of the reaction mechanism in $^{40}Ar + ^{232}Th$ collisions.

López and Randrup have proposed that the shape of the flow tensor should be sensitive to the timescale of the breakup process [Lope 89]. At beam energies well below the Fermi energy, the sequential decay of particles is known be the dominant breakup process [Gelb 87]. This type of time-ordered process should lead to elongated event shapes due to the kinematical constraints of the fragment emission. That is, the compound nucleus emits a particle and recoils, that particle then emits another and so on. The trajectories of the subsequently emitted particles are influenced strongly by the initial axis of emission.

At beam energies above the Fermi energy, multifragmentation processes are believed to become dominant [Fai 83, Bond 90, Bowm 91, Ogil 91]. These processes occur on a much faster time scale than sequential processes and are characterized by the nearly simultaneous breakup of the colliding system into many intermediate size particles. In this scenario, the emission of the fragments may be isotropic as there are no longer one or two large fragments to define an axis [Cebr 90a, Ogil 91].

As discussed in the previous chapter, in the $^{40}Ar + ^{232}Th$ system at beam energies below ~40 AMeV, it is known that the fusion-fission process dominates the cross section [Viol 89, Viol 82, Conj 85]. In the frame of the fissioning nucleus, the two fission fragments are emitted roughly back-to-back as required by momentum conservation, and their trajectories define the fission axis. While particles may be emitted isotropically from the daughter fragments, their momenta in the frame of the compound

nucleus will be folded toward the fission axis. A study by Yee et al., has shown that the emission angles of particles with charge Z=2 and higher are highly correlated with the trajectory of either of the fission fragments in this system at energies below 40 AMeV [Yee 95b].

The fission plane is formed by the fission axis and the beam axis. Work by Tsang et al. has shown that light and intermediate mass charged particles are emitted preferentially in the fission plane for systems similar to the present one. This anisotropy was shown to increase with the mass and kinetic energy of the emitted particles [Tsan 84, Tsan 90, Tsan 91]. These types of focussing effects will suppress sphericity since the ellipsoid described by the flow tensor will be flattened towards the fission plane and elongated along the fission axis.

At the highest energies studied here (>50 AMeV), it has been suggested that multifragmentation takes over as the dominant reaction mechanism [Conj 85, Viol 89, Schw 94]. In this case, the emission may be isotropic, and sphericity should be close to the maximum value allowed. Work by Wilson et al. [Wils 91] has shown that for symmetric systems, the aforementioned anisotropy all but disappears for beam energies near 100 AMeV, providing a clue that the reaction mechanism is undergoing a transition. In asymmetric systems, polar angle distributions of complex fragments indicate increasingly isotropic emission as excitation energy increases [Yenn 90]. Like the decline of this anisotropy, an increase in sphericity may also be interpreted as a signal that there has been a change in the dominant reaction mechanism from fusion-fission to multifragmentation. However, there are some issues that must be discussed before this connection can be made.

4.4 Effects Which May Distort the Event Shape

There are other factors which may affect the event shape other than the time-scale of the break-up. These factors include, finite multiplicity distortions, detector acceptance, and multiple sources within the event set; these issues will be dealt with in the present section.

4.4.1 Model

In order to more easily understand many of the effects discussed in this section, it is useful to model them using a Monte Carlo simulation. The model used is based on one described by Bondorf and Dasso *et al.* [Bond 90a]. In this simulation, particles are generated having center-of-mass momentum components (p_x,p_y,p_z) chosen from gaussian distributions as would be given from simple thermodynamic equilibrium:

$$P(p_i) = e^{\frac{-p_i^2}{2M\tau\sigma_i^2}}. \tag{4.15}$$

Here M is the mass of the particle and τ is the temperature of the system. The standard deviation σ_i of the gaussian associated with a particular axis can be adjusted to be some fraction or multiple of the standard deviations associated with the other axes. Thus, a prolate distribution can be created by setting $\sigma_z > \sigma_y = \sigma_x$, an oblate distribution can be created if $\sigma_z < \sigma_y = \sigma_x$, and a spherical distribution results if $\sigma_z = \sigma_y = \sigma_x$. Since the factor τ is common to all the momentum components, changing τ does not change the relative sizes of the ellipsoid axes, only the overall size of the ellipsoid. The charge distribution was chosen to be an exponential following,

$$P(Z) = e^{-Z/\lambda}, \tag{4.16}$$

where λ was adjusted between the values 1.0 and 2.0.

A set of 50,000 events with multiplicity N_c=10, and temperature $\tau = 6$ MeV was generated from a prolate momentum distribution with $2\sigma_x = 2\sigma_y = \sigma_z = 2$, and a summary of this event set is shown in Figure 4.3. The frame of the emitting source was at rest in the lab. The frames in Figure 4.3 contain plots of key aspects of the simulated events as described in the figure caption. Shown explicitly in this figure is the effect of making σ_z largest of the three standard deviations, since the projection of the momentum distribution along the z-axis (P_z) is much wider that along the y-axis (P_y).

In the bottom right frame of Figure 4.3, the mean value of sphericity, $\langle S \rangle$, for the event set is plotted versus the velocity of the frame in which the momentum tensor was constructed. This demonstrates the effect of constructing the momentum tensor in a frame other than the emitting frame. The frame is boosted along the z-axis and this induces an apparent elongation of the momentum ellipsoid in the boost direction. Thus, the value of $\langle S \rangle$ diminishes as we leave $\beta_{frame} = 0$. The sphericity probability distributions for the correct frame are shown in the bottom left frame of Figure 4.3.

These two frames demonstrate another important aspect of the the sphericity measurement. This aspect is the difference in $\langle S \rangle$ when the $\frac{1}{p^2}$ normalization is used for the flow tensor elements as opposed to the $\frac{1}{2m}$ normalization. In the former case, all of the momentum vectors are made into unit vectors, thus, $\langle S \rangle$ must necessarily be larger than in the latter case because all of the vectors now lie with their ends on a sphere. Only the directions of the particle momenta matter with this normalization; variations in particle energy have no effect on the sphericity. The usefulness of this feature will be made apparent in section 4.4.3.

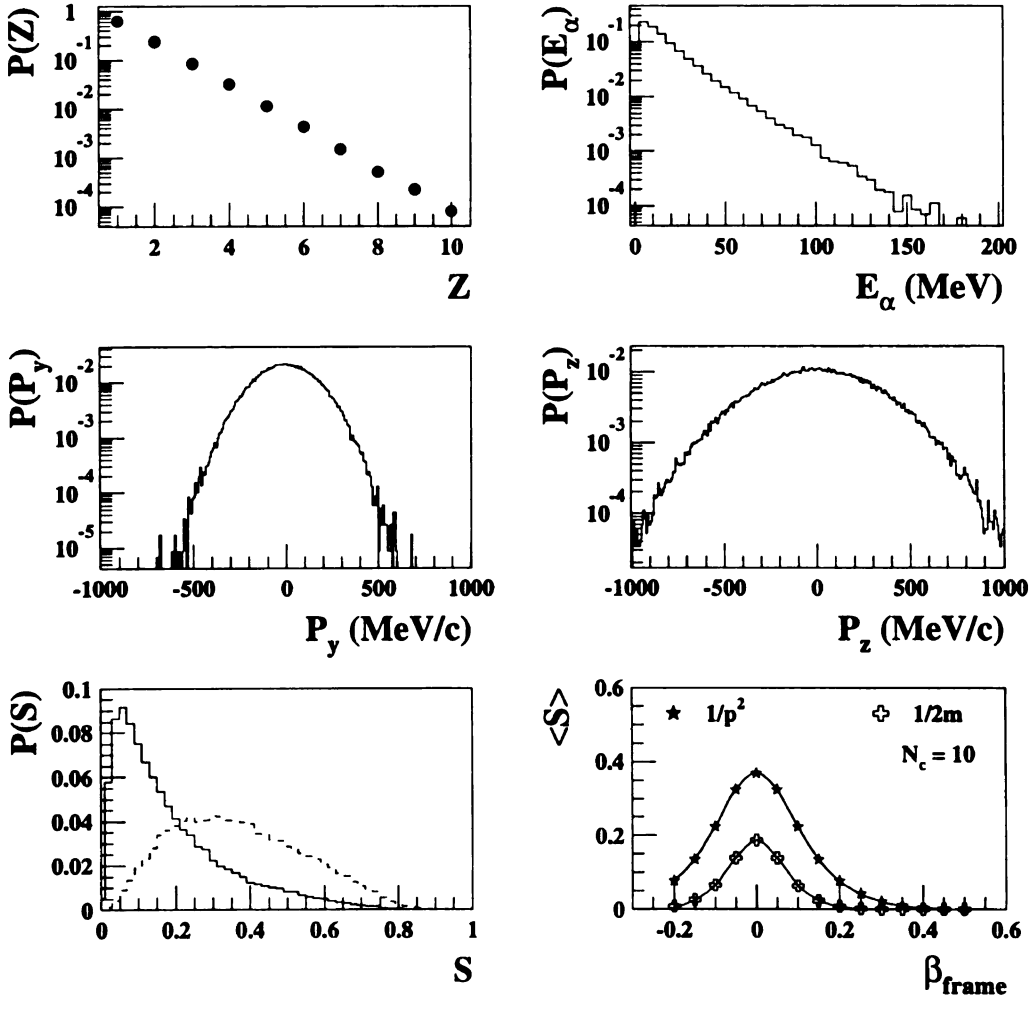

Figure 4.3: Set of 50,000 events with multiplicity $N_c = 10$ and $\tau = 6$ MeV. $2\sigma_x = 2\sigma_y = \sigma_z = 2$. The source of the emitting frame was at rest in the lab. The frames contain "snapshots" of key aspects of the simulated events as follows: Z probability distribution (top left), energy probability distribution for alpha particles (top right), y-axis component of the momentum distribution (middle left), z-axis component of the momentum distribution (middle right), sphericity distributions as calculated in the rest frame with $\frac{1}{2m}$ (solid) and $\frac{1}{p^2}$ (dashed) normalizations (bottom left), and the average sphericity for the event set as calculated for several different boost frames with both normalizations. The boost direction is along the z-axis.

4.4.2 Multiplicity Distortions

It is well known that there are finite multiplicity distortions that affect the measured values of sphericity [Dani 83, Bond 90a]. For events with a finite number of particles, measurements of sphericity will fluctuate about an average value which is shifted from the theoretical value by a factor of order $1/\sqrt{N_c}$. For events with multiplicities of $N_c > 200$, this effect is small, however, for particle multiplicities on the order of those in the present study, it is extremely important. In our case, this means that completely isotropic event may yield a value of sphericity significantly less than 1.0. The average value of sphericity for a set of such events may be equivalent to the value of sphericity corresponding to a prolate event with an infinite number of particles As multiplicity increases, and the distortion becomes less important, the measured value of $\langle S \rangle$ for these isotropic events begins to increase towards its theoretical (infinite particle) value. This means that a simple increase in multiplicity will have the same effect on sphericity as a change to a more spherical emission pattern of the particles. This could be falsely interpreted as indicating a change in the particle flow and reaction dynamics.

This effect has been simulated in Figure 4.4 using the above mentioned Monte Carlo model. Events were generated with a prolate (rod-like), oblate (disc-like), or spherical distribution for event multiplicities $N_c = 2 - 20$. The input parameters σ_x, σ_y, and σ_z are chosen as in Bondorf et al. [Bond 90a]. In Figure 4.4a, as N_c increases, so does $\langle S \rangle$ for the disk-like and spherical distributions. The rod-like distribution increases and then flattens. Even for events with $N_c = 20$, the value of $\langle S \rangle$ for the spherical events is much less 1.0.

For multiplicities below $N_c = 5$, values of $\langle S \rangle$ for the three shapes are very close to one another, however, as Figure 4.4b shows, there are measurable differences in $\langle S \rangle$

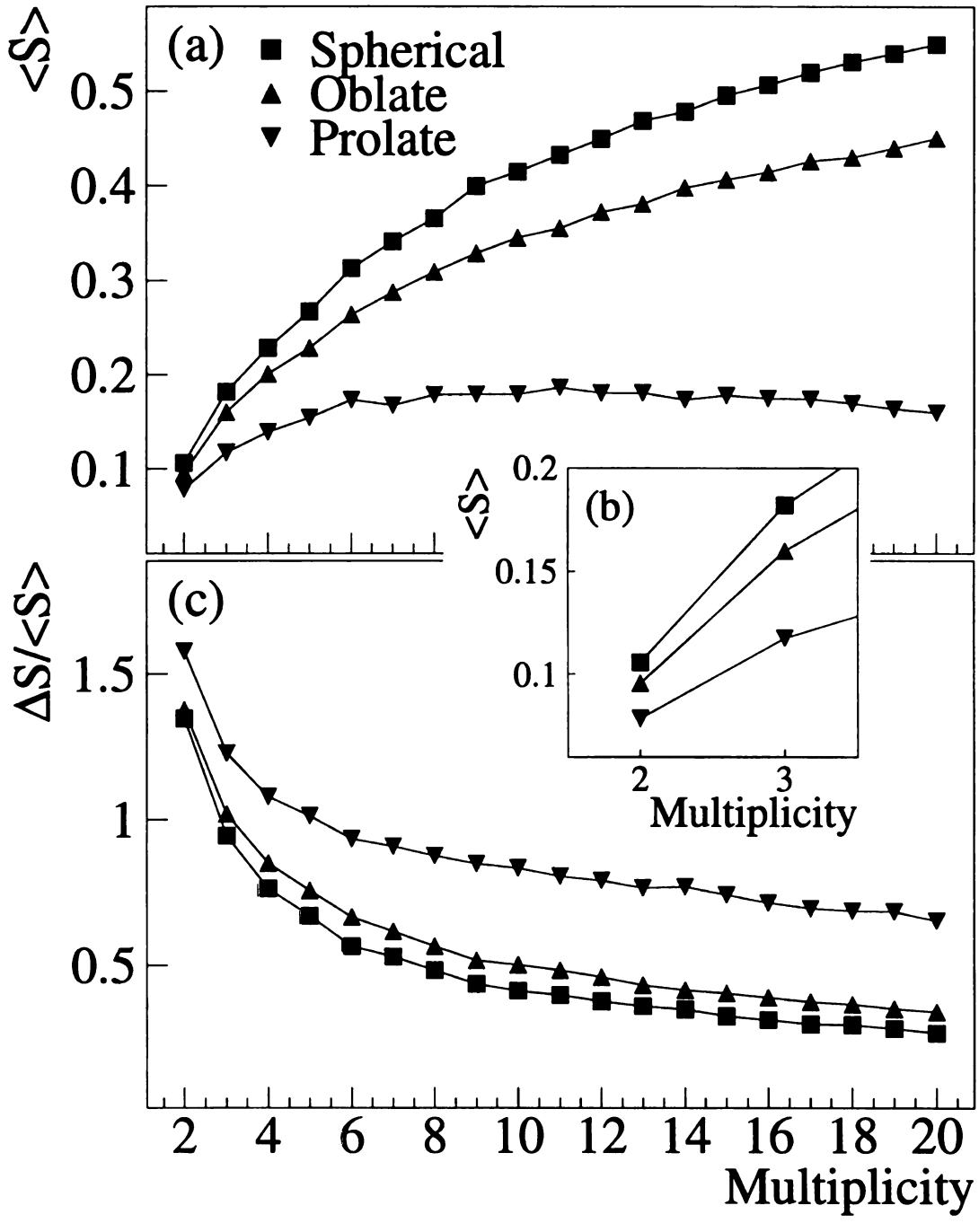

Figure 4.4: Simulated events with spherical, oblate, and prolate particle flows and multiplicities varying from 2 - 20. 50,000 events were generated for each multiplicity and shape. Prolate events have $2\sigma_x = 2\sigma_y = \sigma_z = 2$. Oblate events have $\sigma_x = \sigma_y = 2\sigma_z = 1$. Spherical events have $\sigma_x = \sigma_y = \sigma_z = 1$.

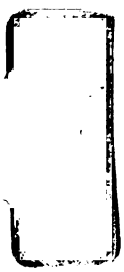

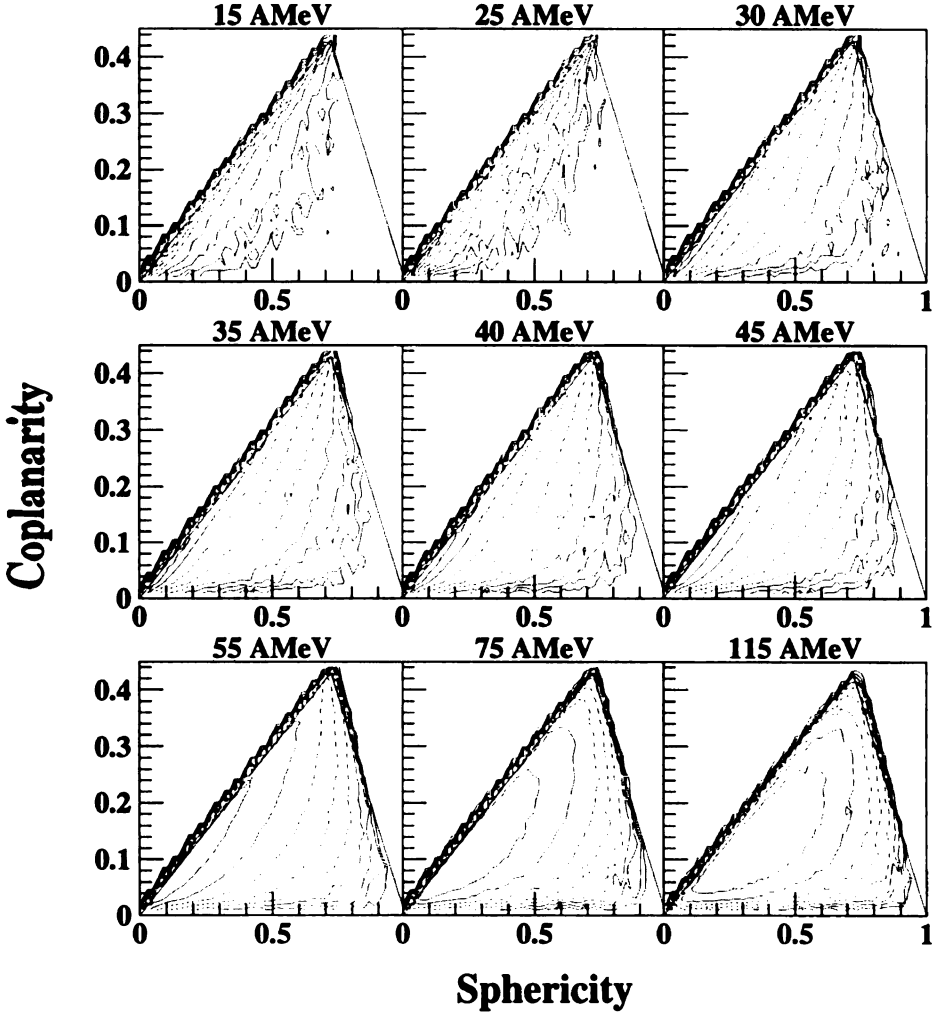

Figure 4.5: Contour plot of the area of S-C space taken up by central events for all **nine** energies studied. The migration of the contour toward the lower right corner is **due** in large part to the increase in average multiplicity as beam energy increases.

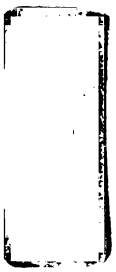

even for $N_c = 2$. Figure 4.4c shows the reduced widths of the sphericity distributions $\Delta S/\langle S\rangle$. The widths decrease steadily with multiplicity as they are also caused by finite number fluctuations, and would vanish for an infinite number of particles.

The effect of multiplicity distortions can also be seen in the present data as shown in Figure 4.5. This figure depicts the S-C distributions for central collisions at the nine beam energies studied. There is no explicit selection on specific multiplicities, and the shift of the contour toward the lower right corner is due in great part to the increase in average multiplicity with beam energy. This problem of multiplicity distortions will be dealt with in the present analysis by explicitly separating events based on their multiplicity and comparing changes in sphericity only for events that have the same multiplicity.

4.4.3 Multiple Emitting Sources

It has already been stated that in order for the sphericity analysis to be meaningful, the flow tensor must be constructed in the correct frame, i.e., the frame in which the particles are being emitted. This naturally brings up the question of what happens when there is more than one emitting source in an event or when events in which the source velocity is different are included in the average over sphericity. We will begin to deal with these issues using our Monte Carlo model. Figure 4.6 shows the event summary for 50,000 events generated with two spherically emitting sources. One source is at rest and the other source is moving with a velocity of $\beta = 0.2$c along the z-axis. Each event contains 20 particles, 10 from each source, and both sources were given a temperature $\tau = 6$ MeV for the sake of symmetry. The double humped energy distribution and P_z distribution are the trivial result of this two-source event set. The interesting result is in the plot of $\langle S\rangle$ versus β_{frame}.

For the $\frac{1}{2m}$ normalization, $\langle S\rangle$ peaks at a frame velocity halfway between the

frames of the two sources. Also, the maximum value of $\langle S \rangle$ attained is less than the case of one spherical source with 20 or even 10 particles (see Figure 4.4). Looking from the frame of the source at rest, the momenta originating from the moving source are elongated along the z-axis, and this reduces the rest source's sphericity in its own frame. The inverse of this is true looking from the moving frame as well. Since the two sources are symmetric, a maximum is reached halfway between the two frames where the combined elongation effect is minimized for both sources.

For the $\frac{1}{p^2}$ normalization, the effect is quite different. Since only the emission angles of the particles are important and not the magnitudes of the momenta, the sources do not interfere with each other nearly as much as with the other normalization, and there are two distinct peaks located at the correct frame velocities. The two sources do still affect one another however, as the maximum value of $\langle S \rangle$ is still less than if there were only one spherical source emitting 10 particles.

A simulation was also run in which the two spherical sources are isolated in separate events. Half of the events contain the source at rest, and half contain the moving source. Figure 4.7 shows the summary for this set of events. In this case either normalization provides two distinct peaks at the correct frame velocities in the $\langle S \rangle$ versus β_{frame} plot. The sphericity probability distributions in the lower left frame also show two peaks coming from the two distinct groups of events. While the maximum values of $\langle S \rangle$ are still lower than the case of one spherically emitting source of 20 particles, the averaging over two sources in different events does not have as large an effect on $\langle S \rangle$ as does averaging over two sources in the same event.

In the present data, we are interested in studying the evolution of central collisions in which the emitting source is presumed to be moving at close to the center-of-mass velocity. Clearly, if there is a contribution from particles emitted from a faster frame, as in either of the previous scenarios, this will have an effect on the sphericity measure-

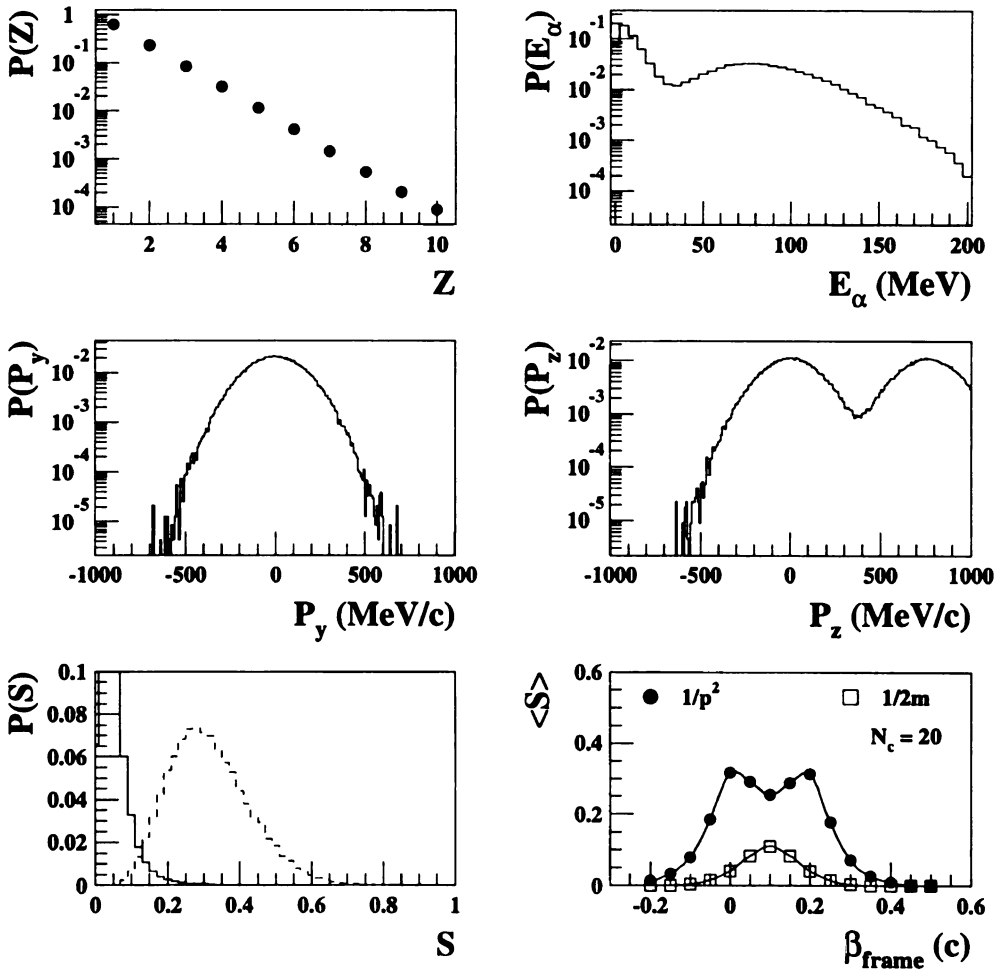

Figure 4.6: Same layout as Figure 4.3. Results of simulation with two spherical sources, one at rest and one moving at $\beta = 0.2$c along the z-axis.

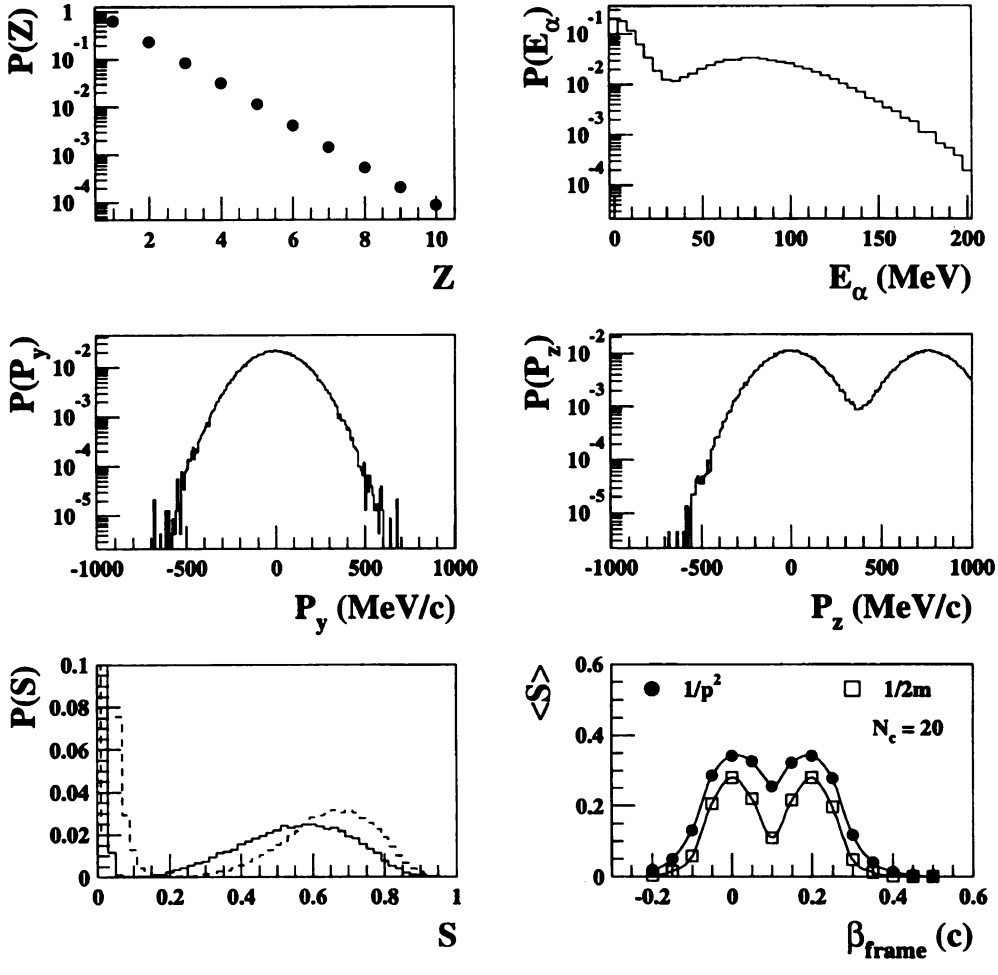

Figure 4.7: Same layout as Figure 4.3. Results of simulation with two spherical sources, one at rest and one moving at $\beta = 0.2c$ along the z-axis. Half the events contain the moving source, and half contain the source at rest.

ment. This effect will be dealt with in two ways: selecting events based on variables known to be related to impact parameter and the careful choice of normalization for the flow tensor.

Figure 4.8 shows plots of $\langle S \rangle$ versus β_{frame} for four of the incident energies studied. The data in these plots were taken with the trigger requiring two particles to be detected in the main ball phoswiches (BALL-2 trigger). Other than this hardware requirement, the data are impact parameter inclusive. The normalization used for the flow tensor is $\frac{1}{2m}$.

The data have been sorted into subsets based on the multiplicity of charged particles detected and fully identified (N_c) in each event. Particles detected with the MWPCs are not included here. The different curves in each plot represent these subsets as indicated by the various symbols superimposed on them (see key). Each multiplicity curve has a shape somewhat reminiscent of the curves generated by the model. That is, there are two peaks (or at least one peak with a large shoulder), one closer to the center-of-mass frame, and one closer to the projectile frame for each energy. We can interpret this as evidence that there is more than one source contributing to these events, as would be expected for impact parameter inclusive data. Notice that the peak at the lower velocity is somewhat to the right of the center-of-mass velocity, while we might expect it occur at exactly that velocity. Most likely this shift is caused by the other source moving at the faster velocity, as described with the simulation. Our first step must be to try to reduce the contribution from this faster source.

In Figure 4.9 mean sphericity versus frame velocity is again shown, but this time only for the 10% most central collisions as determined using the total transverse charge of the event. (Choice of this centrality variable is discussed in Appendix A.) In this figure, The peak at the faster velocities is significantly reduced in size, indicating that

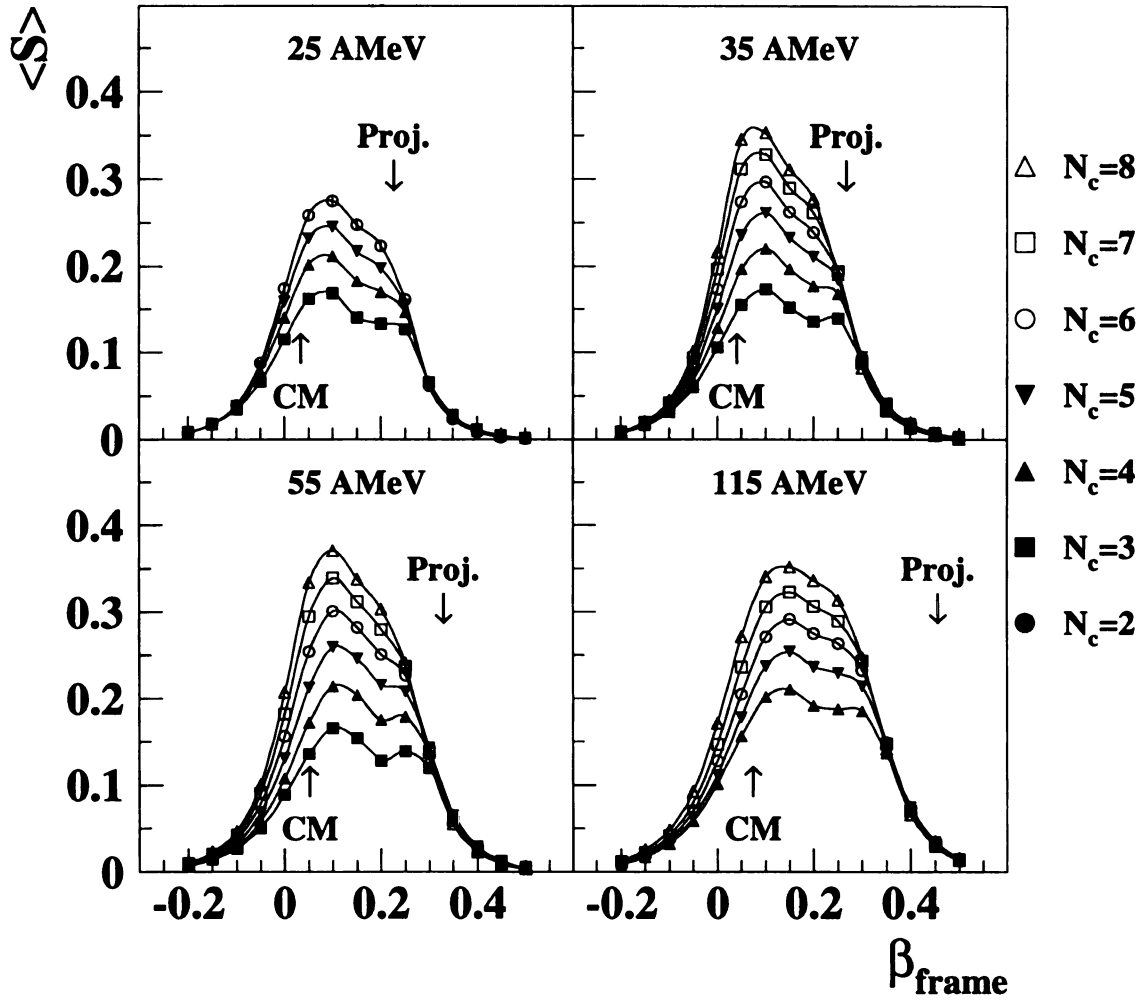

Figure 4.8: Mean sphericity versus frame velocity for impact parameter inclusive events (BALL-2 trigger). The center-of-mass (CM) and projectile (Proj.) velocities are marked on the abscissa by the corresponding arrows. The multiplicity (N_c) of each event set is denoted by the symbols, as shown in the key.

we have removed some portion of the source contributing to it. The leftmost peak is now shifted much closer to the center-of-mass velocity for all four energies. At the three lowest energies, the curve still peaks at velocities slightly higher than that of the center-of-mass. This shift is small but is most likely the residual effect of the faster source. For the 115 AMeV case, the peak is slightly to the left of the center-of-mass velocity. If we are measuring the sphericity accurately, this makes sense because the momentum transfer at this energy is far less than complete, as we learned in the previous chapter.

If the peak at higher velocities is indeed related to a projectile-like source, it is curious that it does not move significantly as the projectile energy increases. This phenomenon is a caused by a trigger bias, both in hardware (the BALL-2 trigger), and in software (the centrality cut). If an event contains particles emitted solely from a source moving faster than ~0.2c, it is likely that most of these particles will be detected at very forward angles, and unlikely that two of them will trigger ball phoswiches. The centrality cut will similarly deselect such events as well. This effect has been modeled using a software replica of the 4π Array, that included a BALL-2 trigger. Using the model, particles were generated from sources moving at speeds of up to $\beta = .5$c, but the $\langle S \rangle$ versus β_{frame} plot always peaked at values closer to $\beta =$ 0.2c.

Thus far, based on the $\langle S \rangle$ vs. β_{frame} plots, we may state that we have significantly reduced the contribution of peripheral events through our centrality cut. However, such a restriction is not absolute, and there are certainly still contributions from faster sources. For this reason, we now investigate the possibility of using the $\frac{1}{p^2}$ normalization for the flow tensor. Figure 4.10 shows $\langle S \rangle$ versus β_{frame} plots using this normalization.

As with the simulation, the two sources have less of an effect on one another if

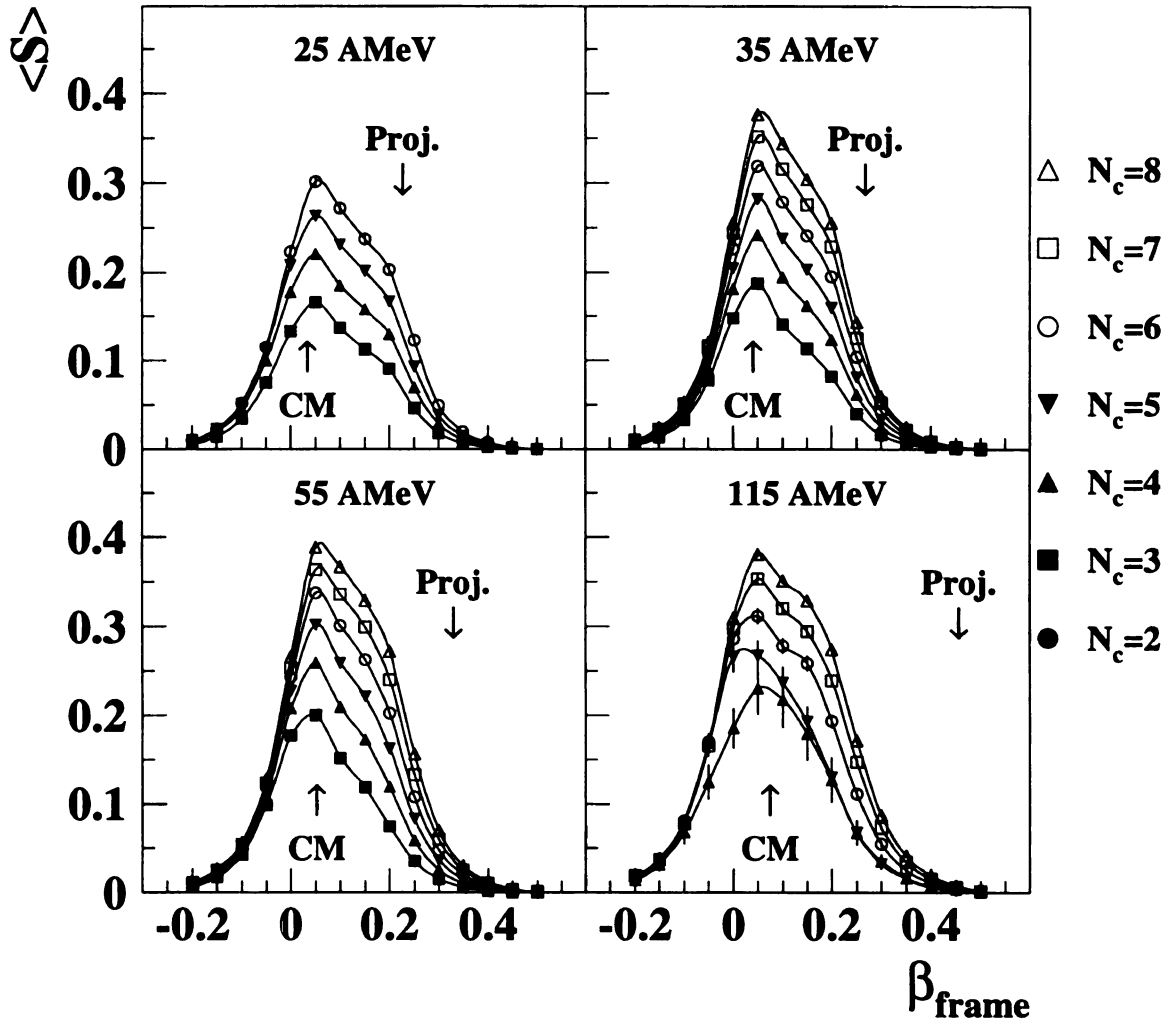

Figure 4.9: Mean sphericity versus frame velocity for the 10% most central events as determined using total transverse charge (Z_T). The flow tensor normalization constant used is $\frac{1}{2m}$.

we use $\frac{1}{p^2}$, and we can see this in the change in the relative size of the two peaks. There is a much greater change in the size of the faster component relative to the change in the size of the center-of-mass component. This may be attributable to the fact that fewer particles in the event set should be coming from this more peripheral source because we are selecting central collisions. When we reduce the influence of the center-of-mass source on this smaller source by using the $\frac{1}{p^2}$ normalization, there is a large change in the sphericity. Conversely, we can infer that removing the influence of the faster source on the center-of-mass source has a smaller but qualitatively similar effect. For this reason, we determine that the $\frac{1}{p^2}$ normalization is superior in cases when the source of interest cannot be completely isolated.

4.4.4 Detector Acceptance Effects

An attempt must always be made to determine the extent to which detector acceptance effects alter the data. In studies like the present one in which observables are being measured over a wide range of beam energies, these acceptance effects may change as the velocity of the emitting source changes. In this study in particular, we are interested in learning if the acceptance will distort the event shape, e.g., will a "rod" become a "sphere" or vice versa, and if this distortion change with beam energy.

We again call on our model to aid in this determination. Nine sets of events with with a spherical momentum distribution ($\sigma_z = \sigma_x = \sigma_y$=1), were generated and boosted to the velocity corresponding to the centers-of-mass of the nine systems studied. These events were then filtered through a software replica of the 4π Array. In order to ensure that the filtered data were realistic, some gross features of the the simulated data, namely Z-distributions, proton energy spectra, and helium energy spectra were compared with the experimental data and adjusted to be a reasonable

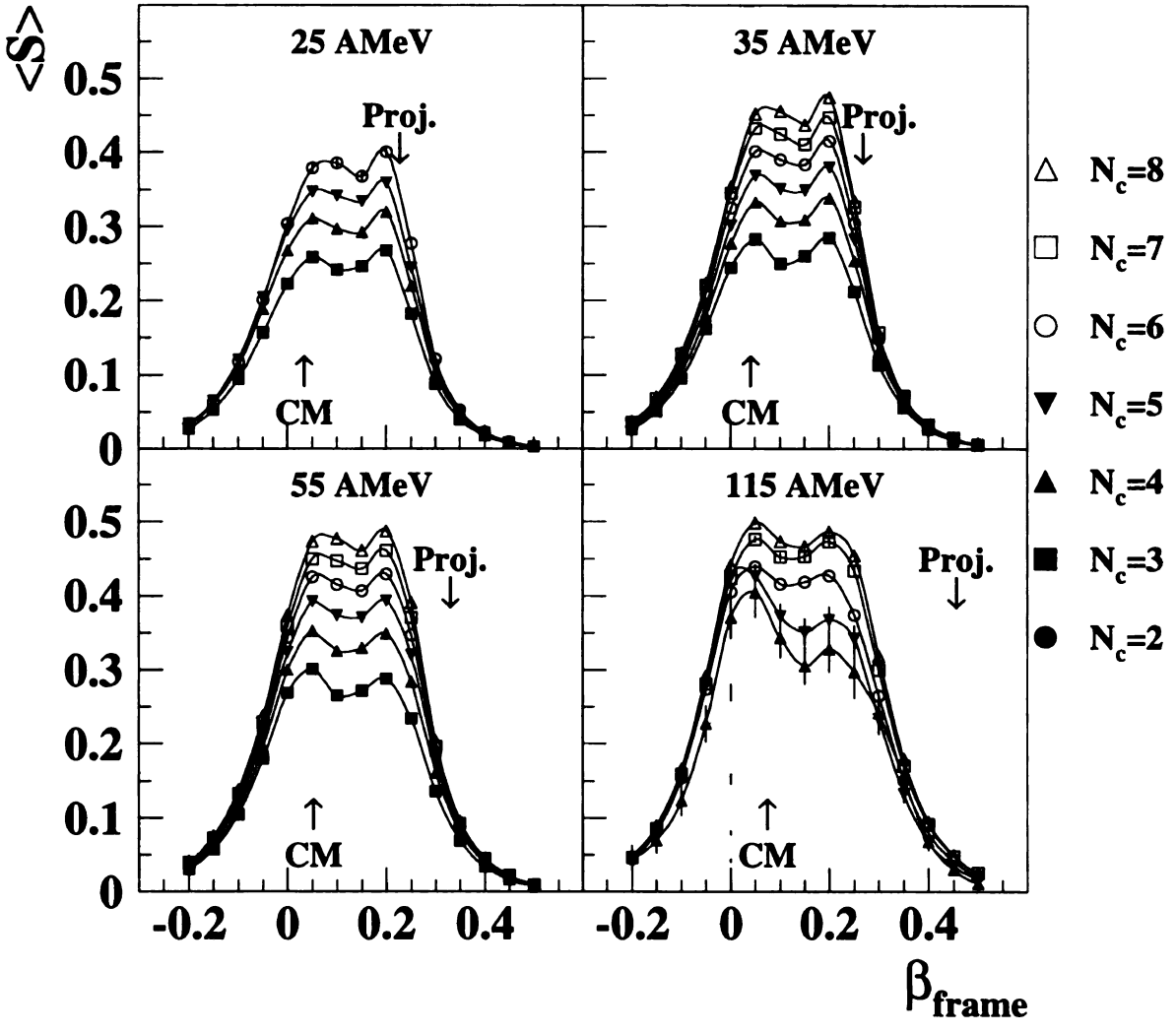

Figure 4.10: Mean sphericity versus frame velocity for the 10% most central events as determined using total transverse charge (Z_T). The flow tensor normalization constant used is $\frac{1}{p^2}$.

match. Since we will explicitly separate events based on their multiplicity, the unfiltered multiplicity distribution need not duplicate the data. Rather, we wish to ensure that the filtered data will have large enough statistics for the range of multiplicities from 2 through 11. Thus, we have selected an unfiltered multiplicity distribution to be a gaussian with a mean of 20 and a standard deviation of 5.

The results of this simulation are shown in Figure 4.11. While there are fluctuations from the unfiltered values of sphericity (marked by arrows), there is no systematic change in $\langle S \rangle$ with beam energy. A spherical event remains a spherical event even after removing several particles. This is to be expected assuming that the particles are removed randomly. There should be no difference between the case of generating 10 particles randomly, and the case of generating 20 particles randomly and then removing 10 randomly. As further empirical proof of this, Figure 4.12 shows the probability distribution for sphericity for events with $N_c = 10$. The three distributions represent data, an unfiltered simulation, and filtered simulation. In the unfiltered simulation, events with $N_c = 10$ were generated, and in the filtered simulation events with $N_c = 20$ were generated and only those events with $N_c = 10$ after filtering are shown. The three curves are essentially identical.

One may not expect a rod-like momentum distribution to retain its shape in the way that a spherical distribution does, since the particles are emitted preferentially along an axis. If this axis tends to be aligned consistently with one region of poor acceptance, such as down the beam pipe, particles emitted along that axis will be deselected over those emitted perpendicular to it. This could cause a rod-like distribution to become more spherical. To test this effect a rod-like set of events ($\sigma_z = 2.5\sigma_x = 2.5\sigma_y$), were generated and filtered as in the spherical case. This aspect ratio was chosen because it produced values of $\langle S \rangle$ close to those of the 15 and 25 AMeV data. The elongated axis of the rod was chosen to be the beam axis to

Table 4.1: Unfiltered values of $\langle S \rangle$ for a rod-shaped event generated by the model with $\sigma_z = 2.5\sigma_x = 2.5\sigma_y$.

N_c	2	3	4	5	6	7	8	9	10	11
$\langle S \rangle$	0.17	0.21	0.23	0.25	0.26	0.27	0.28	0.29	0.29	0.29

test for the worst case. Figure 4.13 shows the values of $\langle S \rangle$ for several multiplicities versus beam energy. The unfiltered values of $\langle S \rangle$ for each multiplicity are listed in Table 4.1. There is an apparent shift upward after filtering for all beam energies. This effect is small for the low multiplicities but grows stronger as multiplicity increases, although none of the shifts increase the value of $\langle S \rangle$ up to the spherical limit for a given multiplicity. Most importantly, this shift shows no dependence on beam energy. Therefore, any beam dependent changes in sphericity seen in the data cannot be attributed to the acceptance. However, the overall values of sphericity must now be interpreted carefully. One should also remember that this test was done for the worst case scenario of a rod oriented along the beam direction, and in the actual data this effect is not as strong.

4.4.5 Collective Effects

One topic not dealt with explicitly in this analysis is that of collective motion of the nuclei such as transverse flow or rotation. Such effects could, theoretically reduce the value of sphericity by elongating or flattening the emission pattern. This topic was dealt with by Cebra [Cebr 90], and such effects were found to be small relative to the elongating effect of sequential emission, particularly for central collisions.

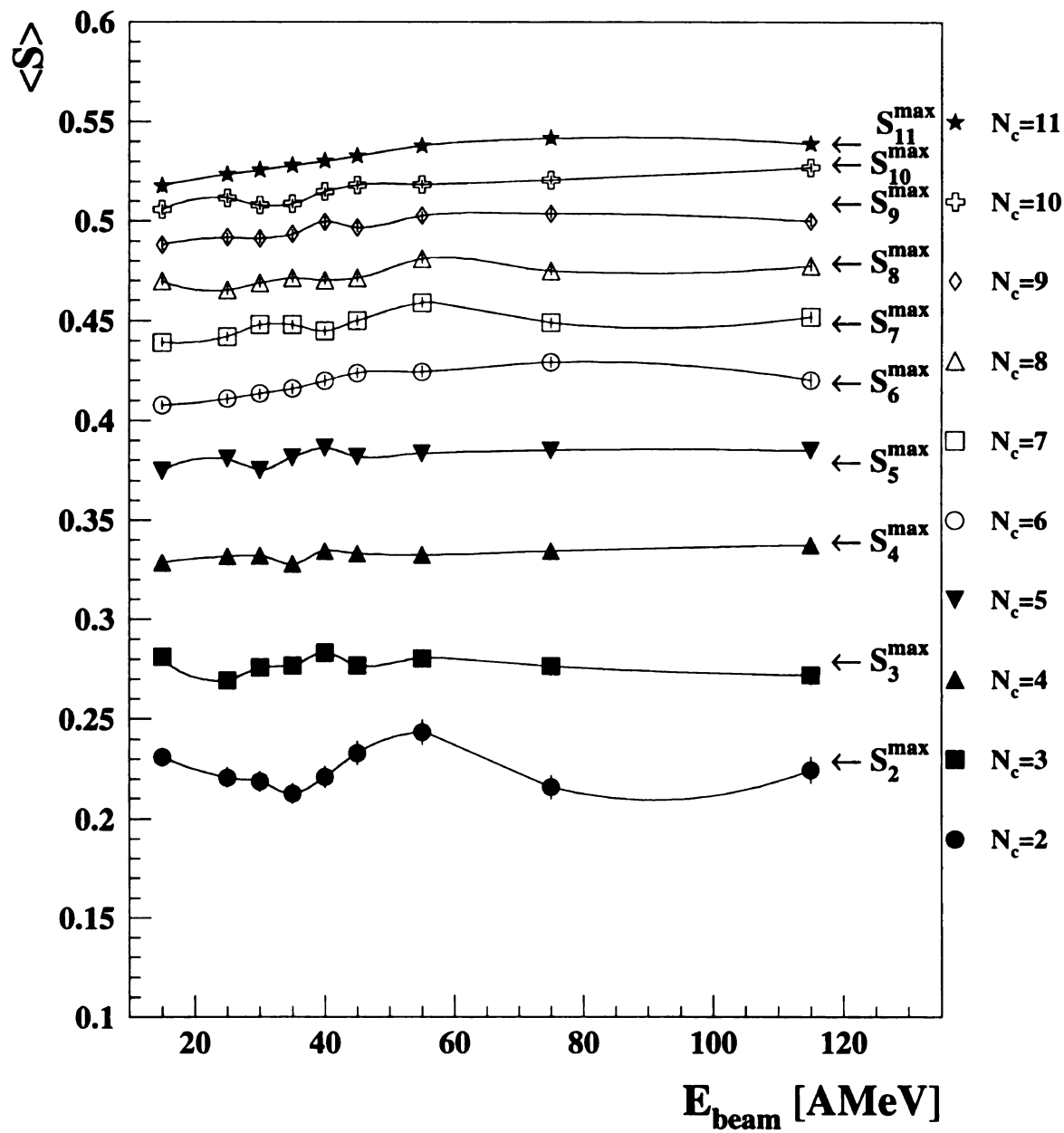

Figure 4.11: Mean sphericity versus beam energy for 9 event sets each generated with a spherical flow ellipsoid, and boosted to one of the center-of-mass velocities corresponding to the 9 beam energies. The data was then filtered through a software replica of the 4π Array.

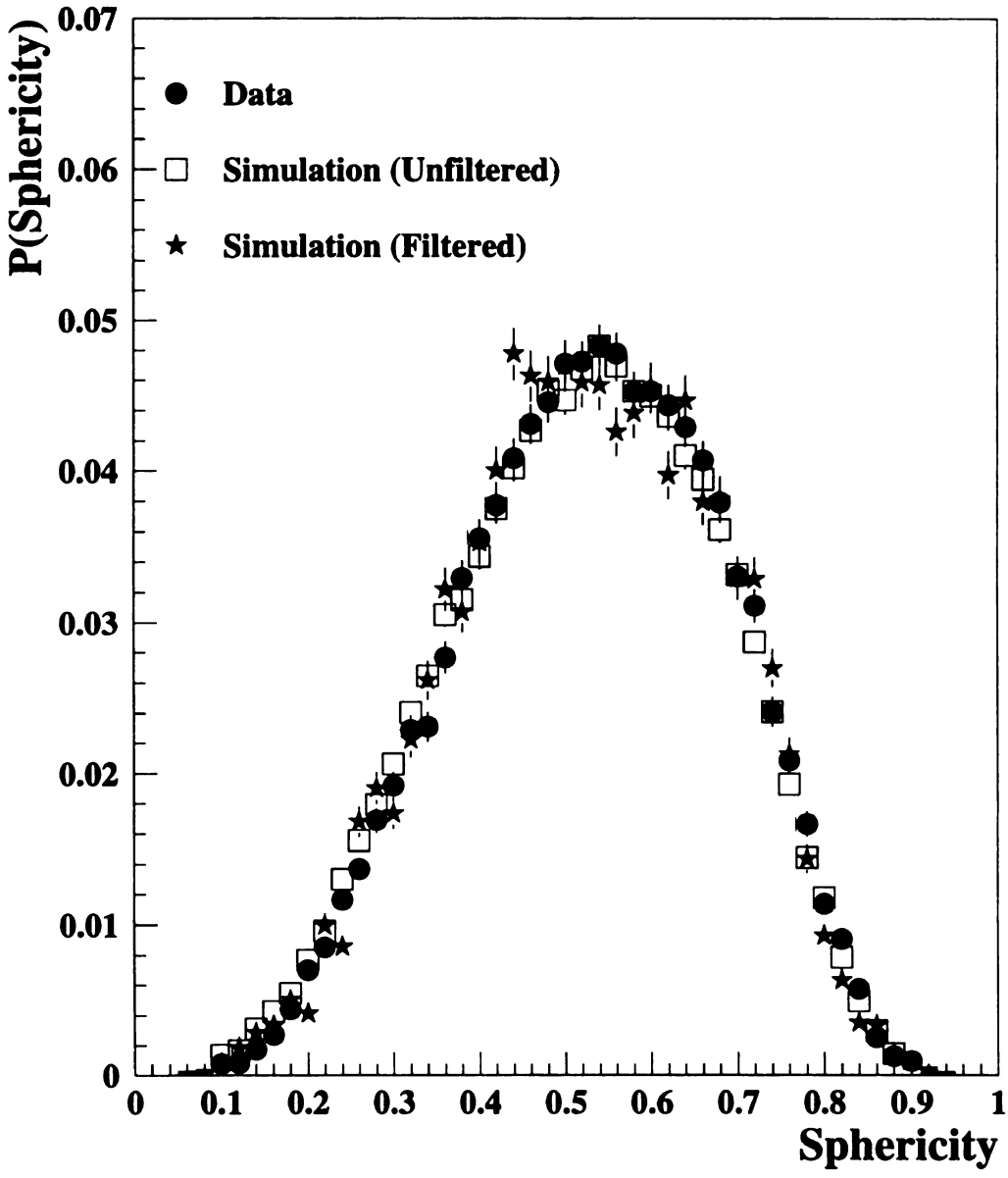

Figure 4.12: Sphericity probability distribution for events with multiplicity $N_c = 10$, from experimental data, unfiltered simulation, and filtered simulation. For the unfiltered simulation, all events were generated with $N_c = 10$. For the filtered simulation, events were generated with $N_c = 20$, and only those events with $N_c = 10$ after filtering are plotted.

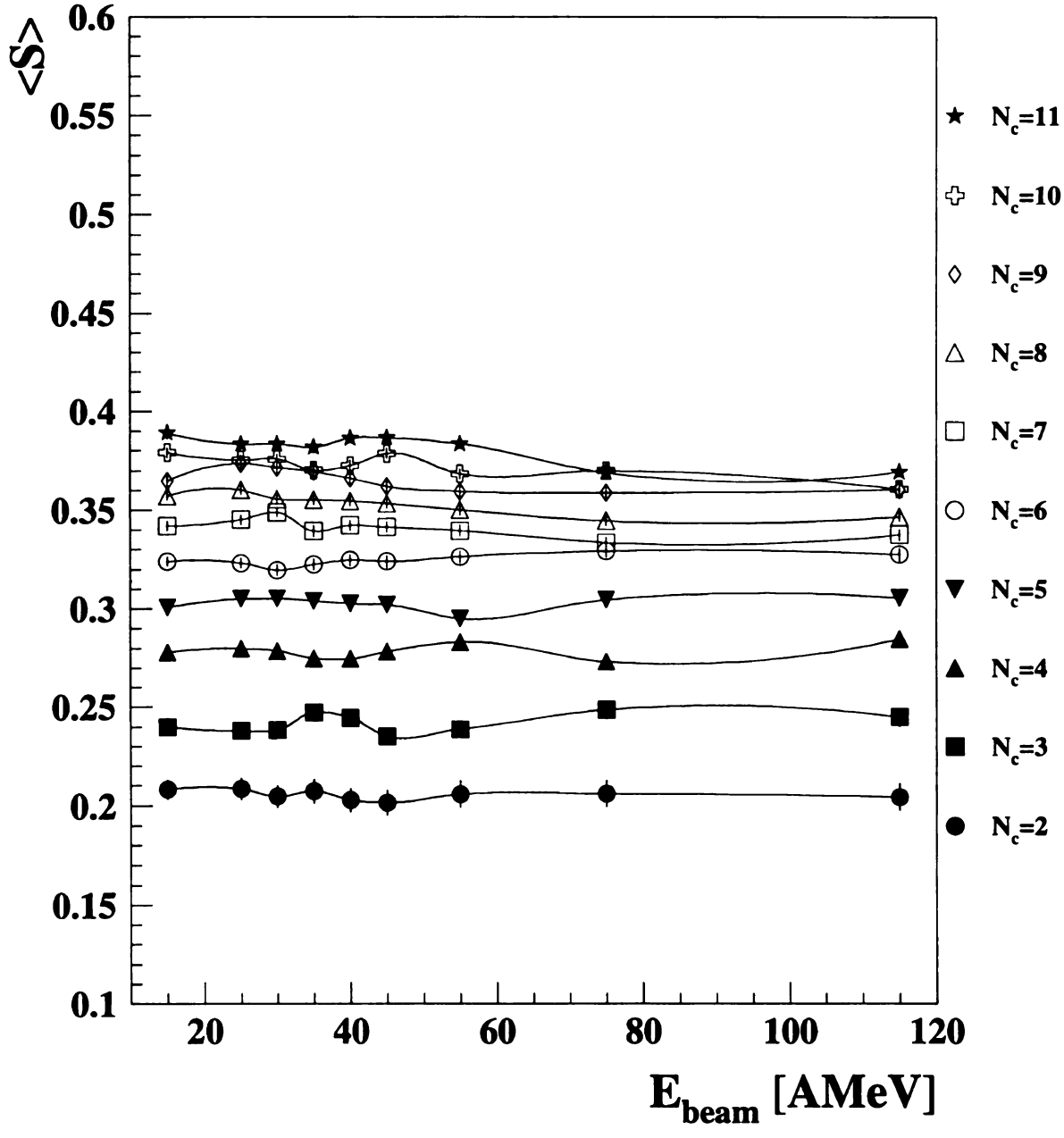

Figure 4.13: Mean sphericity versus beam energy for 9 event sets each generated with a rod-like flow ellipsoid, and boosted to one of the center-of-mass velocities corresponding to the 9 beam energies. The data was then filtered through a software replica of the 4π Array.

4.5 Evolution of Sphericity with Beam Energy

In the previous section, the various effects that may distort the measured values of sphericity were described and the techniques for dealing with them were presented. In this section, using these techniques we will present the final result of the sphericity analysis: the evolution of the sphericity of central collisions with beam energy.

Figure 4.14 shows $\langle S \rangle$ versus multiplicity of identified charged particles for four incident energies, and the expected increase of $\langle S \rangle$ on N_c is apparent. However for a given multiplicity, there is an increase in $\langle S \rangle$ as beam energy increases.

This effect is seen more clearly in Figure 4.15 we plot $\langle S \rangle$ versus beam energy, explicitly separating events by their multiplicity. Data points are not available for all combinations of multiplicity and beam energy. This is due to a dearth of events at high(low) energies with low(high) multiplicities, which makes sense as charged particle multiplicity is itself a measure of the violence of the collision. For all multiplicities, there is an increase in $\langle S \rangle$ from 15 AMeV up to ~55 AMeV, after which the value plateaus. In fact, the values at which each curve saturates are very close to, in fact exceed, the values obtained if one simulates a set of events with a perfectly spherical distribution and calculates the average multiplicity. This would indicate that the particle emission at energies above ~50 AMeV in the $^{40}Ar + ^{232}Th$ is, on average, isotropic. However, remembering the tendency of the acceptance to artificially increase sphericity, we may only say that the emission is becoming *more* isotropic with beam energy. The increase of $\langle S \rangle$ to values *higher* than the isotropic value was not reproduced using the model coupled with the filter. However, we hypothesize that it is an acceptance effect which causes this phenomenon. If values of sphericity that occur rarely and fall on the low tail of the sphericity distribution (4.12), are suppressed by the detector acceptance, this could shift the value of the mean upward.

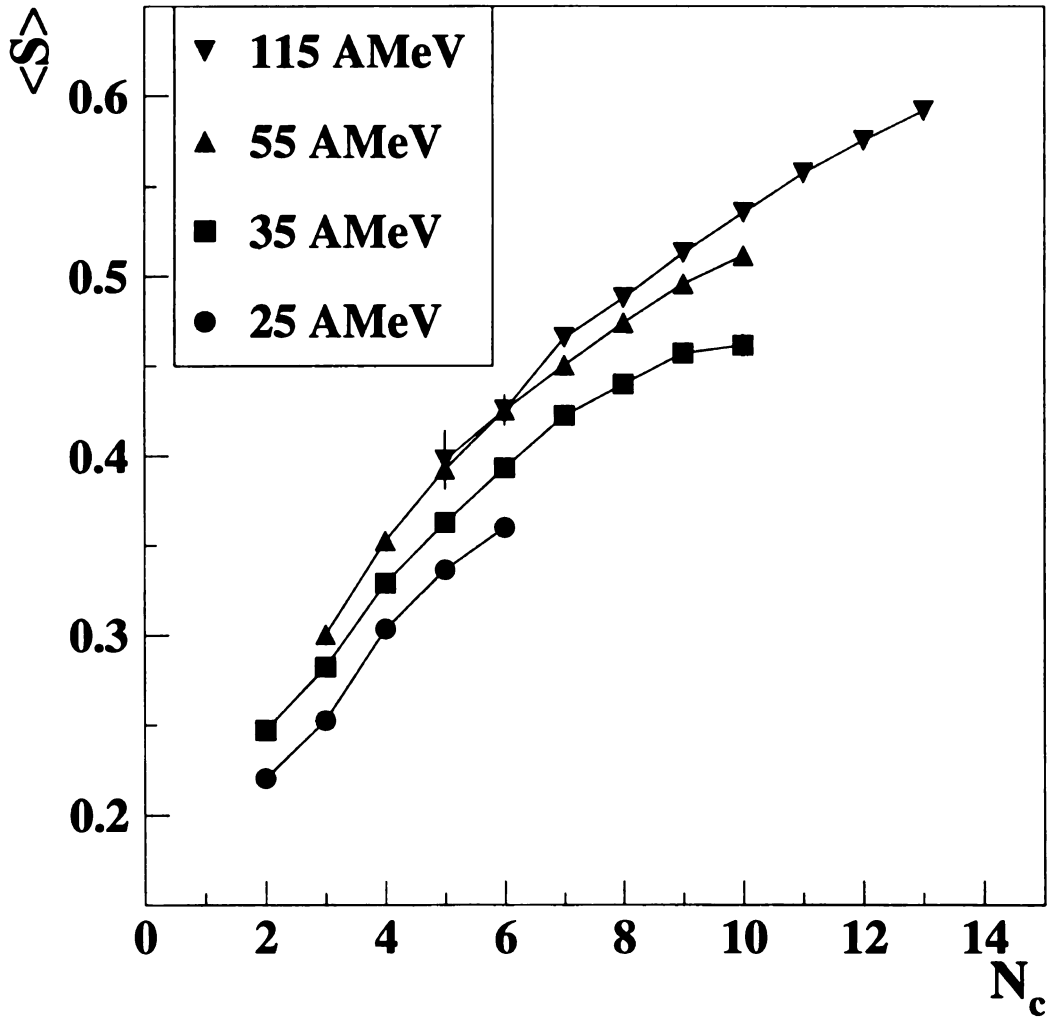

Figure 4.14: Mean values of sphericity plotted versus charged particle multiplicity (N_c), for four incident beam energies of $^{40}Ar + ^{232}Th$. The data is for central collisions.

Thus far, we have only included fully identified particles in the sphericity analysis. That is, we have excluded fission fragments since we do not have easy experimental access to their energy. However, in using the $\frac{1}{p^2}$ normalization, the energy of the particles is not needed explicitly in the flow tensor. Only the angles of emission are needed, and these are very well known for the fission fragments due to the excellent angular resolution of the MWPCs. However, the velocity of the fragments is needed in order to correctly transform the angles them to the center of mass frame. The velocity can be estimated quite accurately using the Viola prescription [Poll 84, Viol 85] described in the previous chapter. The results of including the fission fragments in the sphericity calculation are shown in Figure 4.16. This plot is very similar to the preceding one except for two features. First, since we have added particles, the statistics are improved and we are able to include data points for energy and multiplicity combinations not possible without including the fission fragments. Second, the values of $\langle S \rangle$ are slightly suppressed at the lower energies. This latter point makes sense as we are adding particles that are emitted along, in fact define, a particular axis, and would tend to elongate the shape of the particle flow ellipsoid.

For completeness, we include a plot of $\langle S \rangle$ versus beam energy using the $\frac{1}{2m}$ normalization, for the same set of central events used in the preceding two plots. In Figure 4.17, the same upward trend is seen in the curves from 15 AMeV, up to 55 AMeV. However, beyond that point the curves fall back down again. This is a verification that the faster source has a large influence on the value of sphericity calculated in the center-of-mass frame, and justifies our choice of the $\frac{1}{p^2}$ normalization. As the projectile velocity grows increasingly larger than the center-of-mass velocity, the value of $\langle S \rangle$ becomes increasingly suppressed. Since switching to the $\frac{1}{p^2}$ normalization increases the values of $\langle S \rangle$ at the highest energies relative to those at the lower energies, we conclude that the effect of the faster source is relatively small at the lower energies.

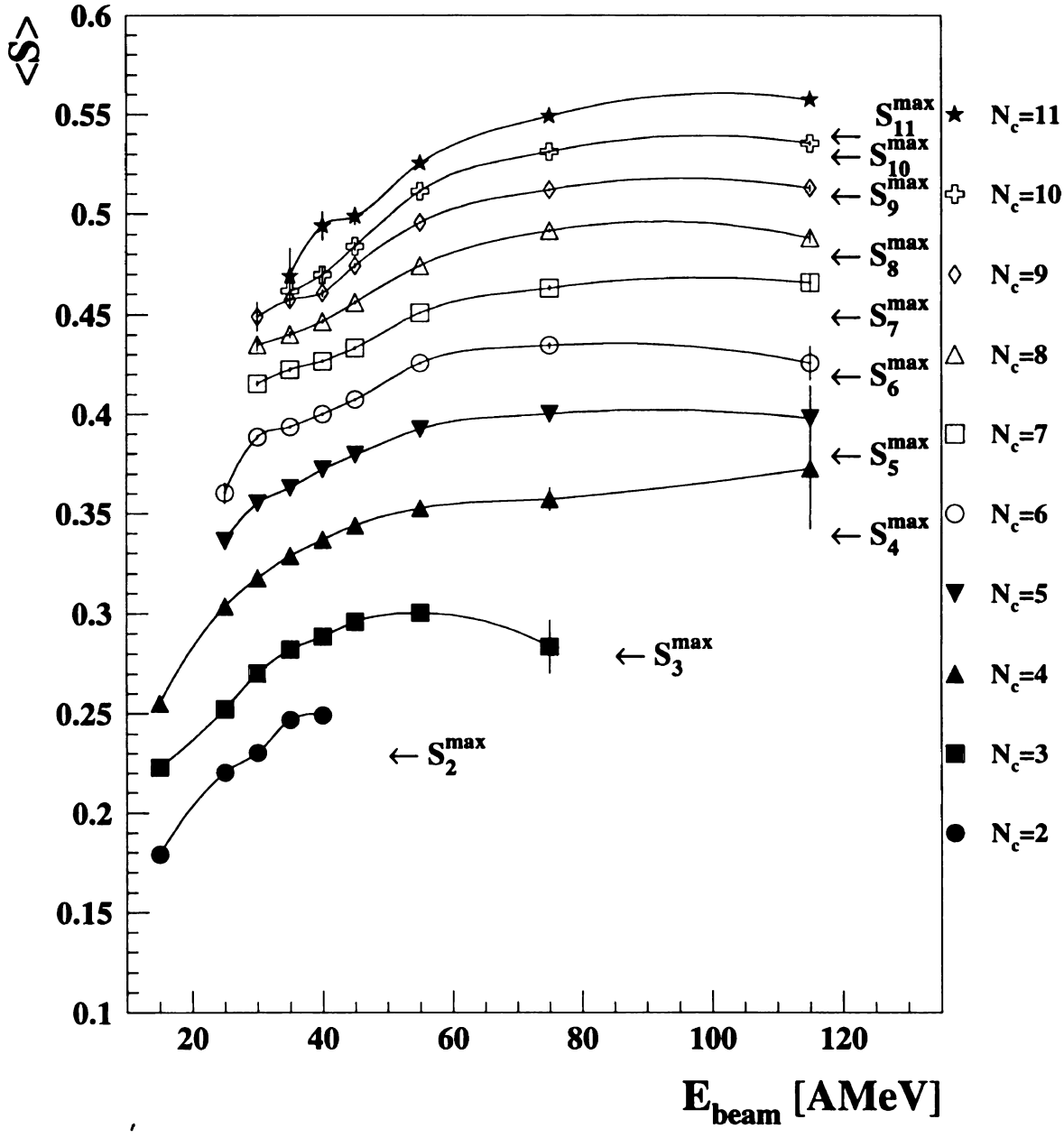

Figure 4.15: Mean sphericity versus beam energy for central collisions as determined using total transverse charge (Z_T). Events are divided into subsets based on multiplicity (N_c) to treat the multiplicity distortions explicitly. The $\frac{1}{p^2}$ normalization is used here, and only fully identified particles (no fission fragments) are included.

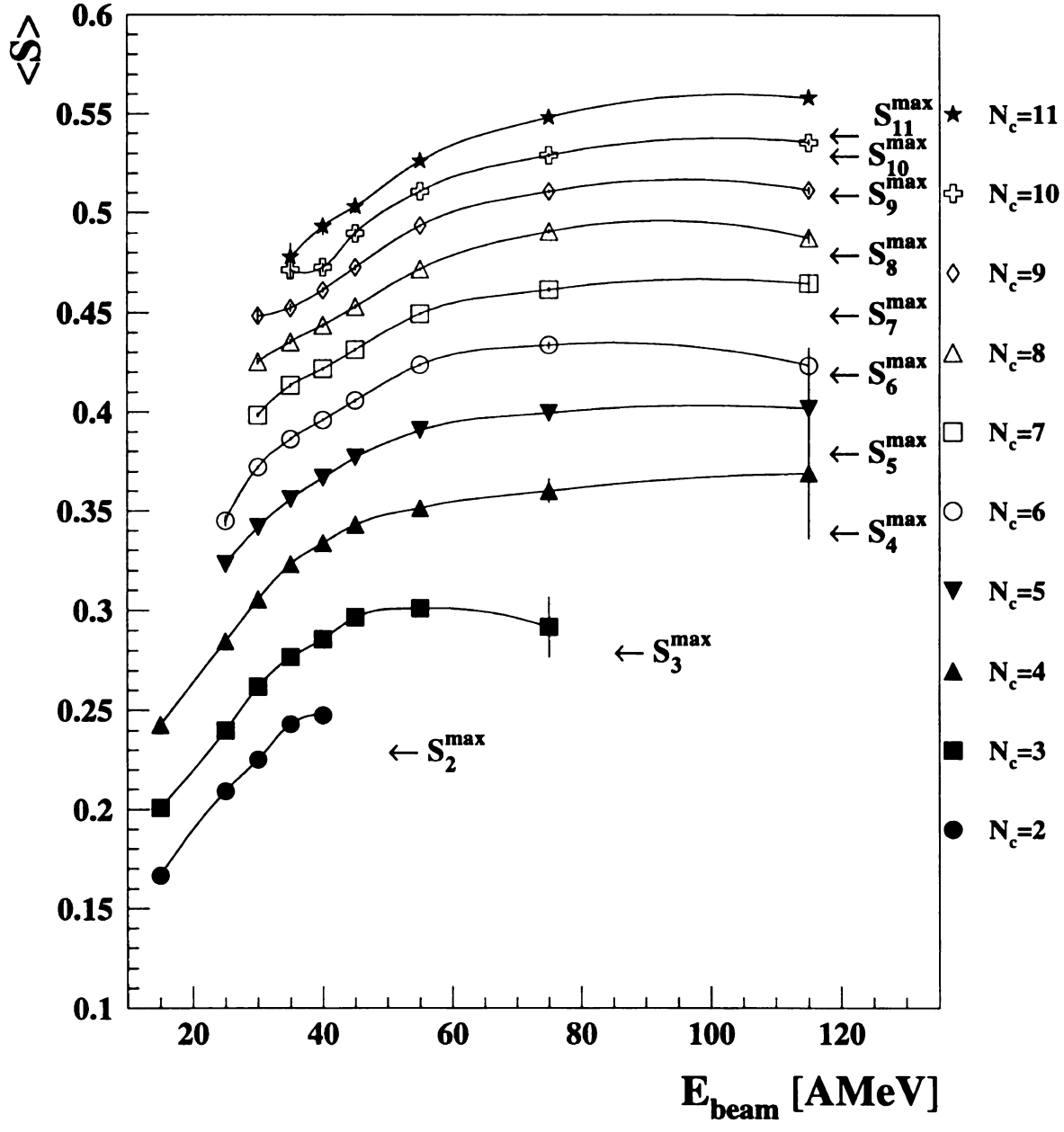

Figure 4.16: Mean sphericity versus beam energy for central collisions as determined using total transverse charge (Z_T). Events are divided into subsets based on multiplicity (N_c) to treat the multiplicity distortions explicitly. The $\frac{1}{p^2}$ normalization is used here, and fission fragments are included.

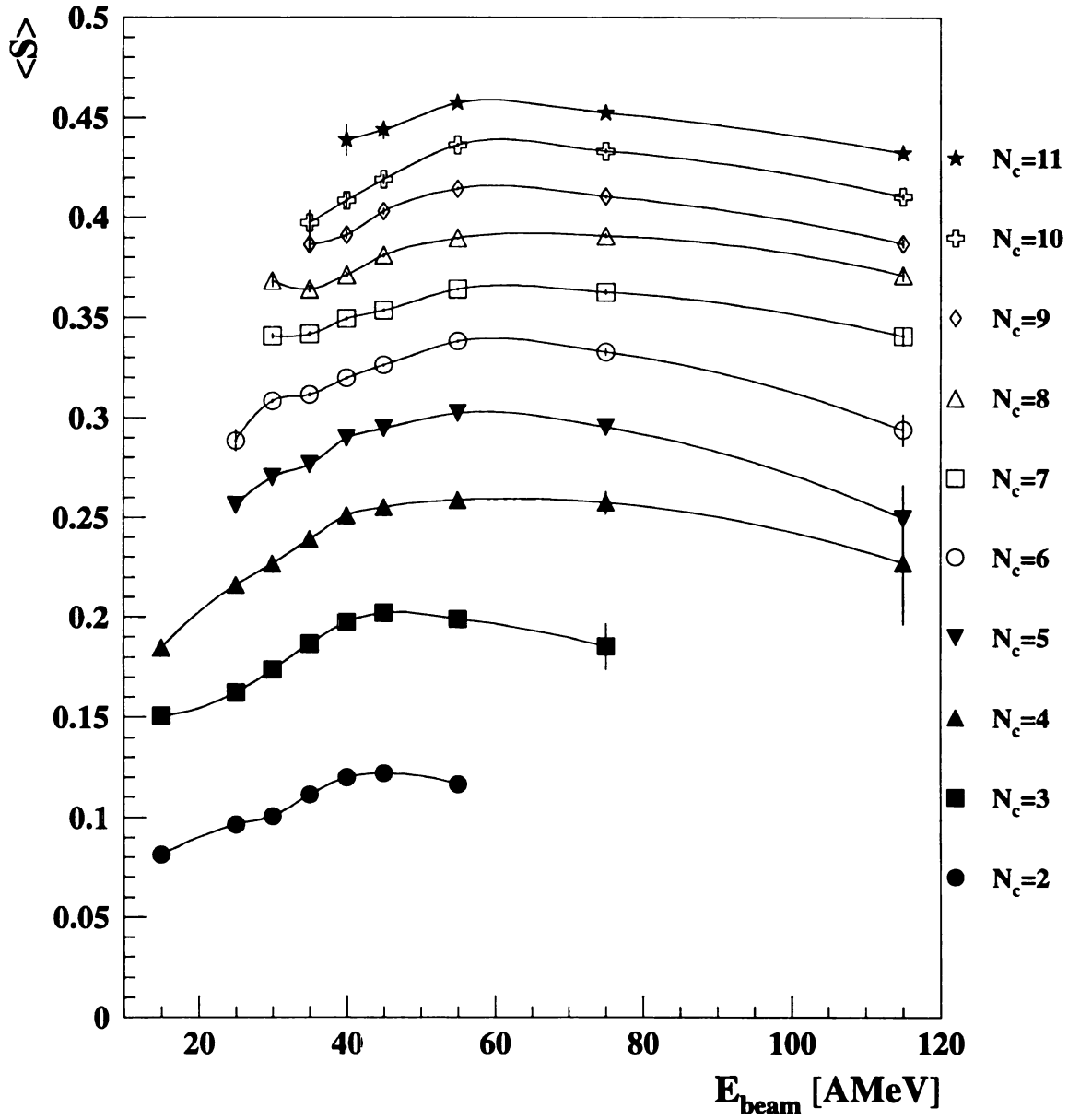

Figure 4.17: Mean sphericity versus beam energy for central collisions as determined using total transverse charge (Z_T). Events are divided into subsets based on multiplicity (N_c) to treat the multiplicity distortions explicitly. The $\frac{1}{2m}$ normalization is used here, and only fully identified particles (no fission fragments) are included.

4.6 Summary and Discussion

In this chapter we have shown that there is a significant increase in the average sphericity of central collisions of ^{40}Ar + ^{232}Th as bombarding energy increases. For energies above ~50 AMeV, the measured value of $\langle S \rangle$ is close to the value obtained from an isotropic distribution. This increase is similar to what has been seen previously in studies of symmetric systems [Cebr 90, Cebr 90a, Barz 91]. It has been suggested through various model calculations that sphericity is expected to be higher for the simultaneous breakup of a system than for sequential breakup through a series of binary decays, and may approach isotropy [Lope 89, Cebr 90, Cebr 90a, Harm 90, Barz 91]. We interpret our results as signifying a gradual change in the dominant reaction mechanism from a sequential binary decay (e.g fusion-fission) to a more prompt scenario (e.g. multifragmentation). However, due to acceptance effects which cause an overall upward shift in $\langle S \rangle$ for all beam energies, we can only place a lower limit on the bombarding energy at which we believe the prompt mechanism becomes dominant. We report this bombarding energy to be 50 AMeV.

Chapter 5

Conclusion

To study the evolution of the reaction mechanism in central collisions of heavy ions on fissionable targets, we studied the ^{40}Ar + ^{232}Th system at bombarding energies ranging from 15 - 115 AMeV using the MSU 4π Array. At the time of the experiment, the Array consisted of the 30, recently completed, multi-wire proportional counters for the detection of fission fragments, backed by 55 Bragg Curve Counters for the detection of intermediate mass fragments, and finally backed by 170 high dynamic range fast/slow plastic phoswiches for the detection of particles with charges from Z= 1-8. An additional array of 45 plastic phoswiches covered forward angles.

Disappearance of Fusion-fission

While the fusion-fission process was found to decline steadily in central collisions as bombarding energy is increased, in agreement with previous measurements, evidence of a fission-like reaction mechanism has been found in the ^{40}Ar + ^{232}Th system in the most central collisions at all bombarding energies studied, including 115 AMeV. That this process is seen at this energy suggests that nuclei are indeed capable of containing large amounts of excitation energy long enough for an inherently slow collective process, such as fission, to occur. However, the probability for this scenario

to occur becomes increasingly unlikely as excitation energies are increased up through $\sim$ 1 GeV.

Momentum Transfer and Excitation Energy

Average momentum transfer has been measured for the impact parameter inclusive fission event set in this system, and the most probable momentum transfer has been measured for the most central events leading to fission. The most probable momentum transfer, as a fraction of beam momentum, is found to follow known systematics as beam velocity is increased [Viol 82, Nife 85], including the two highest energies for which this observable was not previously available for this system. The average momentum transfer was found to fall below the values predicted by the systematics as beam energy increases and the fission channel is fed increasingly by peripheral collisions. The most probable momentum transfer per projectile nucleon saturates at $\sim$170 MeV/c for bombarding energies above 25 AMeV. This is in agreement with previous experimental results [Tsan 84, Conj 85], and provides further evidence that momenta above the Fermi momentum are not easily imparted to a compound system [Woo 83, Sain 84].

Trends in average IMF and LCP production indicate that increasing amounts of energy are being deposited in the ^{40}Ar + ^{232}Th system as beam energy increases. A calculation of excitation energy based on an empirical relationship with momentum transfer also indicates that excitation energy is increasing, and agrees well with the values predicted by a schematic, hydrodynamic model [Harp 71, Desb 87, Cerr 89].

Event Shape Analysis

An analysis of the evolution of the event shape shows an increase in the average sphericity of the most central events as beam energy increases. This increase is most rapid in the 15 - 45 AMeV range and then saturates near the the value corresponding to an isotropic distribution. This can be interpreted as a transition in the dominant reaction mechanism from a sequential binary decay to a simultaneous one [Lope 89, Cebr 90a]. However, due to acceptance effects which can shift the measured value of sphericity uniformly upward for all energies studied, we can only put a lower limit on the beam energy at which this transition might be complete. This energy is 55 AMeV.

APPENDICES

Appendix A

Impact Parameter Filters

A.1 Method

In many experiments, including the present one, it is desirable to make exclusive measurements of the properties of central collisions. One of the most powerful advantages of a 4π device is its ability to act as an impact parameter filter and aid in these measurements. Impact parameter is not directly accessible experimentally, but there are several "centrality" variables which have been shown to be correlated with impact parameter [Cava 90, Phai 92], and which the MSU 4π Array can determine rather well. These variables include total charged particle multiplicity (N_c), midrapidity charge (Z_{mr}), total transverse kinetic energy (E_T), and total transverse charge (Z_T).

Total transverse kinetic energy is defined as the sum over the transverse kinetic energy of each particle in an event:

$$E_T = \sum_i E_i sin^2\theta_i = \sum_i (p_i sin\theta_i)^2/2m_i. \qquad \text{(A.1)}$$

Similarly total transverse charge is defined as the sum over the charge of each particle in the event, weighted by its polar angle:

$$Z_T = \sum_i Z_i sin\theta_i. \qquad \text{(A.2)}$$

Midrapidity charge is the sum over the charge of all particles having a rapidity in the center-of-mass which is greater that 75% of the center-of-mass target rapidity (y') and less than 75% of the center-of-mass projectile rapidity, i.e.:

$$0.75y'_{targ} \leq y' \leq 0.75y'_{proj}. \tag{A.3}$$

The lab rapidity , y, of a particle is defined as

$$y = \frac{1}{2}ln\{(\sqrt{m^2+p^2} + pcos\theta)/(\sqrt{m^2+p^2} - pcos\theta)\} = tanh^{-1}(\beta cos\theta,) \tag{A.4}$$

where m, β, and p denote the particle's mass, velocity, and momentum, respectively.

To obtain a quantitative estimate of impact parameter from these variables, we use the geometrical prescription of Reference [Cava 90]. It is assumed that each variable (q) is monotonically related to impact parameter (b) and the following relation can be written:

$$\frac{2\pi bdb}{\pi b_{max}^2} = \pm f(q)dq, \tag{A.5}$$

where b_{max} is the maximum impact parameter of the reaction and $f(q)$ is the probability density function of q. That is, $f(q)dq$ is the probability of detecting a collision with a value of q' between q and $q+ dq$. The function $f(q)$ is normalized to unity; the plus/minus signs indicate that the variable q increases/decreases as b increases. Integrating Equation A.5 from b to b_{max} we obtain:

$$\int_b^{b_{max}} \frac{2bdb}{b_{max}^2} = \pm \int_{q(b)}^{q(b_{max})} f(q')dq'. \tag{A.6}$$

If we let

$$F(q) = \pm \int_{q(b)}^{q(b_{max})} f(q')dq', \tag{A.7}$$

then

$$b/b_{max} = \sqrt{1 - F(q)}. \tag{A.8}$$

Using Equation A.8 one can easily make an estimate of impact parameter. The experimental distribution of the centrality variable, q is integrated, and the value of q corresponding to the desired value of b/b_{max} is determined. This value is then used as a threshold to accept or reject events. In the present data, q was chosen such that the largest values of b allowed are $\sim 0.31 b_{max}$. This corresponds to $\sim$ 10% of the measured cross section. If the measured cross section were assumed to be equivalent to the geometric (hard sphere) cross section, then b_{max} would be the sum of the target and projectile radii ($R_p + R_t$). However, due to trigger bias and detector acceptance, the actual impact parameter leading to a triggering event is less than ($R_p + R_t$) [Llop 95]. Thus, we can consider $0.31(R_p + R_t)$ to be an upper limit for our maximum impact parameter.

A.2 Choice of Centrality Variable

In order to decide which of these variables to use, one must determine which is most efficient at selecting central collisions for the system under study. One must also check the degree to which the observables of interest autocorrelate with the chosen centrality variable [Conr 93, Llop 95].

A.2.1 Correlation with Folding Angle

In Chapter 3, the correlation between impact parameter and fission fragment folding angle was discussed. It was explained that central, high LMT events lead to folding angles of $\sim 100^\circ$ - 110° , and peripheral, low LMT collisions give folding angles of $\sim 160^\circ$ - 170° , for this system. In Figures A.1-A.4, the four centrality variables are plotted versus folding angle (Θ_{ff}). While there is a general correlation between all of the centrality variables and the folding angle which grows stronger as beam energy increases, the degree of this correlation is not the same for all of the variables.

Figure A.5 shows this effect more dramatically. In this plot, the folding angle distributions from central collisions as defined by the various centrality variables mentioned above, are shown. All of the variables suppress the target fission peak, relative to the high LMT peak (compare Figure 3.2). However, at the low energies there are some qualitative differences. We can state that E_T and Z_T are superior at suppressing the peripheral component and are the preferred choices.

A.2.2 Sphericity as a Test of a Centrality Variable's Efficiency

Sphericity can also be used to test a centrality variables ability to suppress peripheral collisions. As stated in Chapter 4, sphericity is maximum when it is calculated in the frame of the emitting source. Thus, if there is more than one source velocity, there should be more than one frame in which sphericity reaches a (local) maximum. This was shown to be true in Chapter 4 as there were two bumps in the $\langle S \rangle$ vs. β_{frame} curves for central events chosen with Z_T, one near the center-of-mass velocity and one at much faster velocities. By plotting $\langle S \rangle$ versus β_{frame} for central collisions selected with different variables, we can roughly compare the relative size of this faster, projectile-like contribution. We can also compare the positions of the center-of-mass peaks, assuming that this peak will be shifted to faster velocities if there is a stronger contribution from peripheral collisions.

As Figures A.6 and A.7 show, Z_T seems to do a better job suppressing the projectile-like source. The size of this contribution is smaller, and the peak is located at slower velocities than when E_T is used. Thus we can say that Z_T is our first choice as a centrality variable, with E_T also being acceptable.

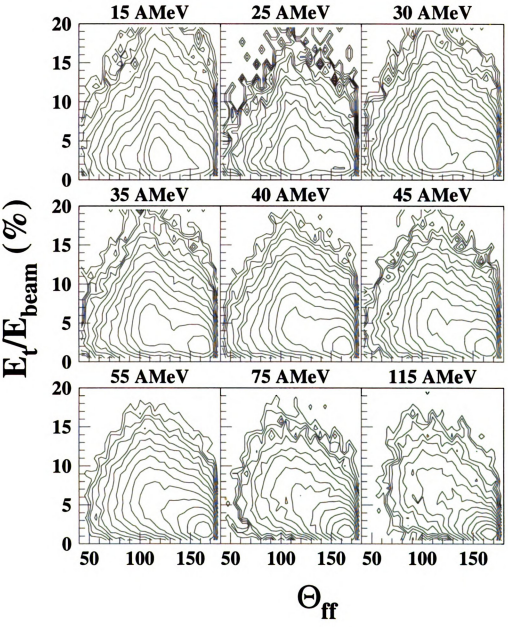

Figure A.1: Contour plot of total transverse kinetic energy (E_T) versus fission fragment folding angle (Θ_{ff}).

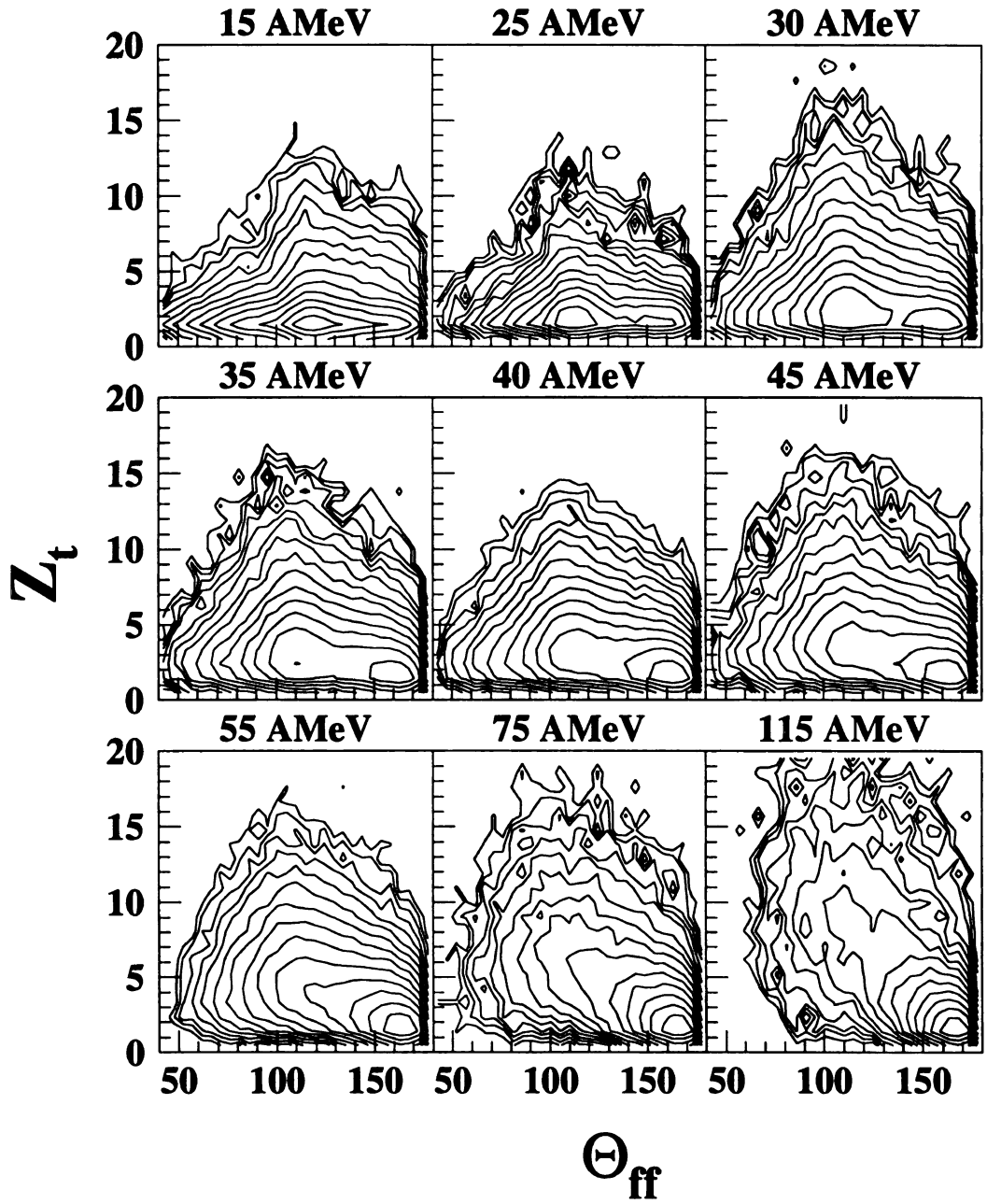

Figure A.2: Contour plot of total transverse charge (Z_T) versus fission fragment folding angle (Θ_{ff}).

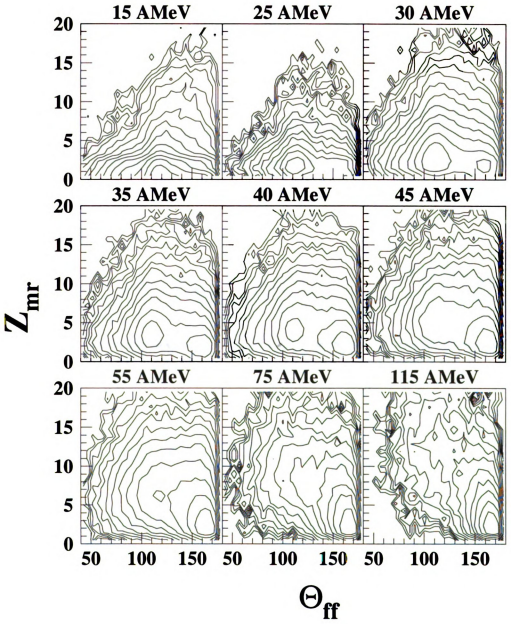

Figure A.3: Contour plot of midrapidity charge (Z_{mr}) versus fission fragment folding angle (Θ_{ff}).

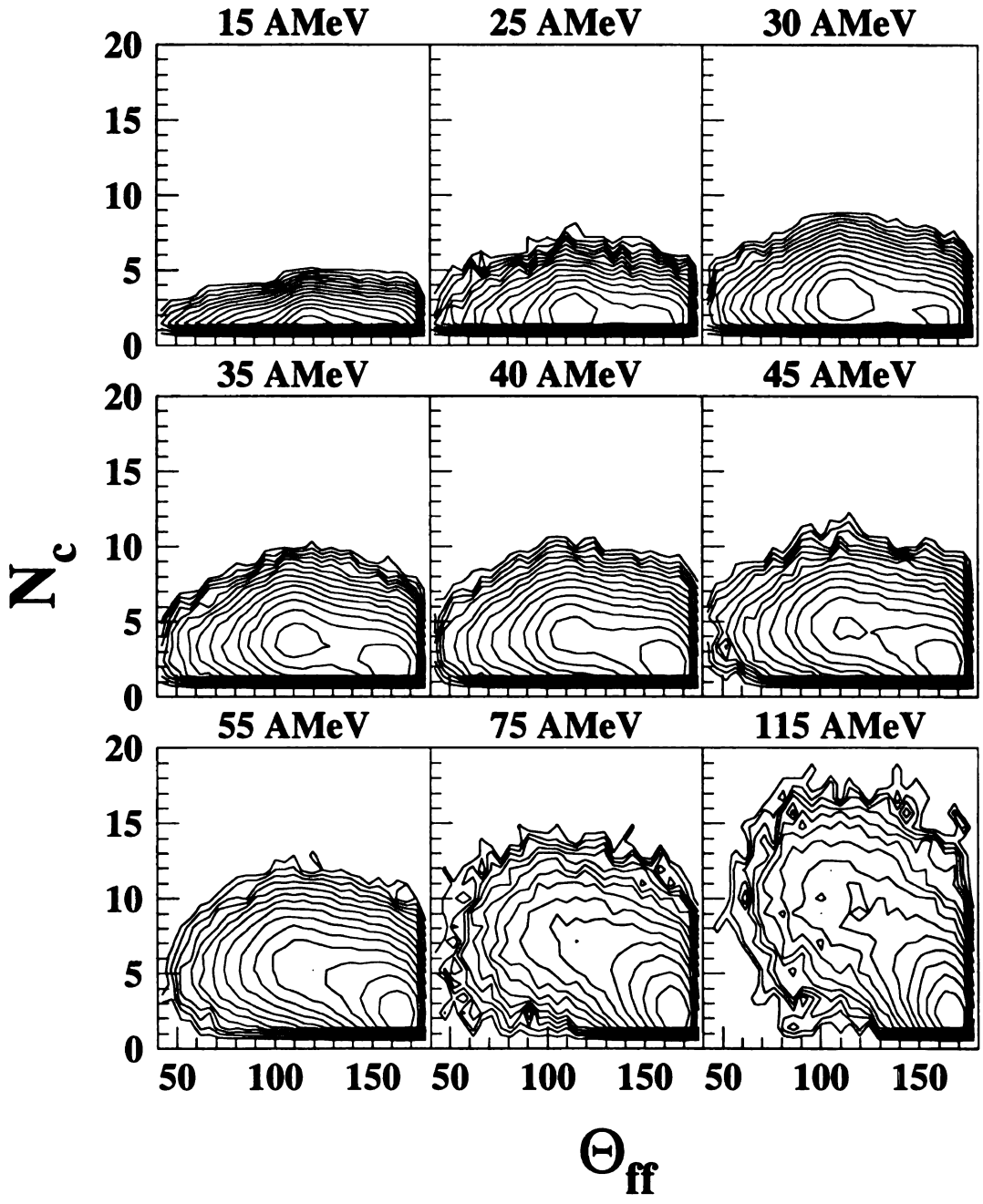

Figure A.4: Contour plot of identified charged particle multiplicity (N_c) versus fission fragment folding angle (Θ_{ff}). The fission fragment multiplicity was not included in N_c.

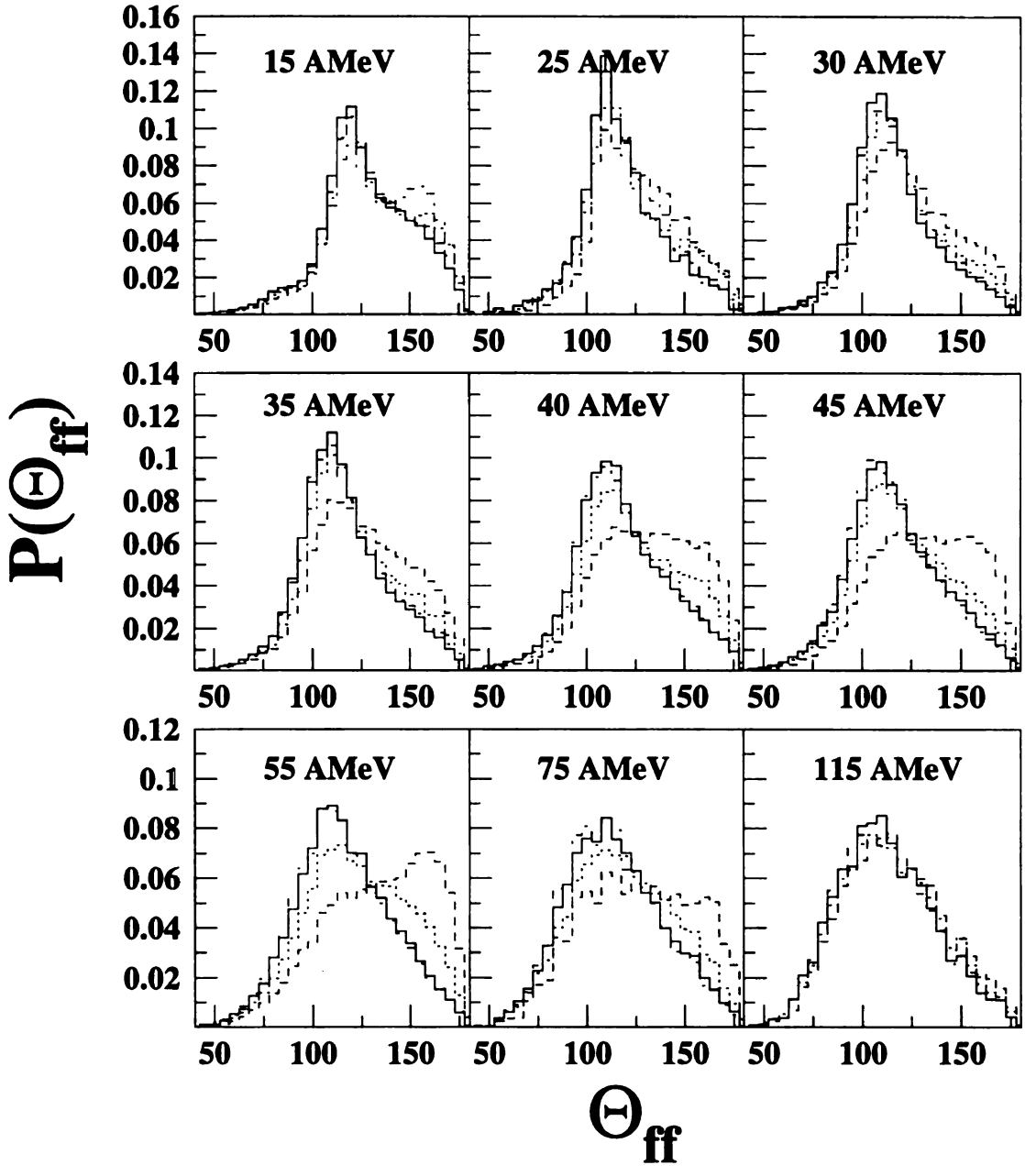

Figure A.5: Folding angle distributions for central collisions as defined by the four variables E_T (solid), Z_T (dot-dash), Z_{mr} (dashed), and N_c (dotted). All distributions are normalized to unit area.

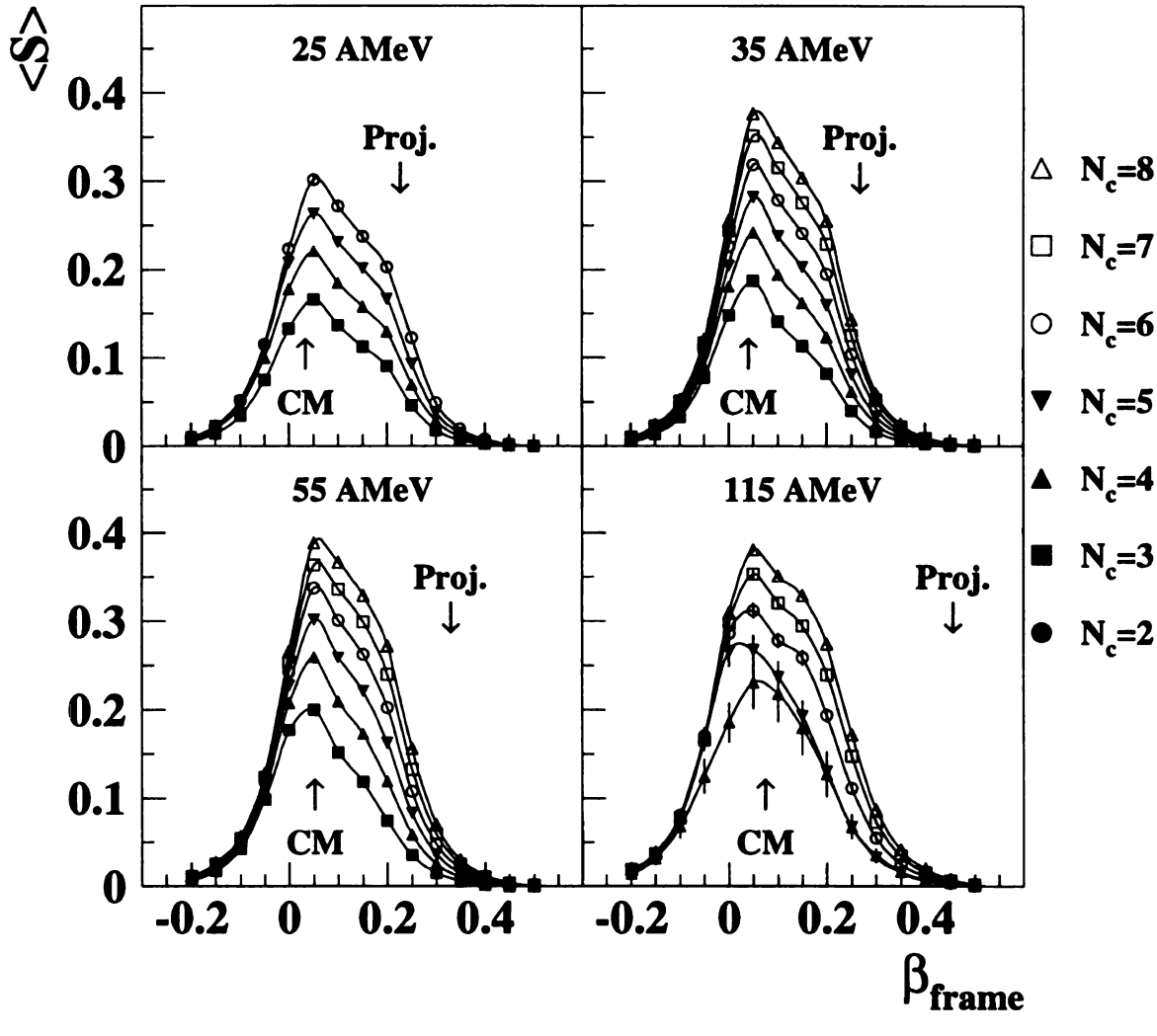

Figure A.6: Mean sphericity versus frame velocity for the 10% most central events as determined using total transverse charge (Z_T). The flow tensor normalization constant used is $\frac{1}{2m}$.

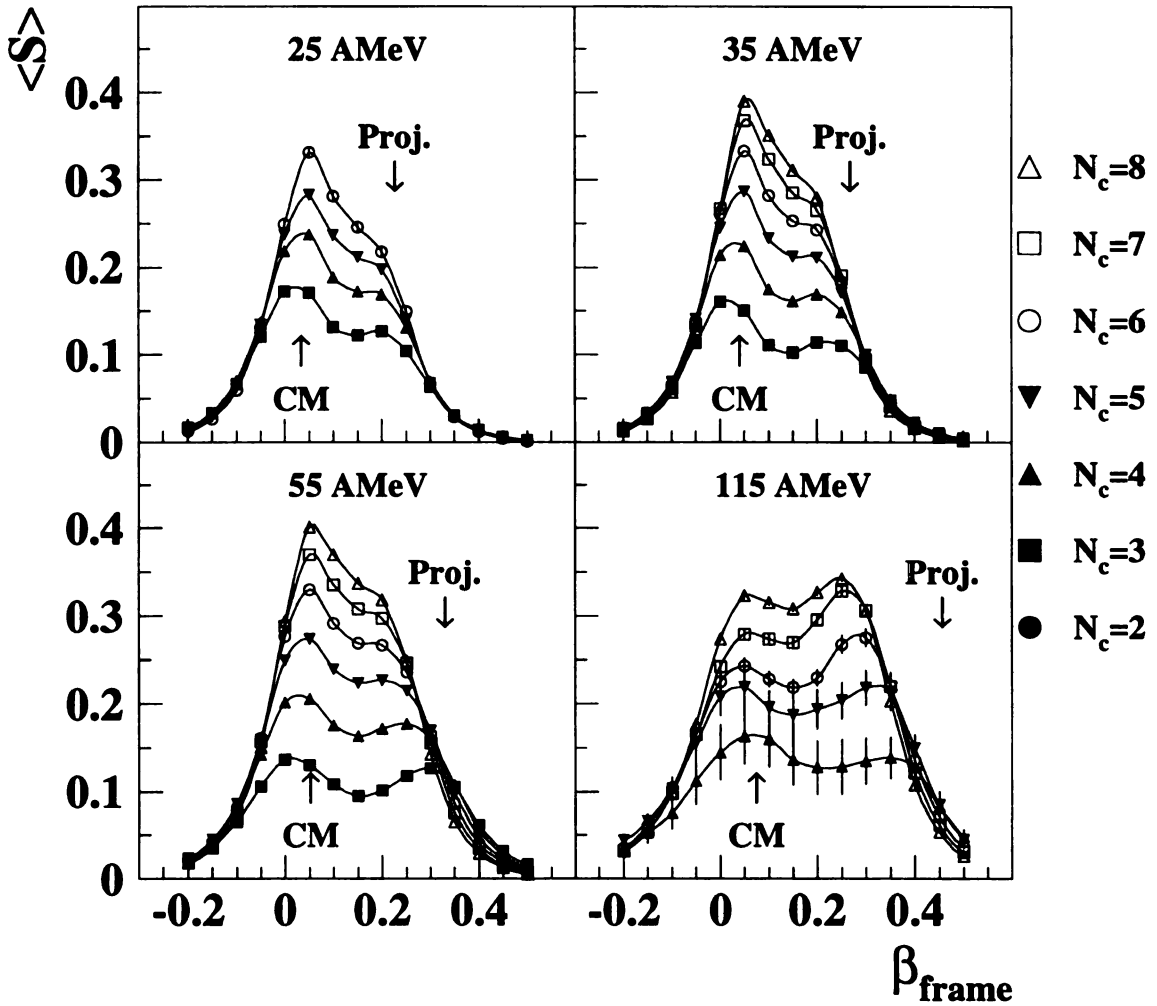

Figure A.7: Mean sphericity versus frame velocity for the 10% most central events as determined using total transverse kinetic energy. (E_T). The flow tensor normalization constant used is $\frac{1}{2m}$.

A.2.3 Autocorrelations

Having decided that E_T and Z_T are the preferred choices for centrality variables, we must now check the extent to which they autocorrelate with the observables we wish to study. Ideally, the variable upon which a centrality cut is made should be tightly correlated with the impact parameter, and negligibly correlated with the experimental observable in all ways except through the impact parameter. Charge, mass, and momentum conservation laws can cause significant "autocorrelations" between a centrality variable and an observable, and may artificially enhance or suppress the measured value of that observable in events which are selected using the centrality variable [Llop 95].

We make the assumption that the width, σ, of an observable in a subset of events selected with a certain centrality variable will be suppressed if there is a significant autocorrelation with that variable. Thus we may compare the widths resulting from gating on different variables in order to choose one that autocorrelates the least, assuming that the gates leading to the largest widths are least autocorrelated. In Figure A.8 we make this comparison for our measurements of $\langle N_{IMF} \rangle$.

From Figure A.8 one can see that the beam energy dependence of $\langle N_{IMF} \rangle$ does not change significantly from one centrality variable to the other. There are, however, significant shifts up or down in the entire excitation function depending on which centrality variable is chosen; Z_T and Z_{mr} give the highest values, N_c gives the lowest, and E_T falls somewhere in the middle. That these relationships do not change with beam energy suggests that they have more to do with the centrality variable rather than a physical effect [Llop 95], and this is borne out by looking at the associated widths in the middle frame of Figure A.8.

The first thing to note about $\sigma(N_{IMF})$ for all the centrality variables is that

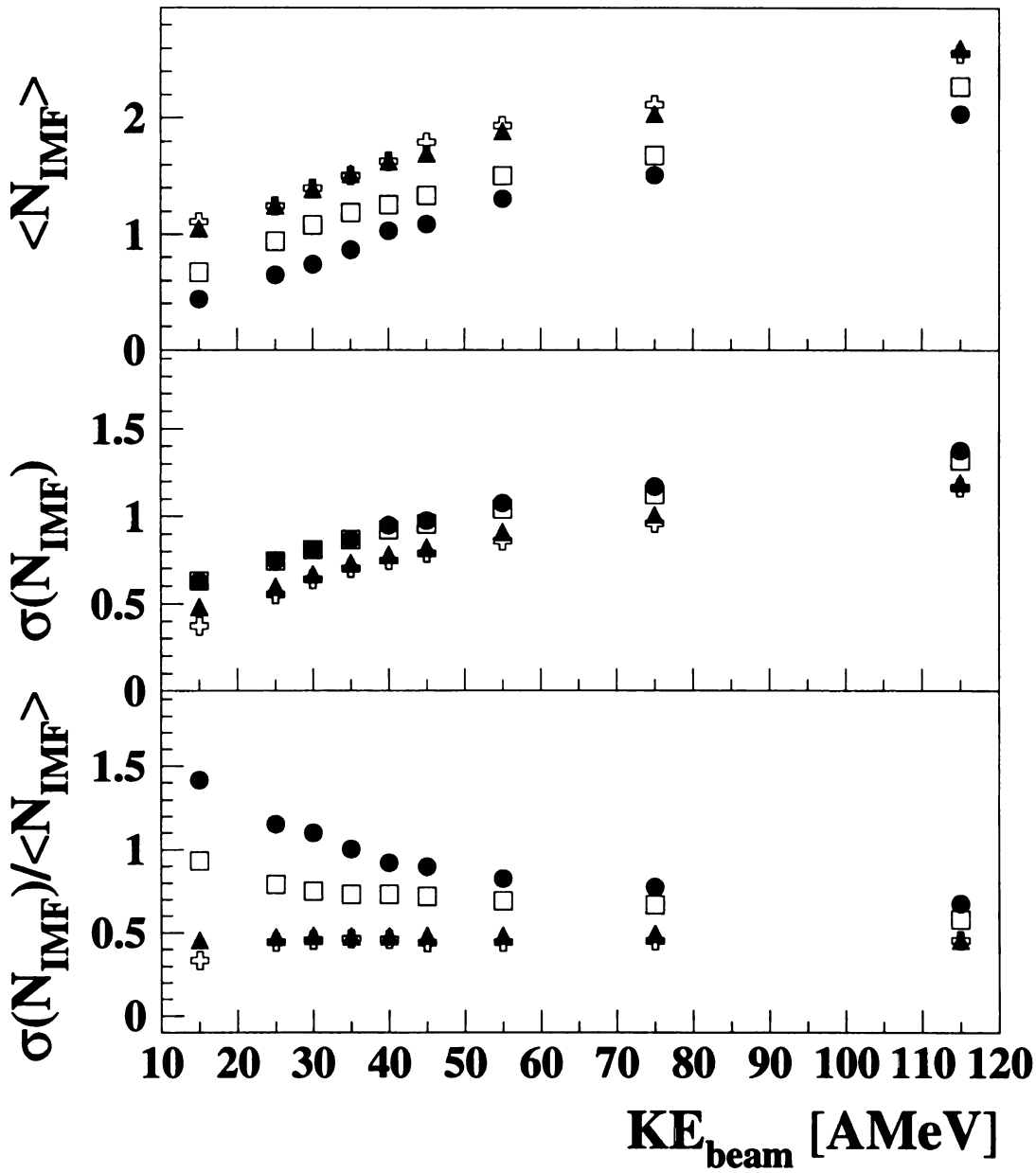

Figure A.8: Means (top frame), widths(middle frame) and reduced widths (bottom frame) for N_{IMF} distributions in the 10% most central events as determined by N_c (solid circle), E_T (open square), Z_{mr} (open crosses), and Z_T (solid triangles).

they are quite large relative to $\langle N_{IMF} \rangle$. However, two distinct groups are evident: one containing Z_{mr} and Z_T, and one containing E_T and N_c. The widths resulting from the Z_{mr} and Z_T cuts are smaller than those resulting from the E_T and N_c cuts, indicating that the former variables autocorrelate more strongly than latter ones, and should be avoided. This result agrees with that of Reference [Llop 95].

The bottom frame of Figure A.8 shows that the reduced widths, $\frac{\sigma(N_{IMF})}{\langle N_{IMF} \rangle}$, for the E_T and N_c selected events are similar for the highest three energies, but differ greatly at the lower energies with $\frac{\sigma(N_{IMF})}{\langle N_{IMF} \rangle}$ being much higher for N_c. This can be explained by what we have already shown in Section A.2.1: N_c is not a sensitive indicator of central events at low energies, most likely due to the relatively low numbers of charged particles produced in these collisions. Thus, we are left with E_T as an appropriate variable to use in our studies of $\langle N_{IMF} \rangle$.

A similar study has been done by Llope et al. [Llop 93] to test the autocorrelation of sphericity with six different centrality variables including most of those presented here. This study included data from five symmetric systems ranging in size from C + C to Xe + La, and beam energies ranging from 15 AMeV to 155 AMeV. It was found that for cuts on the order of 10%, such as those used in this analysis, there are no significant autocorrelations for any of the centrality variables. We make the assumption that the same is true in this data, and choose Z_T as our centrality variable for sphericity studies based on the arguments of Section A.2.2.

BIBLIOGRAPHY

Bibliography

[Awes 81] T.C. Awes, G. Poggi, C.K. Gelbke, B.B. Back, B.G. Glagola, H. Breuer, and V.E.Viola, Jr., Phys. Rev. **C24**, 89 (1981).

[Back 80] B.B. Back, K.L. Wolf, A.C. Mignerey, C.K. Gelbke, T.C. Awes, H. Breuer, V.E. Viola, Jr., P. Dyer, Phys. Rev. **C22**, 1927 (1980).

[Barz 91] H.W. Barz, D.A. Cebra, H. Schulz, G.D. Westfall, Phys. Lett. **B267**, 317 (1991).

[Bege 92] M. Begemann-Blaich, Th. Blaich, M.M.Fowler, J.B. Wilhelmy, H.C. Britt, D.J. Fields, L.F Hansen, R.G. Lanier, D.J. Massoletti, M.N. Bamboodiri, B.A. Remington, T.C. Sangster, G.L. Struble, M.L. Webb, Y.D. Chan, A. Dacal, A. Harmon, J. Pouliot, R.G. Stokstad, S. Kaufman, F. Videbaek, Z.Fraenkel, Phys. Rev. **C45**, 677 (1992).

[Bhat 89] S. Bhattacharya, J.N. De, K. Krishan, S.K. Samaddar, Phys. Rev. Lett. **62**, 2589, (1989).

[Biza 93] G. Bizard, R. Bougault, R. Brou, J. Colin, D. Durand, A. Genoux-Lubain, J.L. laville, C. Le Brun, J.F. Lecolley, M. Louvel, J. Péter, J.C. Steckmeyer, B. Tamain, A. Badala, T. Motobayashi, G. Rudolf, L. Stuttgé, Phys. Lett. **B302**, 162 (1992).

[Bowm 91] D.R. Bowman, G.F. Peaslee, R.T. de Souza, N. Carlin, C.K. Gelbke, W.G. Gong, Y.D. Kim, M.A. Lisa, W.G. Lynch, L. Phair, M.B. Tsang, C. Williams, N. Colonna, K. Hanold, M.A. McMahan, G.J. Wozniak, L.G. Moretto, W.A. Friedman, Phys. Rev. Lett. **67**, 1527 (1991).

[Blai 92] Th. Blaich, M. Begemann-Blaich, M.M. Fowler, J.B. Wilhelmy, H.C. Britt, D.J. Fields, L.F. Hansen, M.N. Namboodiri, T.C. Sangster, Z. Fraenkel, Phys. Rev. **C45**, 689 (1992).

[Bond 90] J.P. Bondorf et al., Phys. Lett **150B**, 57 (1985).

[Bond 90a] J.P. Bondorf, C.H. Dasso, R. Donangelo, and G. Pollarolo, Phys. Lett. **240B**, 28 (1990).

[Camp 84] X. Campi, J. Desbois, E. Lipparini, Phys. Lett. **B142**, 8 (1984).

[Cava 90] C. Cavata, M. Demoulins, J. Gosset, M.-C. Lemaire, D. L'Hôte, J. Poitou, O. Valette, Phys. Rev. **C42**, 1760 (1990).

[Cebr 90] D.A. Cebra, Ph.D. Thesis, Michigan State University,1990.

[Cebr 90a] D.A. Cebra, S. Howden, J. Karn, A. Nadasen, C.A. Ogilvie, A. Vander Molen, G.D. Westfall, W.K. Wilson, J.S. Winfield, and E. Norbeck, Phys. Rev. Lett. **64**, 2246 (1990).

[Cebr 91] D.A. Cebra, S. Howden, J. Karn, D. Kataria, M. Maier, A. Nadasen, E. Norbeck, C.A. Ogilvie, N. Stone, D. Swan, A. Vander Molen, W.K. Wilson, J.S. Winfield, J. Yurkon and G.D. Westfall, Nucl. Inst. and Meth **A300**, 518 (1991).

[Cerr 89] C.Cerruti, R. Boisgard, C. Ngô, and J. Desbois, Nucl. Phys. **A492**, 322 (1989).

[Conj 85] M. Conjeaud, S. Harar, M. Mostefai, E.C. Pollacco, C. Volant, Y. Cassagnou, R. Dayras, R. Legrain, H. Oeschler, and F. Saint-Laurent, Phys. Lett. **159B**, 244 (1985).

[Conr 93] J.A. Conrad, M.S. Thesis, Michigan State University, 1993.

[Cugn 82] J. Cugnon, J. Knoll, C. Riedel, and Y. Yariv, Phys. Lett. **109B**, 167 (1982).

[Cugn 83] J. Cugnon and D. L'Hote, Nucl. Phys. **A397**, 519 (1983).

[Dani 83] P. Danielewicz and M. Gyulassy, Phys. Lett **129B**, 283 (1983).

[Desb 87] J. Desbois, R. Boisgard, C. Ngô, and J. Nemeth, Z. Phys. **A328**, 101 (1987).

[deSo 91] R.T. de Souza, L. Phair, D.R. Bowman, N. Carlin, C.K. Gelbke, W.G. Gong, Y.D. Kim, M.A. Lisa, W.G. Lynch, G.F. Peaslee, M.B. Tsang, H.M. Xu, F. Zhu, W.A. Friedman, Phys. Lett. **B268**, 6 (1991).

[Ethv 91] T. Ethvignot, A. Elmaani, N.N. Ajitanand, J.M. Alexander, E. Bauge, P. Bier, L. Kowalski, M.T. Magda, P. Désesquelles, H. Elhage, A. Giorni, D. Heuer, S. Kox, A. Lleres, F. Merchez, C. Morand, D. Rebreyend, P. Stassi, J.B. Viano, S. Benrachi, B. Chambon, B. Cheynis, D. Drain, C. Pastor, Phys. Rev. **C43**, R2035 (1991).

[Fai 83] G. Fai and J. Randrup, Nucl. Phys. **A404**, 551 (1983).

[Faty 85] M. Fatyga, K. Kwiatkowski, V.E. Viola, C.B. Chitwood, D.J. Fields, C.K. Gelbke, W.G. Lynch, J. Pochodzalla, M.B. Tsang, Phys. Rev. Lett **55**, 1376 (1985).

[Faty 87a] M. Fatyga, K. Kwiatkowski, V.E. Viola, W.G. Wilson, M.B. Tsang, J. Pochodzalla, W.G. Lynch, C.K. Gelbke, D.J. Fields, C.B. Chitwood, Z. Chen, T. Nayak, Phys. Rev. Lett. **58**, 2527 (1987).

[Faty 87b] M. Fatyga, R.C. Byrd, K. Kwiatkowski, W.G. Wilson, L.W. Woo, V.E. Viola Jr., H.J. Karwowski, J. Jastrzebski, W. Skulski, Phys. Lett. **B185**, 321 (1987).

[Fiel 86] D.J. Fields, W.G. Lynch, T.K. Nayak, M.B. Tsang, C.B. Chitwood, C.K. Gelbke, R. Morse, J. Wilczynski, T.C. Awes, R.L. Ferguson, F. Plasil, F.E. Obenshain, G.R. Young, Phys. Rev. **C34**, 536 (1986).

[Gelb 87] Claus-Konrad Gelbke and David H. Boal, Prog. Part. Nuc. Phys., **19**, 33 (1987).

[Gros 86] D.H.E. Gross, Zhang Xiao-ze, Xu Shu-yan, Phys. Rev. Lett. **56**, 1544 (1986).

[Gros 89] D.H.E. Gross, G. Klotz-Engmann, H. Oeschler, Phys. Lett. **B224**, 29 (1989).

[Gual 95] E. Gualtieri, J. Yee, D. Craig, S.A. Hannuschke, T. Li, W.J. Llope, R. Pak, N.T.B. Stone, A.M. Vander Molen, G.D. Westfall, J.S. Winfield, S.J. Yennello, Roy A. Lacey, A. Nadasen, E. Norbeck, Submitted to Phys. Lett.

[Gust 84] H.A. Gustafsson, H.H. Gutbrod, B. Kolb, H. Löhner, B. Ludewigt, A.M. Poskanzer, T. Renner, H. Riedesel, H.G. Ritter, A. Warwick, F. Weik, H. Wieman, Phys. Rev. Lett. **52**, 1590 (1984).

[Gyul 82] M. Gyulassy, K.A. Frankel, and H. Stöcker, Phys. Lett. **110B**, 185 (1982).

[Harm 90] B.A. Harmon, J. Pouliot, J.A. López, J. Suro, R. Knop, Y. Chan, D.E. Digregorio, R.G. Stokstad, Phys. Lett. **B235**, 234 (1990).

[Harp 71] G.D. Harp and J.M. Miller, Phys. Rev. **C3**, 1847 (1971).

[Jacq 84] D. Jacquet, E. Duek, J.M. Alexander, B. Borderie, J. Galin, D. Gardès, D. Guerreau, M. Lefort, F. Monnet, M.F. Rivet, X. Tarrago, Phys. Rev. Lett. **53**, 2226 (1984).

[Jacq 85] D. Jacquet, J. Galin, M.F. Rivet, R. Bimbot, B. Borderie, D. Gardès, B. Gatty, D. Guerreau, L. Kowalski, M. Lefort, X. Tarrago, Nucl. Phys. **A445**, 140 (1985).

[Jian 89] D.X. Jiang, H. Doubre, J. Galin, D. Guerreau, E. Piasecki, J. Pouthas, A. Sokolov, G. Cramer, G. Ingold, U. Jahnke, E. Schwinn, J.L. Charvet, J. Frehaut, B. Lott, C. Magnago, M. Morjean, Y. Patin, Y. Pranal, J.L. Uzureau, B. Gatty, and D. Jacquet, Nucl. Phys. **A503**, 560 (1989).

[Leeg 92] H.K.W. Leegte, A.L. Boonstra, J.D. Hinnefeld, E.E. Koldenhof, R.H. Siemssen, K.Siwek-Wilczyńska, Z. Sosin, J. Wilczyński, and H.W. Wilschut, Phys. Rev. **C46**, 991 (1992).

[Lera 84] S. Leray, G. Nebbia, C. Gregoire, G. La Rana, P. Lhenoret, C. Mazur, C. Ngô, S. Chiodelli, J.L. Charvet, C. Lebrun, Nucl. Phys. **A425**, 345 (1984).

[Llop 93] W.J. Llope, D. Craig, E. Gualtieri, S. Hannuschke, R.A. Lacey, T. Li, A. Nadasen, E. Norbeck, R. Pak, N. Stone, A.M. Vander Molen, G.D. Westfall, J.S. Winfield, J. Yee, S.J. Yennello, Michigan State University Preprint, MSUCL-900.

[Llop 95] W.J. Llope, J.A. Conrad, C.M. Mader, G. Peilert, W. Bauer, D. Craig, E. Gualtieri, S. Hannuschke, R.A. Lacey, J. Lauret, T. Li, A. Nadasen, E. Norbeck, R. Pak, N.T.B. Stone, A.M. Vander Molen, G.D. Westfall, J. Yee, S.J. Yennello, Phys. Rev. **C51**, 1325 (1995).

[Lope 89] J.A. López and J. Randrup, Nucl. Phys. **A491**, 477 (1989).

[Moni 71] E.J. Moniz, I. Sick, R.R. Whitney, J.R. Ficenec, R.D. Kephart, W.P. Trower, Phys. Rev. Lett. **26**, 445 (1971).

[Nich 59] W.J. Nicholson, I. Halpern, Phys. Rev. **116**, 175 (1959).

[Ngo 86] Ch. Ngô, Prog. in Part. and Nucl. Phys., **16**, 139 (1986).

[Nife 85] H. Nifenecker, J. Blachot, J. Crancon, A. Gizon, A. Lleres, Nucl. Phys **A447**, 533c (1985).

[Ogil 91] C.A. Ogilvie, J.C. Adloff, M. Begemann-Blaich, P. Bouissou, J. Hubele, G. Imme, I. Iori, P. Kreutz, G.J. Kunde, S. Leray, V. Lindenstruth, Z. Liu, U. Lynen, R. J. Meijer, U. Milkau, W.F.J. Müller, C. Ngô, J. Pochodzalla, G. Raciti, G. Rudolf, H. Sann, A. Schüttauf, W. Seidel, L. Stuttge, W. Trautmann, A. Tucholski, Phys. Rev. Lett. **67**, 1214 (1991).

[Phai 92] L. Phair, D.R. Bowman, C.K. Gelbke, W.G. Gong, Y.D. Kim, M.A. Lisa, W.G. Lynch, G.F. Peaslee, R.T. de Souza, M.B. Tsang, F. Zhu, Nucl. Phys. **A548**, 489 (1992).

[Plas 78] F. Plasil, R.L. Ferguson, H.C. Britt, B.H. Erkkila, P.D. Goldstone, R.H. Stokes, H.H. Gutbrod, Phys. Rev. **C18**, 2603 (1978).

[Poll 84] E.C. Pollacco, M. Conjeaud, S. Harar, C. Volant, Y. Cassagnou, R. Dayras, R. Legrain, M.S. Nguyen, H. Oeschler, and F. Saint-Laurent, Phys. Lett. **146B**, 29 (1984).

[Poll 93] E.C. Pollacco, C. Volant, Y. Cassagnou, M. Conjeaud, R. Dayras, S. Harar, R. Legrain, J. Sauvestre, Z. Phys. **A346**, 63 (1993).

[Pori 60] N.T. Porile, Phys. Rev. **120**, 572 (1960).

[Pori 89] N.T. Porile, A.J. Bujak, D.D. Carmony, Y.H. Chung, L.J. Gutay, A.S. Hirsch, M. Mahi, G.L. Paderewski, T.C. Sangster, R.P. Scharenberg, B.C. Stringfellow, Phys. Rev. **C39**, 1914 (1989).

[Sain 84] F. Saint-Laurent, M. Conjeaud, R. Dayras, S. Harar, H. Oeschler, C. Volant, Nucl. Phys. **A422**, 307 (1984).

[Sang 92] T.C. Sangster, H.C. Britt, D.J. Fields, L.F. Hansen, R.G. Lanier, M.N. Namboodiri, B.A. Remington, M.L. Webb, M. Begemann-Blaich, T. Blaich, M.M. Fowler, J.B. Wilhelmy, Y.D. Chan, A. Dacal, A. Harmon, J. Pouliot, R.G. Stokstad, S. Kaufman, F. Videbaek, Z. Fraenkel, G. Pielert, H. Stöcker, W. Greiner, A. Botvina, I.N. Mishustin, Phys. Rev. **C46**, 1404 (1992).

[Schw 94] E. Schwinn, U. Jahnke, J.L. Charvet, B. Cramer, H. Doubre, J. Fréhaut, J. Galin, B. Gatty, D. Guerreau, G. Ingold, D. Jacquet, D.X. Jiang, B. Lott, M. Morjean, C. Magnago, Y. Patin, J. Pouthas, E. Piasecki, A. Sokolow, Nucl. Phys. **A568** (1994).

[Sikk 62] T. Sikkeland, V.E. Viola, Phys. Rev. **125**, 1350 (1962).

[Troc 89] R. Trockel, K.D. Hildenbrand, U. Lynen, W.F.J. Müller, H.J. Rabe, H. Sann, H. Stelzer, W. Trautmann, and R. Wada, Phys. Rev. **C39**, 729 (1989).

[Tsan 83] M.B. Tsang, D. Ardouin, C.K. Gelbke, W.G. Lynch, Z.R. Xu, B.B. Back, R. Betts, S. Saini, P.A. Baisden, and M.A. McMahan, Phys. Rev. **C28**, 747 (1983).

[Tsan 84] M.B. Tsang, C.B. Chitwood, D.J. Fields, C.K. Gelbke, D.R. Klesch, W.G. Lynch, K. Kwiatkowski, and V.E. Viola, Jr., Phys. Rev. Lett. **52**, 1967 (1984).

[Tsan 89] M.B. Tsang, Y.D. Kim, N. Carlin, Z. Chen, R. Fox, C.K. Gelbke, W.G. Gong, W.G. Lynch, T. Murakami, T.K. Nayak, R.M. Ronningen, H.M. Xu, F. Zhu, L. Sobotka, D. Stracener, D.G. Sarantites, Z. Majka, V. Abenante, H. Griffin, Phys. Lett. **B220**, 492 (1989).

[Tsan 90] M.B. Tsang, Y.K. Kim, N. Carlin, Z. Chen, C.K. Gelbke, W.G. Gong, W.G. Lynch, T. Murakami, T. Nayak, R.M. Ronningen, H.M. Xu, F. Zhu, L.G. Sobotka, D.W. Stracener, D.G. Sarantites, Z. Majka, and V. Abenante, Phys. Rev. **C42**, R15 (1990).

[Tsan 91] M.B. Tsang, R.T. de Souza, Y.D. Kim, D.R. Bowman, N. Carlin, C.K. Gelbke, W.G. Gong, W.G. Lynch, L. Phair, and F. Zhu, Phys. Rev. **C44**, 2065 (1991).

[Utle 94] D. Utley, R. Wada, K. Hagel, J. Li, X. Bin, M. Gui, Y. Lou, R. Tezkratt, J.B. Natowitz, and M. Gonin, Phys. Rev. **C49**, R1737 (1994).

[Viol 82] V.E. Viola Jr., B.B. Back, K.L. Wolf, T.C. Awes, C.K. Gelbke, and H.Breuer, Phys. Rev. **C26**, 178 (1982).

[Viol 85] V.E. Viola, K. Kwiatkowski, M. Walker, Phys. Rev. **C31**, 1550 (1985).

[Viol 89] V.E. Viola, Nuclear Physics **A502**, 531c (1989).

[Warw 83] A.I. Warwick, H.H. Wieman, H.H. Gutbrod, M.R. Maier, J. Péter, H.G. Ritter, H. Stelzer, F. Weik, M. Freedman, D.J Henderson, S.B. Kaufman, E.P. Steinberg, B.D. Wilkins, Phys. Rev. **C27**, 1083 (1983).

[West 85] G.D. Westfall et al., Nucl. Inst. and Meth. **A300**, 518 (1991).

[Wils 91] W.K. Wilson, Ph.D. Thesis, Michigan State University, 1991.

[Woo 83] L.W. Woo, K. Kwiatkowski, V.E. Viola Jr., Phys. Lett **B132**, 283 (1983).

[Yee 95] J. Yee, E. Gualtieri, D. Craig, S.A. Hannuschke, T. Li, W.J. Llope, R. Pak, N.T.B. Stone, A.M. Vander Molen, G.D. Westfall, J.S. Winfield, S.J. Yennello, Roy A. Lacey, A. Nadasen, E. Norbeck, Submitted to Phys. Lett.

[Yee 95b] J. Yee, Ph.D. Thesis, Michigan State University, 1995.

[Yenn 90] S.J. Yennello, K. Kwiatkowski, D.E. Fields, R. Planeta, V.E. Viola, E.C. Pollacco, C. Volant, R. Dayras, R. Legrain, Y. Cassagnou, S. Harar, E. Hourani, Phys. Lett. **B246**, 26 (1990).

[Zoln 78] D.R. Zolnowski, H. Yamada, S.E. Cala, A.C. Kahler, T.T. Sugihara, Phys. Rev. Lett. **41**, 92, (1978).